2014-9

Analysis and Design of Footwear Antennas

Domenico Gaetano

Technological University Dublin, domenico.gaetano@mydit.ie

Analysis and Design of Footwear Antennas

Domenico Gaetano

Doctor of Philosophy

Supervisors:
Dr. Patrick McEvoy
Prof. Max J. Ammann

Dublin Institute of Technology
School of Electrical & Electronic Engineering

September 2014

ABSTRACT

Wearable technologies are found in an increasing number of applications including sport and medical monitoring, gaming and consumer electronics. Sensors are used to monitor vital signs and are located on various parts of the body. Footwear sensors permit the collection of data relating to gait, running style, physiotherapy and research. The data is sent from sensors to on-body hubs, often using wired technology, which can impact gait characteristics. This thesis describes the design of footwear antennas for wireless sensor telemetry. The work addresses the challenges of placing antennas close to the foot as well as the proximity to the ground. Guidelines for polarization are presented. The channel link between footwear and wrist is investigated for both narrowband and wideband channels across different frequencies. The effects of the body proximity and movement were gauged for walking subjects and are described in terms of the Rician Distribution K-factor. Different antenna solutions are presented including UWB antennas on various footwear locations as well as 433 MHz integrated antennas in the insole. Both directional and omnidirectional antennas were considered for UWB and the evaluation was for both time-domain and frequency-domain.

The research established new ideas that challenge the old paradigm of the waist as the best hub position, demonstrating that a hub on the footwear using directional antennas outperforms a hub on the waist using an omnidirectional antenna. The cumulative distribution functions of measured path gains are evaluated and the results are described in terms of the achievable minimum data rate considering the Body Area Network standard.

DECLARATION

I certify that this thesis which I now submit for examination for the award of PhD, is entirely my own work and has not been taken from the work of others save and to the extent that such work has been cited and acknowledged within the text of my own work.

This thesis was prepared according to the regulations for postgraduate study by research of the Dublin Institute of Technology and has not been submitted in whole or in part for an award in any other Institute or University.

The work reported in this thesis conforms to the principles and requirements of the Institute's guidelines for ethics in research.

The Institute has permission to keep, to lend or to copy this thesis in whole or in part, on condition that any such use of the material of the thesis be duly acknowledged.

Signature: ________________________ Date __________
Domenico Gaetano

ACKNOWLEDGMENTS

My first thought goes to the immateriality of human reason, and how it could have resulted in a so reticent and eccentric combination of neurons without order or sense. I can't forget people who watched over my adventure in Dublin - I would have been lost without them. People of the lab, you could accompany any weird mood of mine, I'd like to thank you for the staring, silence, sniffs, laughs and good craic. Thanks to the discussions with Pádraig, thanks to Adam to be always present, thanks to Vit for his help, thanks to Giuseppe that believed in me, and thanks to Max for his patience and for his leadership. Thanks to you all, Afshin, Oisin, Abraham, Matthias, Xiulong and Antoine! I can't thank the several people of the Coombe, so many, so different universes that intersected each other and created beautiful pictures. I will never forget Rali's humour, Adam's discussion, Fabiola's creativity, Alexandre's way to discover the world, and Julia's sense of life. And also for all the others, I always was able to get something from you. Thanks to Dee because she made my days special. Thanks to Carlos, for the funny and amazing time we spent together! Thanks to my brother, because he has always believed in me. Thanks to my parents, Carlo and Felicia, because my pride and my goals are strictly connected to their nostalgia. I won't forget my other friends, Roberto, Domenico, Giuseppe, Mariangela, Maria, Pasqualina, Kiril, Chiara, and all the others I can't mention here. I can't forget John, a good life-mate who taught me so much and made me feel good. Thanks to Ireland to exist, for the mix of different cultures and to welcome people from every country. Everybody left a trace inside me, and I am really glad to have met all of you.

Nomenclature

BW	impedance bandwidth
c_0	speed of light in vacuum, 299 792 458 m/ s
C	capacitance (F)
D	directivity (dBi)
δ_{tan}	loss tangent of a dielectric material
ϵ_r	relative dielectric constant of a dielectric material
η_{rad}	radiation efficiency
η_{total}	total efficiency
f	frequency (GHz)
G	gain (dBi)
G_r	realized gain (dBi)
h	substrate thickness
λ_0	wavelength (m)
P_{rad}	total power radiated (W)
ψ	phase of the transfer function (°)
R_{in}	input resistance of antenna (Ω)
S_{nn}	input reflection coefficient at port n
S_{mn}	transmission coefficient between ports n and m
σ	conductivity of a material (S/m)
θ, ϕ	angular coordinates in spherical coordinate system (°)
U	radiation intensity (W/unit solid angle)
x, y, z	coordinates in a cartesian coordinate sytem (m)
Z_{in}	input impedance of antenna (Ω)

ABBREVIATIONS

BAN	Body Area Network
BER	Bit Error Rate
CDF	Cumulative Distribution Function
CPW	Coplanar Waveguide
CST	Computer Simulation Technology GmbH
DIT	Dublin Institute of Technology
FF	Fidelity Factor
GPS	Global Positioning System
IEEE	Institute of Electrical and Electronics Engineers
LOS	Line Of Sight
MLE	Maximum Likelihood Estimation
NLOS	Non Line Of Sight
OFDM	Orthogonal Frequency-Division Multiplexing
OOK	On-Off Keying
PCB	Printed Circuit Board
PEC	Perfect Electric Conductor
PPM	Pulse Position Modulation
RRC	Root Raised Cosine
SAR	Specific Absorption Rate
SMA	SubMiniature Type A Connector
UWB	Ultra Wide Band
VNA	Vector Network Analyser

CONTENTS

List of Figures

LIST OF TABLES

1. Introduction

Up to now, most research on Body Area Network (BAN) antennas was focused on the upper body, for locations above the ankle. Handheld devices such as smartphones, portable electronics and video game consoles which can represent the main hub of a BAN are usually located in pockets waist-high or above.

No work is reported on footwear antennas or on the effects of ground proximity on footwear telemetry communications channels. Moreover, a footwear antenna design should consider the spatiotemporal characteristics of human gait and the different footwear shapes. On-body antennas are normally designed to be omnidirectional in order to communicate with sensors deployed on different body locations. In contrast to conventional on-body antennas, an antenna in a footwear scenario for on-body communication has one direction of interest, above the ground. The antenna design must include a minimum antenna beamwidth to illuminate different body areas when taking into account the natural gait during walking, running and everyday activities.

A brief history of the research on antennas and human body is presented. The research evolution is given, and how it slowly evolved from a generic case of how the human body affects antenna performance, to a variety of more specific aspects such as the effects of antenna radiation on the body, numerical and physical phantoms, new antenna technologies and propagation channels. Finally an overview of directional Vivaldi antennas and footwear research is reported.

1.1. On-Body Antennas

Early research on human-body antenna interaction was initially confined to VHF and low-UHF frequency coupling between the body and a whip antenna at 100 MHz [1] and with a dipole antenna at 450 and 900 MHz [2] for different body locations, as shown in Fig. 1.1.

These papers investigated the effects of the human body on the antenna impedance and gain. The research later focused on the absorption of electromagnetic waves in the body [3] and on imaging applications [4]. With the introduction of mobile phones, the research progressed to the effects of the human body on portable handheld telecommunication systems [5–8]. Models representing the head, the mobile phone case and the hand, shown in Fig. 1.2, were developed.

While in [5–8] the effects of the body on the antenna parameters are evaluated, in [8] an antenna is designed to minimize body interaction. The concepts of wearable electronic devices for health monitoring applications and gaming were explored, leading to the development of Body Area Net-

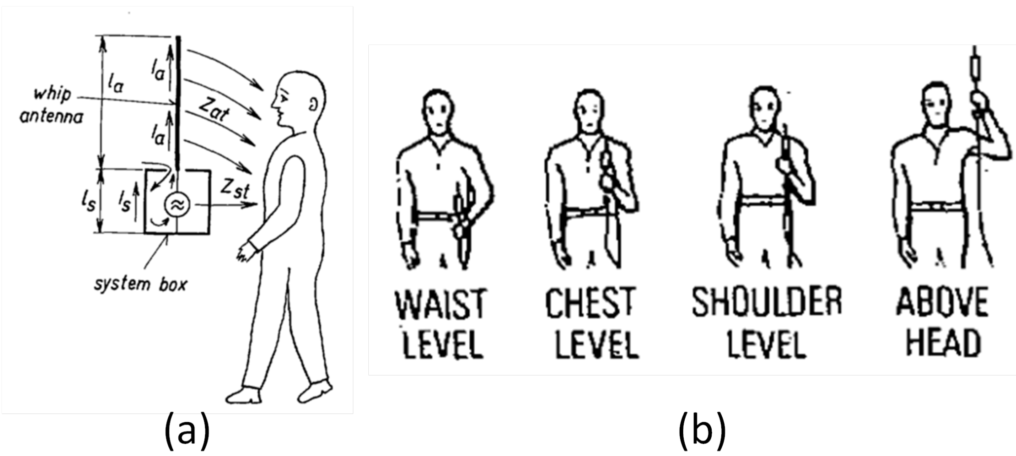

Figure 1.1. Basic small-sized communication system arrangement for whip antenna (a) and antenna/body positions for radiation pattern measurements with $\lambda/2$ choke dipole (b) [1, 2].

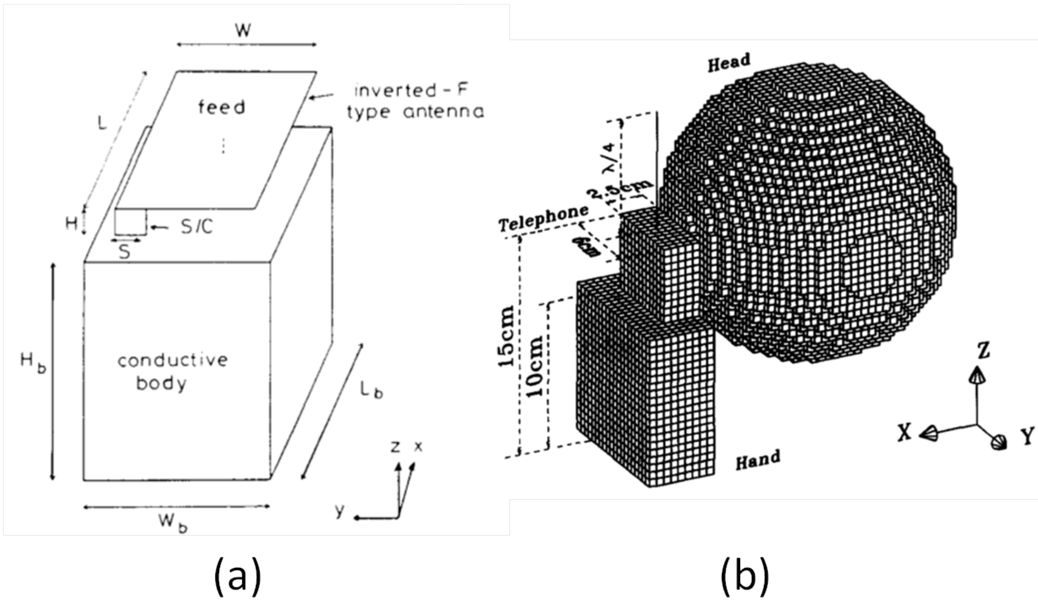

Figure 1.2. Solid on-body model with inverted-F planar antenna (a) and simulated telephone with hand and head voxel model (b) [5–8].

works (BAN) [9]. BANs are short range wireless communication networks in the proximity of or inside a human body [10]. The human body became the landscape for different deployed sensors. Biological sensor signals on body movement [11–13], blood pressure [13, 14] , body and skin temperature [13], oxygen saturation [14], respiration rate [12] and electrocardiogram [12] were obtained. A survey of wearable sensor-based systems for health monitoring and prognosis is described in [15]. Sensors are usually small and simple devices with the sole purpose of detecting a biological parameter and relaying it to a smarter node, defined as a hub. The hub can be a hand held device or a router located on a person's waist. Body communication [16, 17] can be classified as:

- on-body communication, considering sensors and gateways on the human body;
- off-body communication, considering sensors on the human body,

and the gateway off-body usually within 3 meters from the human body;

- in-body communication, considering communication between sensors-actuators inside the human body and on-body and off-body devices.

Inter-body communication refers to communication link between nodes located on the body. Intra-body communication refers to a communication link between a node located on the body and another node located off-body or on a different on-body location. Considering on-body communication links, initially series of S_{21} measurements were performed for two quarter-wavelength monopole antennas at 2.45 GHz on different on-body locations [18] to assess the channel model. Different antenna technologies are investigated resulting in better performance by a polarization perpendicular to the body surface and assessing that the body and the local environment influence the system performance. The research was limited to a narrow-band channel at 2.45 GHz. A novel disc-loaded reduced height monopole [18] was optimized for on-body performance, but not low profile. Instead of a real human body, a cylindrical phantom [19] was used to compare different antenna performances. The antennas used in the paper are shown in Fig. 1.3.

A higher mode microstrip patch antenna was demonstrated to perform as well as the quarter-wavelength monopole antenna in an anechoic environment. However in an indoor environment, where multipath propagation predominates, the performance of a patch antenna at the fundamental mode is better [19, 20]. An active antenna was finally designed to adapt the pattern as a function of the environment [21] using end-fire or off-body patterns. The previous reported work was limited to 2.45 GHz or below, and the antennas were always located above the ankle. Because the antennas were always located on the upper body, the proximity to the ground was never investigated in terms of reflection coefficient. There is some reported work on the ground materials because of the reflective components

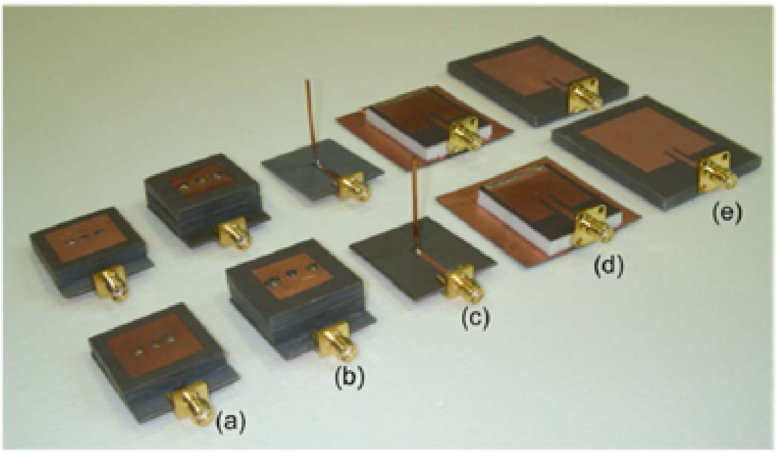

Figure 1.3. 2.45 GHz antennas with different patterns: (a) 5 mm high modes microstrip patch antenna, (b) 10 mm high modes microstrip patch antenna, (c) monopole antenna, (d) reduced microstrip patch antenna, (e) microstrip patch antenna [19].

of the main radiating element which impacts on the on-body and off-body communication links. The influence of the proximity to different ground types on the antenna reflection coefficient has never been investigated. The effects of the body movements were investigated with measurements and different channel propagation models obtained [18].

1.2. Ultra Wideband Antennas

The increased presence of different radiators on the body and the higher data rate requirement push the designers to new communication systems such as Ultra Wide Band (UWB). UWB provides high data rate and low power consumption for short range communication and it is suitable for BANs. Commercial UWB antennas were used [22–24] to initially investigate the interaction with the human body. The first UWB investigation of on-body antennas was conducted by Welch et al. [22], reporting the

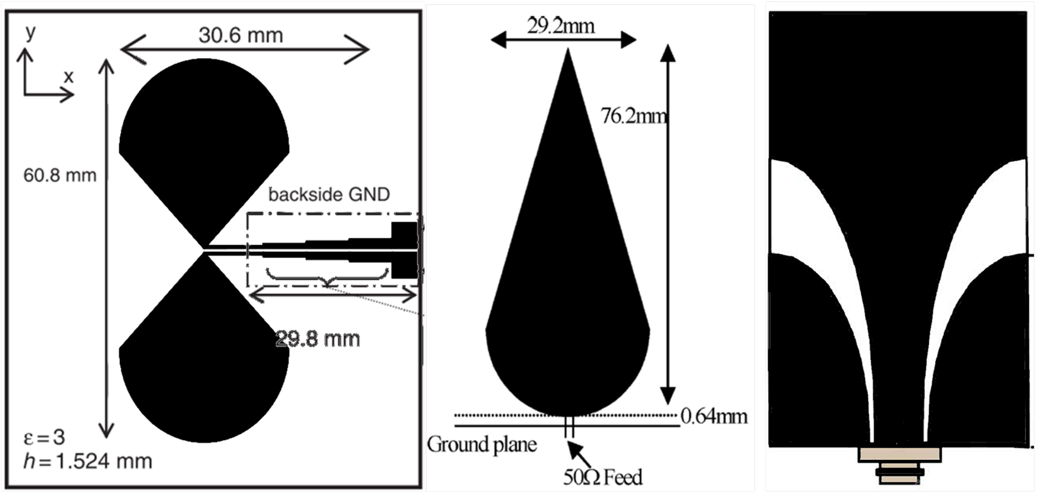

Figure 1.4. Horn shaped self-complementary antenna (HSCA) with 3-stage Chebyshev transformer, planar inverted cone antenna and CPW-fed tapered slot antenna [25–28].

human body interaction with a close proximity UWB PulsOn antenna in an anechoic chamber as well as in various different indoor multipath environments. The study proved that in a dense multipath environment the communication link was better. Time-domain performance of a horn shaped complementary antenna (HSCA) and planar inverted cone antennas (PICA) [25, 26] were investigated and the on-body UWB channel was studied [27]. The channel model using HSCA was characterized by lower mean root mean square (RMS) delay spread for surface wave propagation. The channel model using PICA was characterized by smaller path loss in a non-reflecting environment and a greater signal distortion. Later a CPW-fed tapered slot antenna shown in Fig. 1.4 was proposed and compared with the HSCA [28, 29].

Other researchers introduced different parameters to characterize the antenna such as the frequency-domain transfer function, the spatially-averaged transfer function and the fidelity factor [30] using RF over fibre to minimize the cable influence on the antenna performance. There are different

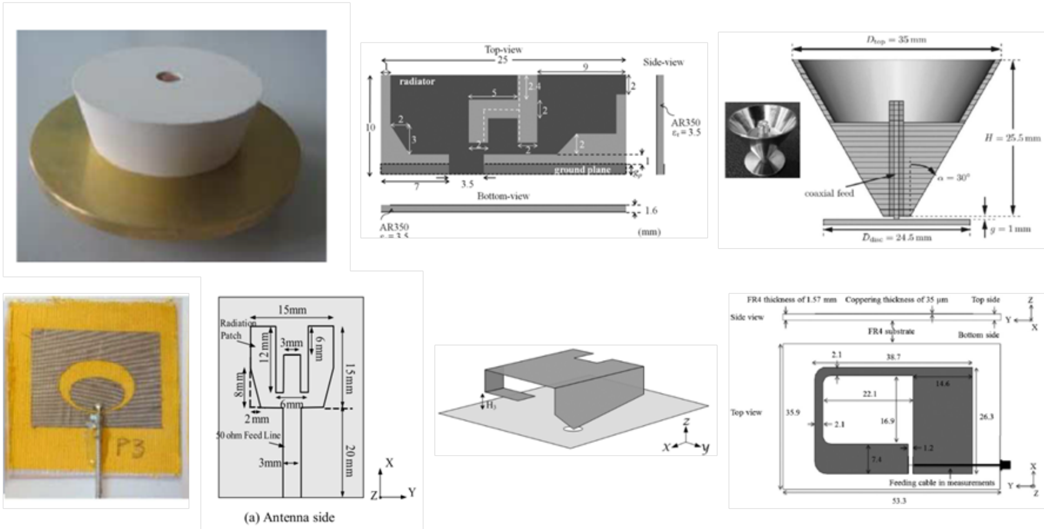

Figure 1.5. Different UWB antennas technologies: dielectric antenna, monopole antenna, discone antenna, slot antenna, 3-D antenna and loop antenna [34–40].

techniques to increase the antenna bandwidth, such as adding slots in the antenna and in the ground plane [31–33]. Different antenna technologies were implemented for on-body antennas, such as dielectric resonator antennas [34], monopoles [35, 36], discone antennas [37], slot antennas [38], 3-D structure [39] and loops [40] shown in Fig. 1.5.

The difference in Bit-Error-Rate (BER) performance is investigated for different modulation schemes for antennas located on the body in an anechoic chamber and in a staff lounge room [33], reporting that pulse position modulation (PPM) is very sensitive to the RMS delay spread and that on-off keying (OOK) is less sensitive to channel environments. In other research the performance for OFDM [41, 42] is reported, showing a BER equal to or smaller than 0.1% for more than 75% cases for a static person. The effects of the body movement on the UWB channel have been investigated in 2009 [24] just for the upper body, both numerically and experimentally, investigating 35 different postures. Also the effects of arm swing movements

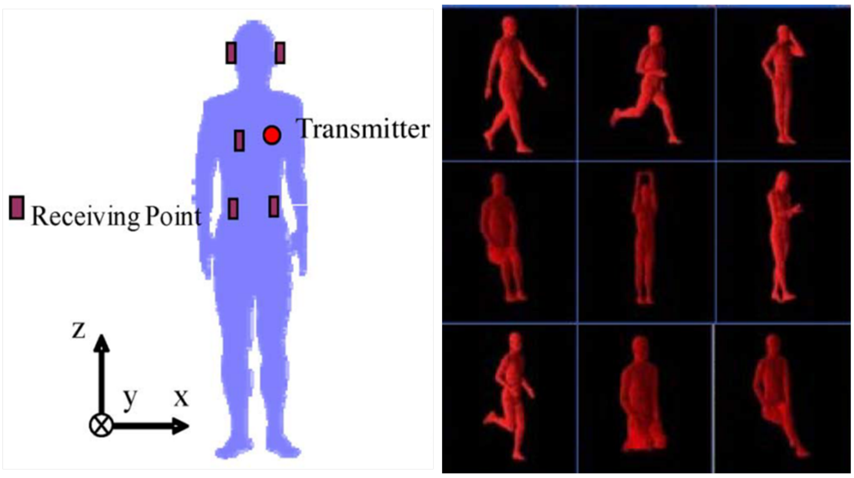

(a) (b)

Figure 1.6. Location for the transmitting and receiving antenna (a) and different investigated on-body postures (b) [24, 42].

were investigated for four different links in an anechoic chamber and in a multipath environment [42], shown in Fig. 1.6, revealing that classical channel characterisation models for the wrist-to-belt link are less accurate because of variations in antenna alignment and distance.

1.3. Directional Antennas

Generally the antennas are omnidirectional for on-body communications or directional for off-body communications. Considering the footwear scenario, directional end-fire antennas on particular locations can be used to direct the antenna pattern above the ground and to the upper body.

Vivaldi antennas are used to reduce the ground effects, minimizing backlobe radiation. Vivaldi antennas are aperiodic continuously scaled antennas [45] with theoretically infinite gain. They belong to the frequency independent antenna group whose impedance properties and patterns are frequency independent above a certain value. Normally the Vivaldi antenna

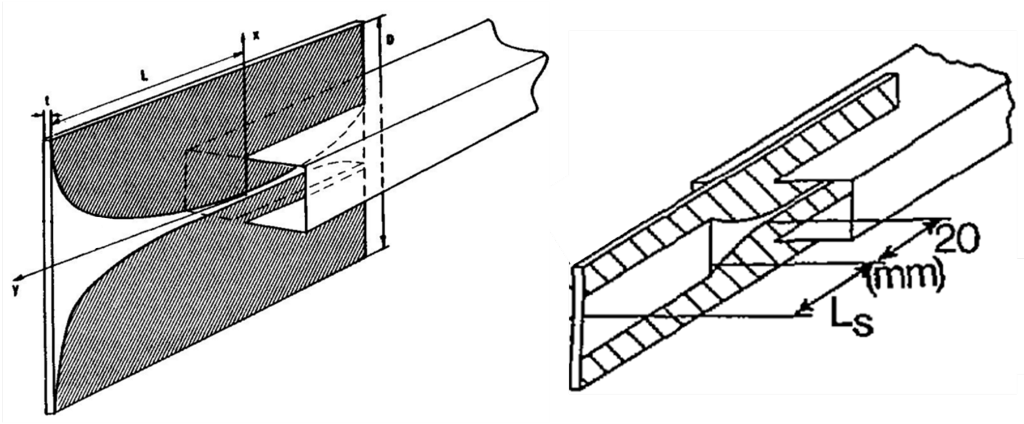

Figure 1.7. Fin-line feed for different Vivaldi antenna shapes [43, 44].

requires a Balun or it has to be fed by fin-line [43, 46], as shown in Fig. 1.7. Another way to feed the antenna is to print the two flares of the Vivaldi antenna on different layers and feed the two flares with an unbalanced line, as in [47], as shown in Fig. 1.7. In this case the antenna is characterized by high cross-polarization. To overcome the high cross-polarization, another layer with another Vivaldi flare is added to the antenna [48, 49], as shown in Fig. 1.8.

For some applications, it is important to use just one layer of the dielectric. Antennas on a single layer are low profile, easier to manufacture and

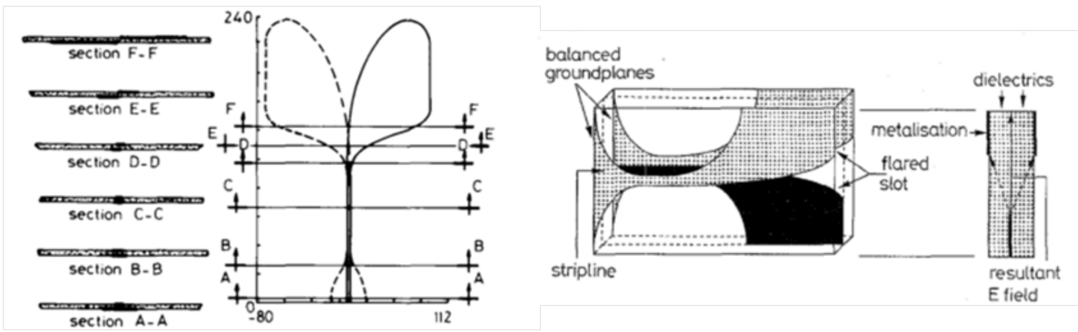

Figure 1.8. Balanced feed for two and three layers antipodal Vivaldi antenna [47, 49].

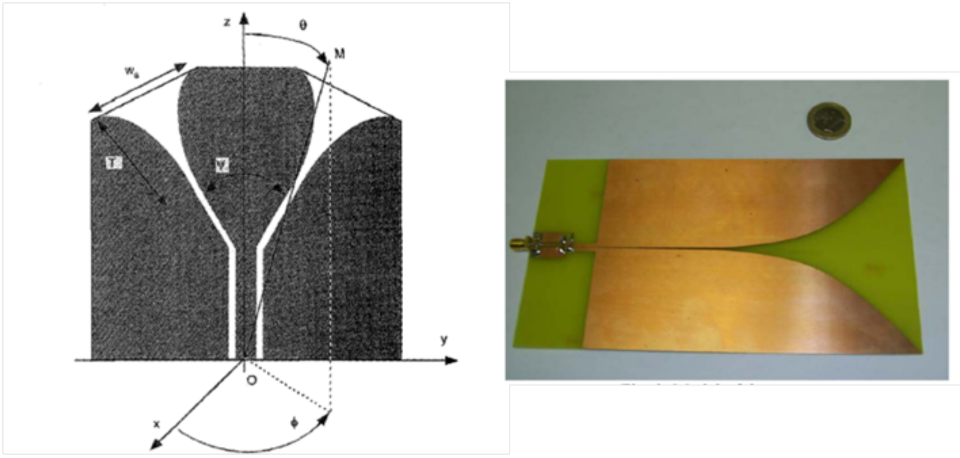

Figure 1.9. Coplanar waveguide feed for single sided twin Vivaldi antenna and with integrated Balun [50, 53].

to integrate in PCB technology. Examples of one-sided Vivaldi antennas shown in Fig. 1.9 are a twin Vivaldi antenna [50, 51] and a classic Vivaldi antenna fed by a coplanar-to-slot-line transition [52–54].

1.4. Footwear Antennas

The first research work on footwear antennas is the Nike in-shoe antenna, a 2009 patented system where a 2.4 GHz antenna is located in an aperture in the sole of the shoe [55]. The antenna is a curved inverted-F element that uses the printed circuit board as a ground plane and the battery as a passive element. The antenna is fully integrated within the sole of the shoe, but it covers just the 2.4 GHz band. The antenna performance is not described in relation to the body or ground proximity and it seems that the antenna is not optimized for on-body performance. The authors stated that their main object was to ensure a high on-body radiation efficiency and a wide bandwidth for the footwear-embedded antenna to overcome the effects of the close body proximity.

An antenna for a footwear Global Positioning System (GPS) was patented

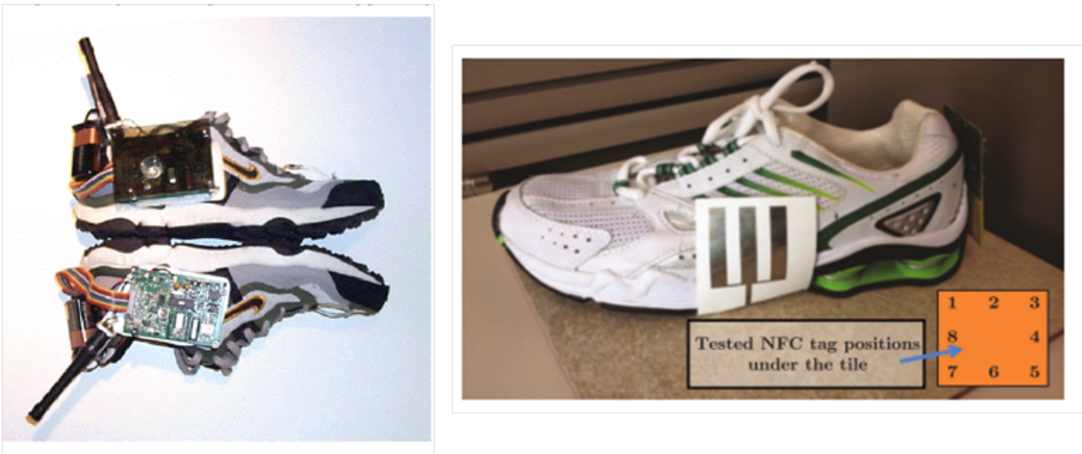

Figure 1.10. Monopole antenna on footwear and dual-band integrated monopole on footwear lateral quarter [59, 60].

in 2004 [56]. No details about the antenna geometry are reported, but the patent states the possibility of a module embedded in the shoe sole. The antenna position is suggested to be on the shoe tongue, although no reason is given to justify this choice.

Research on footwear electronics is mostly on Indoor Geo-location, where most details are given to the device rather than the antenna performance [57, 58]. Another shoe application is an experimental dancing application [59], to transform sensed data to music. In this case a normal monopole antenna shown in Fig. 1.10 is used and again no particular focus was given to antenna performances in close proximity to the body and ground.

A dual-band footwear antenna was embedded in the shoe toe cap for radar applications [61]. The antenna performance was investigated for different curvatures, but there is no human body or ground proximity analysis.

Another dual-band antenna shown in Fig. 1.10 was embedded as a brand logo on the lateral side of the shoe [60] for health monitoring and indoor localization. The simulated radiation pattern in the presence of the body is shown, but it is not clear if the ground is included in the modelling.

The simulated and measured scattering parameters are shown, but it is not stated whether they are in free space or on-body. From the pattern, the antenna radiates to one side off-body, so on-body sensors will not be covered. In all the previous research the footwear antenna was simply a normal antenna located on the footwear. The influence of the body and of the ground were not taken into account for the antenna design. The footwear environment is a complex scenario where different elements have to be taken into account, as the antenna orientation, the low profile and the antenna position in respect to the on-body and the off-body sensor locations. In this work the main focus is to define general design rules and some unique properties related to the footwear scenario.

1.5. Numerical and Physical Phantoms

Numerical phantoms were initially layers of heterogeneous or homogeneous dielectrics with constant electric properties [30, 31, 34] but later on, detailed voxel models were used. Homogeneous body models can be made using the various dimensional body characteristics. These models can be later modified to assume different postures to simulate different stances such as walking, running, sitting, etc [24]. Most of the experimental work used real human subjects [18, 23, 25, 26, 28, 34, 41, 42], but also physical phantoms were developed [19, 20, 35]. There are different methods to develop phantoms that resemble the electrical properties of the human body [19, 20] but few for UWB phantoms [35]. After the phantom realization, it is necessary to measure the electrical properties, using waveguides [62], ring resonators [63], open coaxial cables [64] or free-space measurements [65].

1.6. Antenna Parameters

In the antenna design different parameters have to be taken into account. Some parameters, such as the reflection coefficient and the radiation pattern, are important for all the antennas. Some other parameters, such as the fidelity factor and the group delay, are important for applications where the pulse purity is required.

1.6.1. Scattering Parameters

Every microwave device can be characterized with an impedance matrix, an admittance matrix, an ABCD matrix or a scattering matrix. The scattering matrix is mainly used for microwave devices because they can be directly measured with a Vector Network Analyzer (VNA), including at higher frequencies. From the scattering parameters it is straightforward to calculate the other matrices. Considering an N-port device, the scattering parameters represent the ratio of the input and the reflected or transmitted voltage waves, as shown in Fig. 1.11

A single S-parameter can be calculated as described in Equation 1.1.

$$S_{ij} = \left. \frac{V_i^-}{V_j^+} \right|_{V_k^+=0 \; for \; k \neq j} \tag{1.1}$$

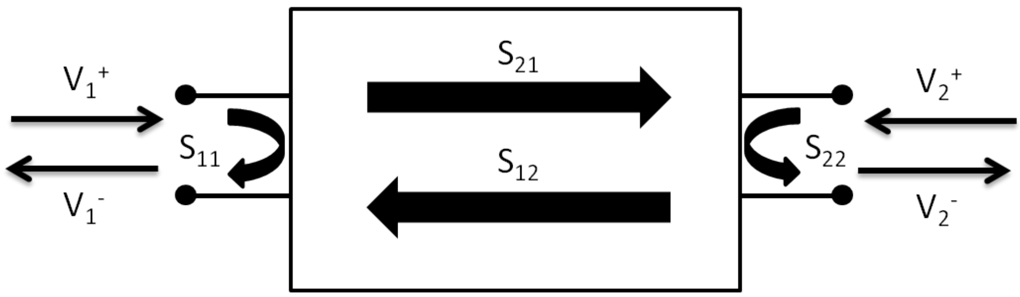

Figure 1.11. An arbitrary 2-port microwave device [66].

The single scattering parameter relative to one port is equal to the ratio of the incident wave to the reflected wave when all the incident waves on the other ports are set to zero. Antennas are usually 1-port microwave devices, where the S_{11} parameter represents the reflection coefficient. The reflection coefficient is usually measured in dB. The frequency bands where the reflection coefficient is below -10 dB represents the antenna bandwidth. For a system of two antennas, the S_{21} parameter represents the amount of the input wave from antenna 1 that reaches the terminal of antenna 2. The S_{21} parameter contain several pieces of information such as the antennas' matching and radiation properties, the channel loss and multipath effects.

1.6.2. Radiation Pattern, Directivity, Gain, Realized Gain

The radiation pattern is defined as a mathematical function of the radiation properties of an antenna as a function of the spatial coordinates [67]. Radiation properties include directivity, gain and realized gain. The directivity can be defined as the ratio of the radiated power density toward a particular direction (θ,ϕ) to the radiation intensity of an isotropic antenna. The directivity is defined in Equation 1.2.

$$D = \frac{4\pi U(\theta, \phi)}{P_{rad}} \tag{1.2}$$

where U is the radiation intensity and P_{rad} the total power radiated. Usually the directivity is calculated considering the maximum radiation intensity (U_{max}). The gain is a parameter correlated to the directivity but that includes the effects of the antenna loss. Finally the realized gain takes in account the antenna directivity, losses and mismatches.

1.6.3. UWB Pulse Signals

There is no mandatory pulse shape required in the UWB standard [10, 68] but the chosen signal must comply with the spectral mask defined in the

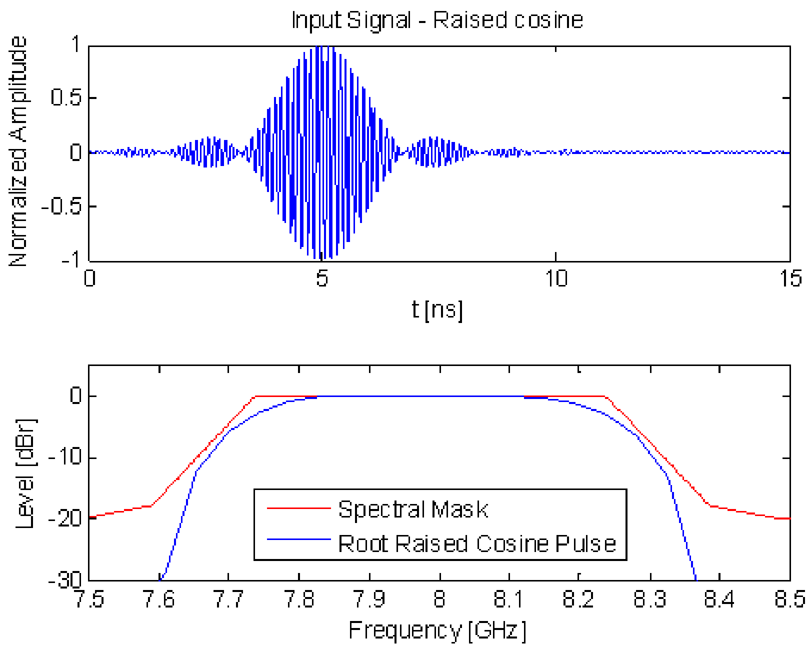

Figure 1.12. Time domain shape of the root raised cosine pulse modulated at 7.9872 GHz with roll off equal to 0.5 and 499.2 MHz bandwidth and comparison of the UWB spectral mask with the signal spectrum.

standard. This signal can be a Gaussian pulse or one of its derivatives. A signal that perfectly complies with a given mask is the Root Raised Cosine (RRC) because its spectrum is a well-matched fit due to the bell-like spectral shape [69] in comparison to the many derivatives of Gaussian pulses. An example of modulated RRC pulse is shown in Fig. 1.12.

1.6.4. Fidelity Factor

The Fidelity Factor (FF) [70] is a parameter that compares the shape of two pulses and is defined as in Equation 1.3 as the maximum absolute value of the cross-correlation coefficient between two signals., where $x_1(t)$ and $x_2(t)$ represents the signals.

$$FF = max \left| \frac{\int_{-\infty}^{+\infty} x_1(t) * x_2(t+t_d)dt}{\sqrt{\int_{-\infty}^{+\infty} |x_1(t)|^2 dt}\sqrt{\int_{-\infty}^{+\infty} |x_2(t)|^2 dt}} \right| \tag{1.3}$$

The fidelity factor is an important parameter used in radar applications. It takes into consideration the shape of the signal, neglecting the amplitude. For this reason it is important to take the near electric-field into consideration as well as the far-field radiation pattern. The pulse shape can be distorted by several factors [71]:

- the receiving and transmitting antennas' capability to preserve the same shape for the transmitted pulse in different directions;
- the dispersive materials in close proximity to the receiving and transmitting antennas;
- the different media in which the electromagnetic waves propagate;
- constructive and destructive interference.

Different frequency components travel at different speeds in dispersive media, distorting the resulting signal. The transmitted pulse shape depends on the antenna near field, and in particular, on the medium in close proximity to it, because of the influence on the antenna input impedance. The antenna can also have different resonances in different areas as a function of its geometry, resulting in different transmitted pulse shapes for different directions. Considering the IEEE Standard on WBAN [10], the required fidelity factor for a reliable communication has to be greater than 0.8.

1.6.5. Group Delay

Another parameter to characterize the antenna dispersion is the group delay. The group delay is defined as the negative derivative of the phase of the transfer function of a given channel with respect to the angular frequency, as defined in Equation 1.4.

$$\tau(w,\theta,\phi) = -\frac{d\psi}{dw} \tag{1.4}$$

where ψ represents the phase of the transfer function of the channel, described in Equation 1.5.

$$H(w,\theta,\phi) = Gain(w,\theta,\phi)e^{i\psi(w,\theta,\phi)} \tag{1.5}$$

The group delay parameter is used to quantify the delay of the different frequency components and it is more often used for two-port devices such as filters or amplifiers. FF is a parameter to compare the shape of two different signals and it is directly used as a design goal in different UWB standards [10, 68] for BAN.

1.7. Conclusions

In recent years, there has been a notable increase in research on antennas for on-body communications. The on-body research investigated the effects of the human body on the antenna performance and the main objective was to provide a reliable communication link between sensors or to a hub. Also the effects of human body absorption of electromagnetic energy is considered, to establish a safety limit on the maximum power. New applications including imaging and hyperthermia emerged. The antenna designs were mainly based on upper limbs. The antennas located on the footwear were at ankle height and mostly used for channel characterization. Different technologies were investigated, from narrowband to wideband technologies. No work is reported on antenna design for footwear which considers ground proximity and foot/shoe models or numerical phantoms. Many questions have arisen, which are not completely answered. The antenna locations on footwear are constrained by various problems, such as the ground proximity and the spatiotemporal characteristics of human gait, which alternates the channel between line-of-sight (LOS) and non-line-of-sight (NLOS) scenarios. However, footwear has the advantage of a larger available surface to locate the antenna and the electronics and the possibility to focus the radiated beam in one direction.

This thesis aims to develop different antenna technologies enabling reliable communication with on-body sensor devices. For the first time UWB antennas are studied in the time- and frequency-domain for on-body communication. Novel solutions are found for the antenna integration considering the effects of body and ground proximity.

2. Methodology

2.1. On-Body Models

2.1.1. Electrical Properties

Antennas for on-body networks must consider the surrounding environment. The human body is usually most influential on the antenna performance unless there is close proximity to metallic enclosures or batteries. The human body model is a complex combination of different media, which can be characterized as low and high water content tissues. The low water-content tissues include fat, bones and cartilage which are characterized by low permittivity and low losses. The high water-content tissues include muscle, skin and brain and are characterized by high permittivity and high losses. One of the first attempts to measure the dielectric properties of body tissue was made by Durney et al. in 1986 [72]. It is not easy to characterize the electrical properties of the human body materials. The problem is related to the measurement technique, which requires contact measurements that is not possible for live tissue. To overcome this problem, dead tissue or animal tissue were analyzed [73]. Gabriel et all [73] made an accurate and broadband analysis of the human body materials. Because the electrical properties are frequency dependent, a 4-Cole-Cole equation is required [73], shown in Equation 2.1.

$$\epsilon(w) = \epsilon_\infty + \sum_{m=1}^{4} \left(\frac{\Delta\epsilon_m}{1 + (jw\tau_m)^{1-\alpha_m}} + \frac{\sigma_j}{jw\epsilon_0} \right) \tag{2.1}$$

where

- ϵ_∞ is the material permittivity at terahertz frequency;
- ϵ_m,τ_m,α_m are material parameters for each dispersion region;
- σ_j is the ionic conductivity.

In [74] it is possible to obtain the electrical properties for each body tissue. The human foot and ankle is characterized by 26 bones, 33 joints and more than 100 tendons, ligaments and muscle. Also the thin layer of skin and fat has to be considered, with blood vessels and nerves.

2.1.2. Numerical Phantom

A numerical phantom is important to model the effects of the human body on the antenna performance. Two different numerical phantoms can be used:

- a homogeneous phantom;
- a voxel model.

The homogeneous phantom is a geometrical shape in which electrical properties are modeled as an on-body material. It can be:

- anatomical shape, resembling the human body;
- layers of canonical shapes such as bricks or cylinders.

While the anatomical model is more suitable for high frequency antennas because of the more specific shape that can produce shadowing and diffraction phenomena, the stacked homogeneous or heterogeneous structure is used as a simple model, saving computational power. An anatomical model can be obtained by graphic software such as Make Human [75], which enables the creation of different human body models with different

Figure 2.1. Example of an anatomical homogeneous human body model.

global and local features. The global features includes the height, weight, age and gender of a person. The local features include the diameter and length of each limb and different body parts. An example of the model from Make Human software is shown in Fig. 2.1.

The model in Fig. 2.1 represents a human body model with the arms perpendicular to the body. The body posture can be modified using another program, Blender [76]. In this case the human body joints can be rotated, and different postures can be modelled as a subject walking, running, lying down, etc. Some examples of Blender models are shown in Fig. 2.2.

A voxel represents the smaller 3-dimensional element of the voxel numerical phantom. A numerical voxel phantom provides high detailed sections of the human body such as the internal organs, bones, etc. These models are obtained from medical imaging techniques, such as magnetic resonance imaging and X-ray computer tomography. The drawback of these models is the requirement of high computational power. CST microwave studio allows the use of the CST voxel family. An example of a voxel model with different layers is shown in Fig. 2.3.

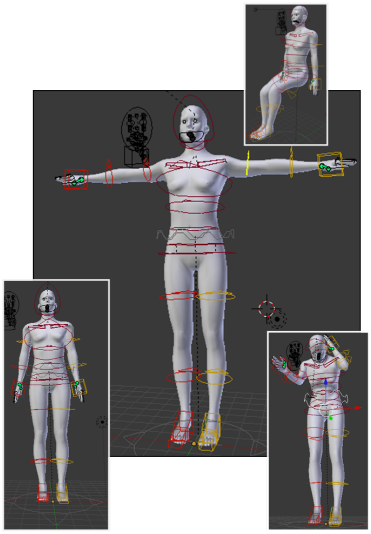

Figure 2.2. Different body postures created with Blender software.

An important characteristic of the voxel model is the voxel resolution. The smaller the voxel resolution, the more accurate the model and more computational power is required. Voxel models are used mainly for elec-

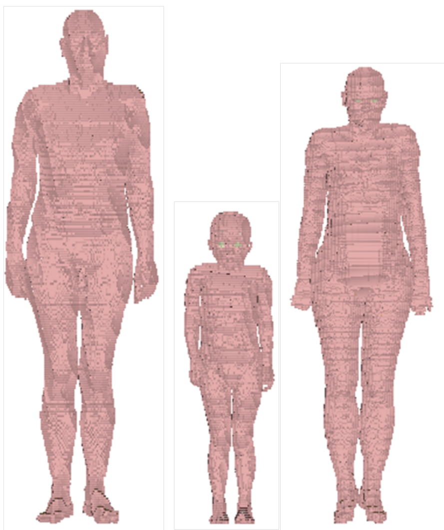

Figure 2.3. CST voxel family : Gustav, child and Katia.

Figure 2.4. CST model of skin, muscle, fat and bones of the Gustav phantom foot model.

tromagnetic dosimetry, radio frequency imaging and specific absorption rate simulations. A section of the CST voxel family representing the foot is shown in Fig. 2.4. Locations near the ankle are characterized by a high concentration of muscle, whereas locations on the toes are characterized by more bones.

2.2. Antenna Design Approach

The antenna radiation mechanism is influenced by the close proximity of the body, in particular the input impedance and efficiency of the antenna. The degradation of radiation efficiency depends on the lossy properties of the body tissue and the resonant frequency shift depends on the relative permittivity [18]. These effects are functions of the body-antenna separation.

In this thesis all the antennas are optimized considering the application and their location on the body. An antenna with a ground plane between the radiating element and the body are less sensitive to the body presence. However such a structure is complex and it is not easy to integrate on the footwear surface. Single-sided antennas on semi-flexible dielectric substrate are used in this work. This leads to easy integration of the antenna on the shoe surface or inside the shoe material. Particular care is necessary for the antenna geometry design. Complex shapes including spirals, exponential curves or splines are required for the radiating and the ground plane elements to provide a -10 dB broadband impedance match.

2.3. Simulation Software

The design and optimization of complex antenna shapes in close proximity to the human body requires advanced software tools. Maxwell's equations can be solved using various numerical methods.
The method of moments is a technique to solve the integral form of Maxwell equations reducing them to simple linear equations. The method is useful for canonical shapes and non-dispersive electrical properties.
The finite element method is a numerical model that can be used for complex geometries, but it demands high computational power. It divides the domain space into a finite number of elements of various shapes, such as rectangles or triangles. For each element the field is expanded in terms of a set of basis polynomials, weighted as a function of the field intensity. Finally a matrix eigenvalue equation is obtained and solved. This method is suitable for complex structures, but the matrix solution is time consuming.
The finite difference time domain method was developed by Yee in 1966, which also divides the model into small cells as in the finite element method. The Maxwell equations are discretized to space and time domain partial derivatives. From the excitation origin the field is expanded to the adjacent cells, as a function of the boundary conditions. This method can be used for inhomogeneous and complex models and it is less complex compared

to the previous technique.
CST microwave studio is a commercial simulation software tool which directly solves the differential equation with the finite integration technique. It enables fast and accurate simulation of complex electromagnetic structures with a user-friendly computer aided design. The finite integration technique is a consistent discretization technique scheme to solve Maxwell's equations in their integral form [77]. CST microwave studio includes an adaptive mesh technique which increases the mesh numbers until the errors are minimized. In this thesis CST microwave studio is used because it allows a fast and reliable solution for complex antenna geometries in close proximity to the human body. In order to validate the simulation results, an implementation of the proposed antenna arrangement is always performed.

2.4. Specific Absorption Rate

The specific absorption rate (SAR) is a parameter to quantitatively characterize the power absorbed by body tissues. Initially the human-antenna interaction was confined to the effects of the handset antennas on the human head. The advent of wearable technologies extended the SAR investigation to different body locations. The SAR is described by Equation 2.2.

$$SAR = \int \frac{\sigma(r)|E(r)|^2}{\rho(r)} dr \tag{2.2}$$

where

- σ is the body tissue electrical conductivity;
- E is the RMS electric field;
- ρ is the body tissue density.

The SAR depends on the antenna proximity, on the body tissue composition and shape and on the transmitting power. There are different SAR regulations:

- ICNIRP guidelines for Europe [78];
- IEEE C95 guidelines for United States [79].

There are different definition for the SAR:

- The point SAR is the local SAR calculated without mass or volume averaging;
- The total SAR is the total power loss divided by the total mass;
- The mass averaged SAR is the calculated SAR averaged on a particular quantity of mass, typically 1 g or 10 g;
- The volume averaged SAR is the calculated SAR averaged on a particular quantity of volume.

Although the limits vary from country to country, the 10 g mass average SAR limit for the foot area is equal to 4 W/Kg in Europe and United States.

2.5. Propagation Models for On-Body Communication Links

The on-body scenario is a complex environment where the waves can propagate in different ways. This is due to the electrical and geometrical complexity of the human body. It is important to consider many different propagation scenarios to guarantee a reliable communication link for different body postures and compositions between two nodes located on the body. Generally, the propagation path between on-body nodes can be:

- a line of sight link;
- multipath propagation;
- on-body paths.

Line of sight links include the links where a direct link is possible between nodes located on the body surfaces. This type of link is not always possible and depends on the antenna radiation pattern shape and on the body posture. Some examples include the link between wrist and footwear or between the waist and the toe cap. Usually the channel gain is much higher for this type of body-link compared to other cases, but it is not possible for all the combinations of body location nodes.
The multipath propagation case includes links that depend on the surrounding environment. The best results for this kind of propagation are when the antenna radiation pattern is directed away from the body surface. This kind of propagation leads to a channel gain sometimes greater that an on-body path channel gain, as demonstrated in [20], but it is strictly dependent on the surrounding environment, which must offer multiple propagation paths. It is characterized by high fading and it is difficult to create a general model that is valid for every case.
The on-body propagation is defined as a path where the waves are bound to the human body and which propagates with low attenuation around the body contour [80]. In [81], an analytical description of the surface wave propagation based on Sommerfield's definition is made when applied to human bodies tissues. A surface wave propagates along a boundary between two different media. In contrast to the radiating wave, in this case the wave is bound to one of the media. The wave attenuation depends on the loss properties of the medium. Surface waves always propagate at a speed slower than that of free-space and hence are defined as slow waves. The phase velocity depends on the boundary conditions. Surface waves depend on the electrical properties of the medium, so they are often dis-

persive. A Norton wave is the propagating electromagnetic wave produced by a source over or on the ground [82]. In [80], the surface wave TE and TM mode is obtained for a multilayered human body model. The definition is based on an oblique plane wave incident on dielectric slabs and their transverse wave impedances. The condition of existence for a surface wave is a vanishing reflection coefficient at any boundary. If the surface is characterized by a capacitive impedance, a TE mode is supported. If it is an inductive surface, a TM mode is supported. If the planar wave is characterized by a vertical component of the E-field, there are less electrical losses compared to the complementary polarization. In this case there is no low frequency cut off, but there is a high frequency cut off. To excite a surface wave the radiator must be located near the planar boundary. In [83], it was demonstrated that a vertically and horizontally polarized antenna can launch a TM Norton wave and that a vertically polarized antenna excites stronger waves. The surface wave propagation depends also on the metallic objects located on the body surface, which can impair or improve the channel gain [84].

2.6. Conclusions

In this chapter the methodology used in this thesis was introduced. The design of antennas for footwear telemetry is a complex subject where different elements must be taken into account. The human body plays an important role for the antenna design. The different approaches to the body models are shown, with particular emphasis on the material characterization and on the model type. To characterize the human body for different postures, different tools are used although they are limited to anatomical dielectric shapes. For SAR simulations voxel models are required. The antenna design approach is shown and how the human body affects the antenna performance. The main numerical techniques are compared and CST microwave studio was chosen to model the antenna/body arrangements. Finally the different propagation modes for on-body communication are described.

3. Investigation of Antenna Polarization Issues for On-Body Line-of-Sight Communications

3.1. Introduction

On-body perpendicular polarization is proposed in many papers [18, 20] because of the superior surface wave capability to creep around the body surfaces. Different studies are focused on the investigation of the best polarization for on-body communication but some are limited to the 2.45 GHz frequency [85], to the distances between the antennas [86] and to non-line-of-sight (NLOS) UWB channel investigation [87].

However there is no evidence to suggest that an antenna with a polarization tangential to the body surface behaves worse than an orthogonal polarization across all frequencies and for each body-to-antenna separation considering line-of-sight (LOS) communication link. There are some studies that acknowledge the superiority of on-body perpendicular polarization with respect to tangential polarization [83], but none investigate it for a broadband channel.

Increasing the body-to-antenna separation is expected to decrease the coupling effects of the body on the antenna and the influence on the shape of the radiation pattern. This is valid for a LOS communication link, where the creeping characteristic of a surface wave is not required. In this chapter an investigation of a LOS link is made for the two different polarizations and for frequencies ranging from 4 to 10 GHz considering simulations and measurements of a halved Vivaldi antenna on a brick of water. In particular, the characteristic of the radiation properties of the two polarizations is investigated on a brick of water, and then the S_{21} parameter is analyzed for different water-to-antenna separations for a broadband range of frequencies.

E-field plots are used to show the different behavior of the electromagnetic wave propagation as a function of antenna polarization. A halved Vivaldi antenna was chosen because it is characterized by linear polarization and the radiation pattern is stable in the end-fire direction for different frequencies and for both orientations.

3.2. Antenna Free-Space Characteristics

The antenna described in this chapter is a halved Vivaldi antenna [88]. The halved Vivaldi antenna is made of a half flare Vivaldi antenna on a perpendicular ground plane as shown in Fig. 3.1.

The antenna dimensions described in this chapter are the results of the on-water antenna optimization. Two FR4 substrates of 1.4 mm thickness are used and soldered. The antenna dimensions are shown in Fig. 3.2 and

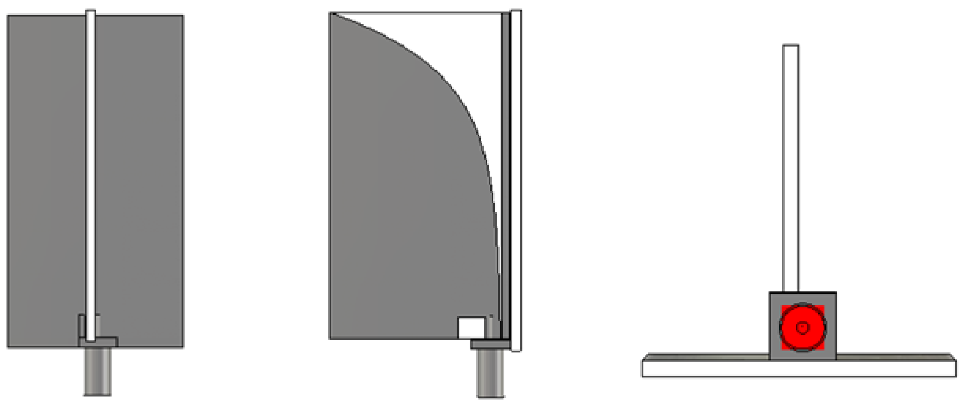

Figure 3.1. Top, side and front view of the halved Vivaldi antenna.

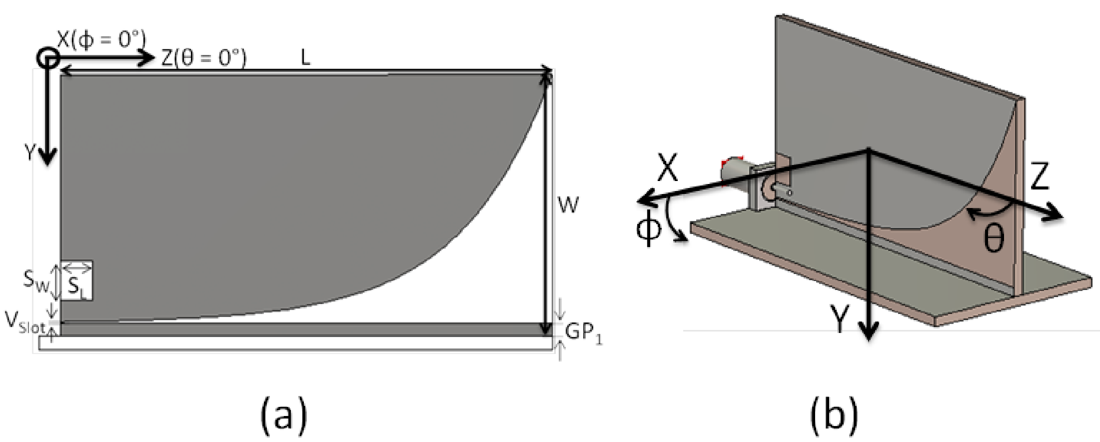

Figure 3.2. Geometry of the halved Vivaldi antenna without the connector (a) and reference system with the connector(b).

summarized in Table 3.1. The halved Vivaldi antenna is fed by an SMA connector on its side, as shown in Fig. 3.2 (b).

The Vivaldi flare follows Equation 3.1.

$$Y = 1.575 - 0.125(1 - e^{0.1z}) \tag{3.1}$$

with

$$0 < z < 54 \tag{3.2}$$

using the coordinate system described in Fig. 3.2.

There are different parameters to control the shape of the Vivaldi antenna. In particular the parameter z in the exponential curve controls the

Table 3.1. Dimensions of the optimized halved Vivaldi antenna.

Parameter	Dimension [mm]	Parameter	Dimension [mm]
W	29.13	S_W	4.36
L	54	S_L	3.55
V_{Slot}	0.22	GP_1	1.36

length of the Vivaldi line, and it tunes the maximum aperture of the antenna. The maximum aperture of the Vivaldi antenna should be equal to half the wavelength at the lowest operating frequency. The antenna growth rate is controlled by the exponential factor of the Vivaldi curve. The base of the exponential equation controls the Vivaldi initial slot, which is an important parameter to match the antenna impedance to the 50 Ω feed line.

A rectangular slot is added to the Vivaldi flare to increase the bandwidth and to separate the Vivaldi flare from the flange connector. The thin rectangular strip below the Vivaldi flare is used to better control the distance between the Vivaldi and the ground avoiding gaps. The ground on the second dielectric is 29.13 x 54 mm and it is the result of a trade-off between the lossy material coupling and the antenna size. The simulated and measured S_{11} and radiation pattern is shown in Fig. 3.3.

The antenna is chosen because of the end-fire radiation pattern, com-

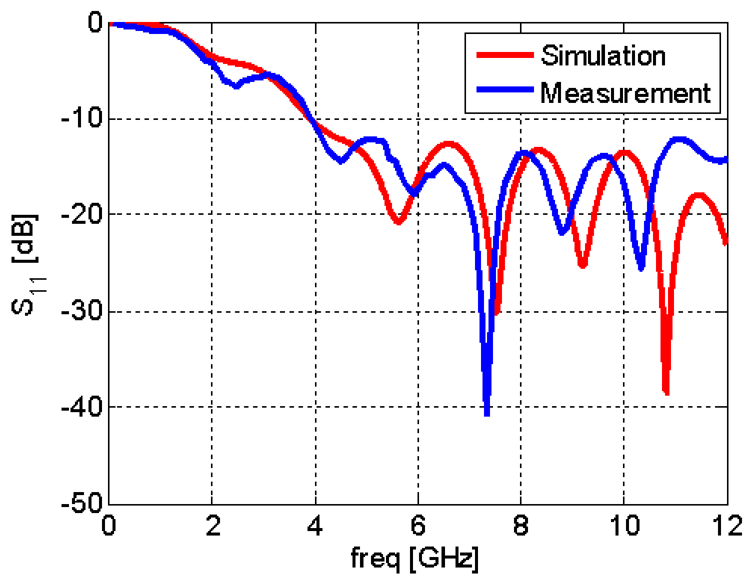

Figure 3.3. Simulated and measured S_{11} (dB) for the free space halved Vivaldi antenna.

pact size compared to a classic Vivaldi antenna and the linear polarization. Orthogonal and tangential polarization with respect to a surface can be achieved by rotating the antenna by 90°.

Different versions of the same antenna demonstrated that the thin strip line is critical to keep the antenna stable due to the solder along the antenna edge and to maintain a constant distance between the Vivaldi flare and the ground plane. The antenna reflection coefficient was found to be more sensitive to the water for a smaller ground plane. A larger ground plane doesn't improve the reflection coefficient of the antenna in the presence of the water.

The antenna is simulated with CST microwave studio. The simulation results are validated with the measurements on prototyped samples. There is a good agreement between the simulation and the measurement. The good match between the simulations and the measurements validate the choice of CST microwave studio and the antenna analysis doesn't require use of more numerical methods. The -10 dB antenna free-space bandwidth spans from 4 GHz to frequencies greater than 12 GHz for the simulated and for the measured data. The 3-D measured realized gain is shown in Fig. 3.4.

The radiation pattern is symmetric in the $\phi = 180°$ plane and asymmetric in the $\phi = 270°$ because of the presence of the ground. The maximum measured realized gain is equal to 9.2 dBi. The realized gain for $\theta = 0°$ direction is always greater than 2.9 dBi across the 4 GHz to 10 GHz bandwidth. There is a good agreement between simulated and measured radiation patterns as shown in Fig. 3.5.

Considering the 7 GHz and 10 GHz cases, the polar plots for the $\phi = 270°$ plane show that the main beam is tilted with respect to the $\theta = 0°$ direction because of the presence of the ground. Although the radiation pattern of the antenna is different for the two vertical planes, the realized gain is not characterized by any null in the end-fire direction in the 4-10 GHz bandwidth. This is important for our experiment because the end-fire di-

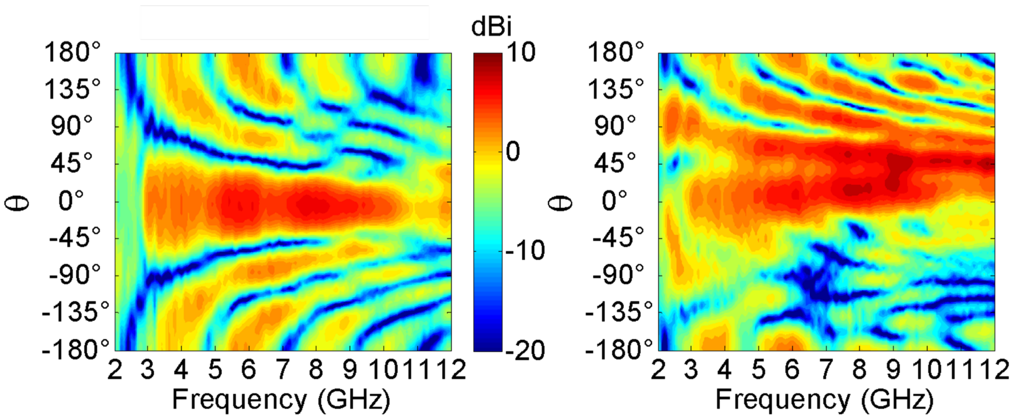

Figure 3.4. Measured absolute realized gain (dBi) for $\phi = 180°$ and $\phi = 270°$ cuts for the free-space halved Vivaldi antenna.

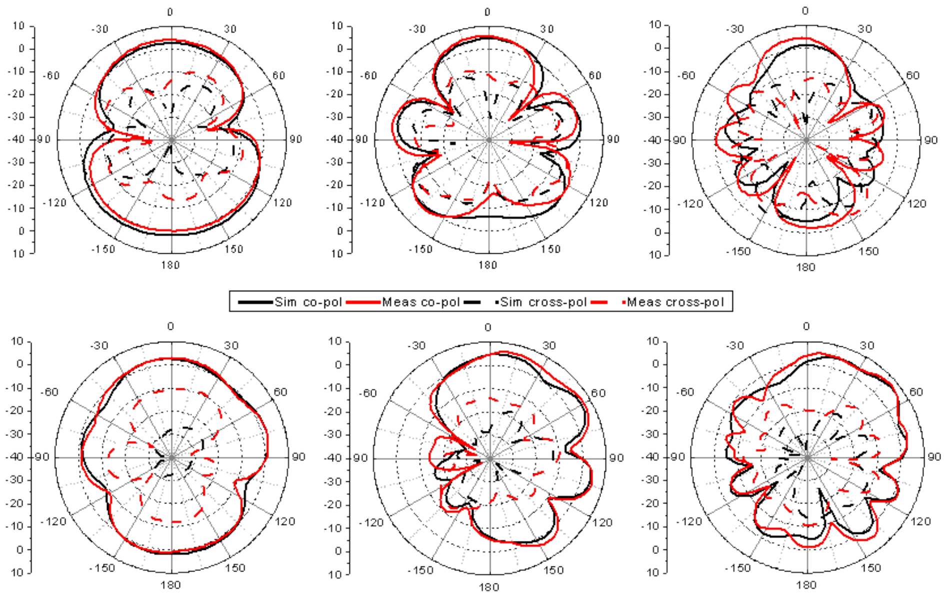

Figure 3.5. Simulated and measured co-polarized and cross-polarized realized gain patterns (dBi) for $\phi = 180°$ (first row) and $\phi = 270°$ (second row) at 4, 7 and 10 GHz for the perpendicular polarization for the free-space halved Vivaldi antenna.

rection has to be considered for LOS links. The antenna performances are investigated for two different polarizations with respect to the layer of the water:

- for polarization perpendicular to the water surface, the antenna ground is parallel to the water;
- for polarization parallel to the water surface, the antenna ground is rotated by 90°.

3.3. Antenna Characteristics when in Close Proximity to Water Surface

3.3.1. Motivation and Model Setup

Here, the performance of the antenna when in close proximity to a layer of water is investigated. The electrical properties of the water are very similar to the high water content human body tissues, as observed in Fig. 3.6 in case of muscle.

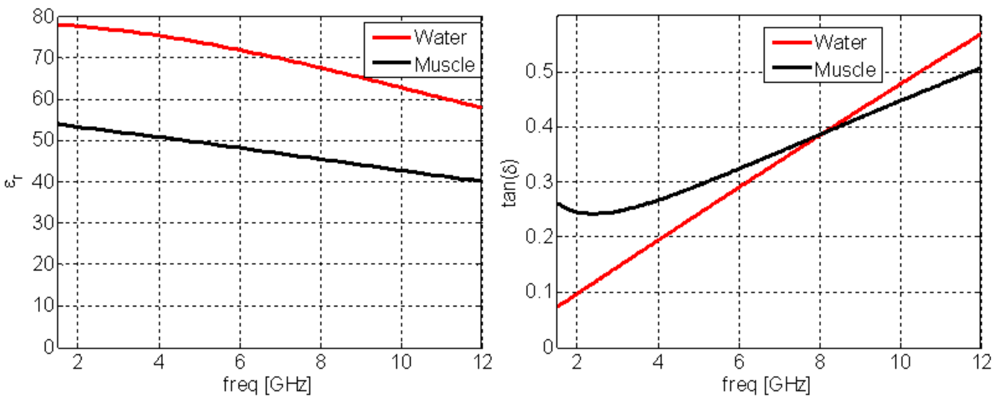

Figure 3.6. Relative permittivity and tangent loss for water and muscle.

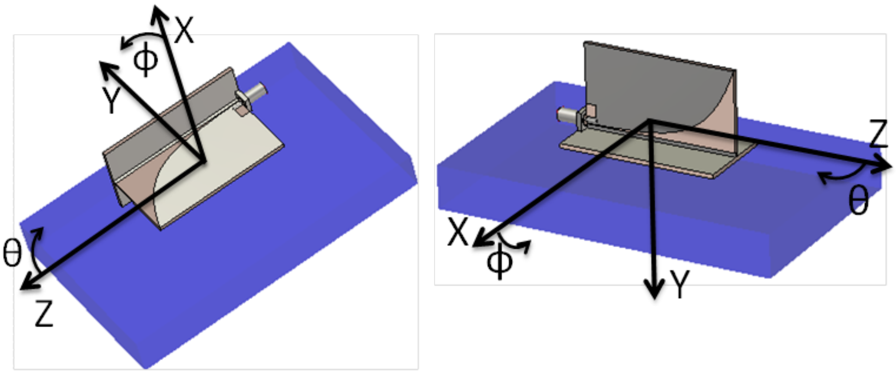

Figure 3.7. Halved Vivaldi antenna model for the parallel and perpendicular polarizations configuration.

The permittivity of the water is 40% greater than the muscle and the values of tangent loss are similar in the range between 4 and 12 GHz. Using water as dielectric represents a worst-case scenario with respect to a 2/3rd muscle permittivity phantom or a real human body. The electrical properties of the water with different salt concentration are well described in different papers [89–91] and it is relatively easy to set the electrical properties to target values. A reference model to represent the human body doesn't exist because real human body tissue changes from person to person, with age [92] and as a function of wet/humid environment. Using a homogeneous 2/3rd muscle phantom model or a three layers skin, fat and muscle model would lead to similar results, with small changes in the radiation pattern and impedance matching. Many studies demonstrated the equivalent behavior of three stacked human body tissue with equivalent homogeneous body tissue [93–95]. The two different configurations are shown in Fig. 3.7.

The separation between the antenna and the water layer is constant at 3 mm. The dimensions of the water layer are equal to 75 x 120 x 15 mm which correspond to λ x 1.5λ x $\lambda/5$ at 4 GHz and it represents a trade-off between simulation speed and results accuracy.

3.3.2. Perpendicular Polarization Case

The S_{11} parameter of the antenna for the perpendicular polarization is shown in Fig. 3.8. The antenna matching is better than -10 dB for the 4 GHz to more than 12 GHz bandwidth with the measured bandwidth wider than simulated. The measured bandwidth is shifted down by 1 GHz, with a -10 dB bandwidth from 2 to more than 12 GHz. With respect to the free space case, the lower edge of the -10 dB frequency band shifts down by 1 GHz in the simulation and 2 GHz in the measurement because of the close proximity of an high relative permittivity medium. Considering all the frequency range, the measured S_{11} was better matched than the simulated case. The frequency shift in the resonant frequency is due to a different length of the coaxial cable length, that is longer in the measurement system. No further numerical methods are required because the measured and simulated -10 dB bandwidth is from 4 GHz to 10 GHz.

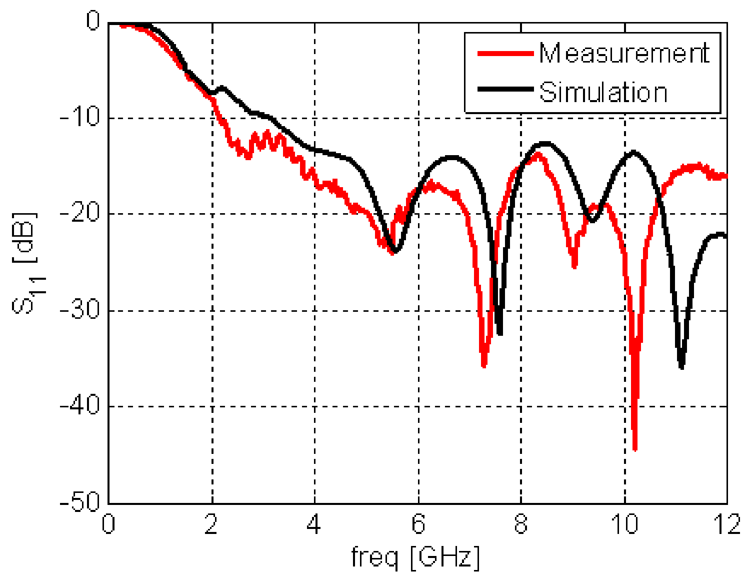

Figure 3.8. Simulated and measured S_{11} (dB) for the on-water halved Vivaldi in the perpendicular polarization configuration.

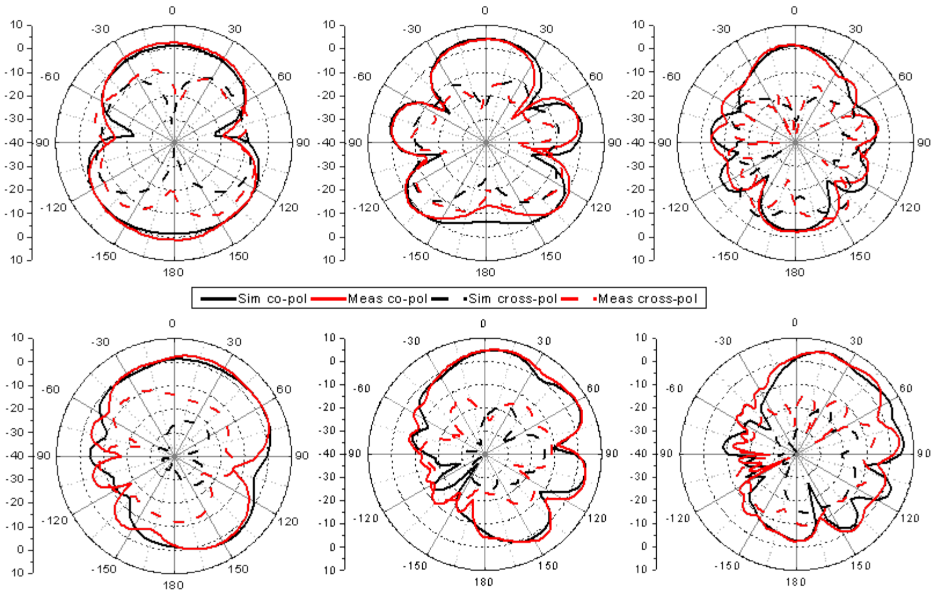

Figure 3.9. Simulated and measured co-polarized and cross-polarized realized gain patterns (dBi) for ϕ= 180° (first row) and ϕ= 270° (second row) at 4, 7 and 10 GHz for the on-water halved Vivaldi antenna in the perpendicular polarization configuration.

The radiation patterns are shown in Fig. 3.9, which are the same as the free-space case except for the slightly lower intensity of the realized gain. In particular the realized gain decreases more at 4 GHz, with a decrement of 1and less at 10 GHz, with a decrement of 0.1 dBi. The -3 dB beamwidth is not influenced by the presence of the water. For the perpendicular polarization the presence of the ground between the Vivaldi flare and the water limits the coupling with the water. The antenna cross-polarization is always better than 12 dB, making the antenna suitable for our experiment. The measured values of the realized gain are equal to the simulated values, validating the antenna geometry and the computation method.

3.3.3. Parallel Polarization Case

In this section the parallel polarization results are described. The simulated and measured S_{11} is shown in Fig. 3.10. The measured S_{11} is less than -10 dB from 4 GHz to greater than 12 GHz whereas the simulated S_{11} is -8.2 dB at the lower edge frequency. In this configuration the antenna is more sensitive to body proximity, with a degradation of the simulated reflection coefficient at the lower edge of the bandwidth. Also in this case the simulated resonant frequencies were shifted with respect to the measured values. As in the previous case, this is due to the longer cable in the measurements. However the resonant frequency doesn't impair the antenna performances, resulting in an antenna match for the required bandwidth.

The simulated and measured radiation patterns are shown in Fig. 3.11. The radiation pattern shapes are different compared to the free-space case. The main beam is no longer symmetrical but tilted above the groundplane

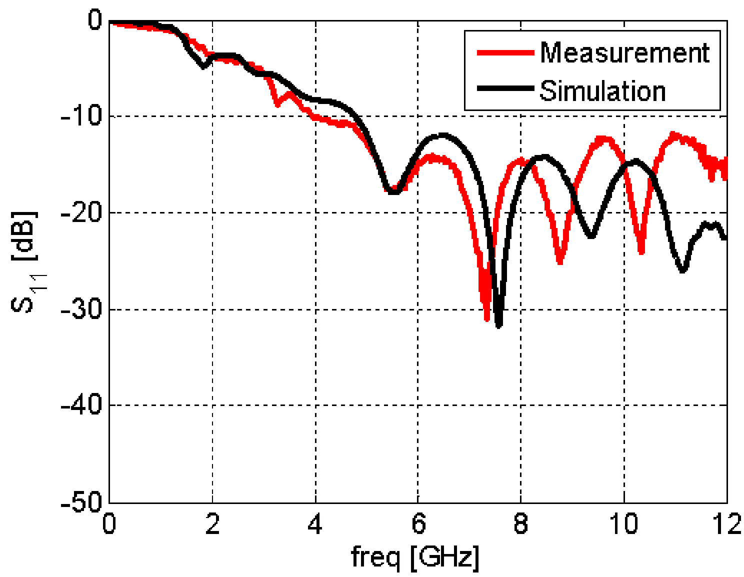

Figure 3.10. Simulated and measured S_{11} (dB) for the on-water halved Vivaldi in the parallel polarization configuration.

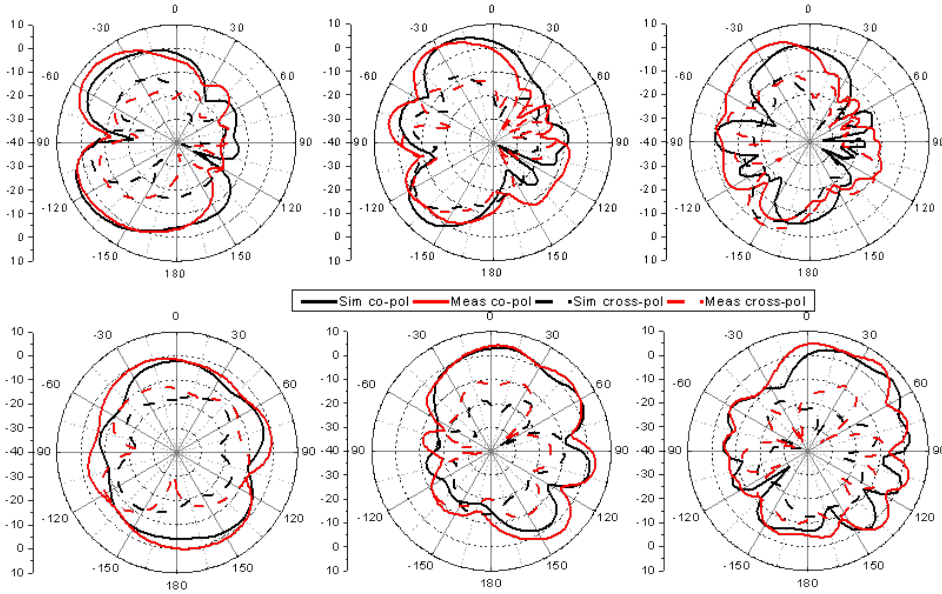

Figure 3.11. Simulated and measured co-polarized and cross-polarized realized gain patterns (dBi) for ϕ= 180° (first row) and ϕ= 270° (second row) at 4, 7 and 10 GHz for the on-water halved Vivaldi antenna in the parallel polarization configuration.

of the antenna and above the water surface. Comparing the E-plane of the free-space antenna (ϕ = 180°) and of the parallel polarization (ϕ = 180°) it is clear that the water layer influences the shape of the radiation pattern, resulting in a tilted beam. The simulated and the measured realized gain for the two planes is smaller with respect to the free space case and the perpendicular polarization case. Also in this case the simulated radiation pattern shapes are close to the measured ones. The cross-polarization is always better than 10 dB. Considering the overall system performance for the parallel polarization, a smaller realized gain has to be considered in the end-fire direction with respect to the perpendicular polarization when the S_{21} results will be compared.

3.4. Simulated Transmission between Two Vivaldi Antennas on Water Layer

The transmission between two halved Vivaldi antennas is modelled for different LOS body-to-antenna separations in the 4 to 10 GHz frequency band. The perpendicular and parallel polarization models are shown in Fig. 3.12.

The distance between the two antennas is 30 cm and the separation between antenna and water is varied from 3 mm to 33 mm. The distance between the antennas corresponds to 4 wavelengths at 4 GHz considering free-space conditions. The dimensions of the water layer are equal to 437 x 80 x 15 mm. The simulated S_{21} is shown in Fig. 3.13 for four different cases:

- both the Vivaldi antennas are parallel polarized;
- both the Vivaldi antennas are perpendicular polarized;
- one antenna is parallel polarized and the second antenna is perpendicular polarized;

Figure 3.12. Simulated model of the two halved Vivaldi antennas on the water layer for the perpendicular and parallel polarization.

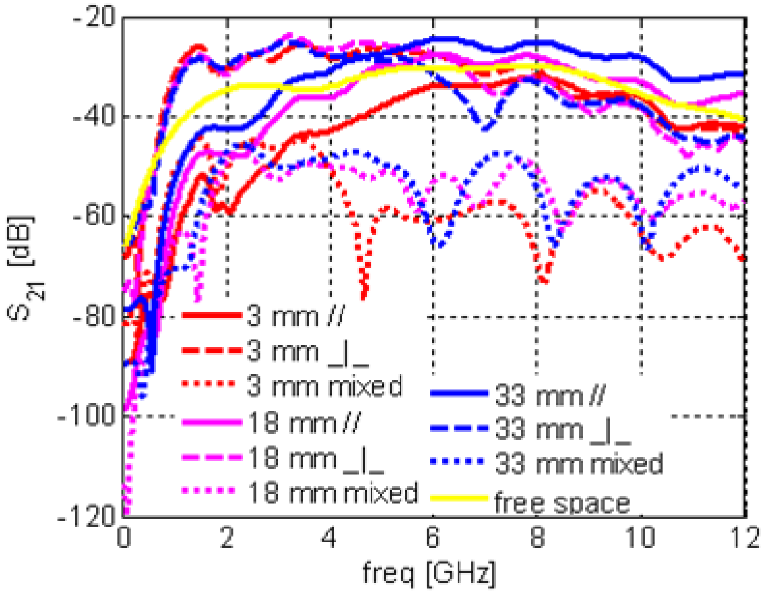

Figure 3.13. Simulated S_{21} (dB) for perpendicular, parallel and mixed configuration on a layer of water for different antenna/water separations and water-less case for same polarization case.

- the two Vivaldi antenna have the same polarization without the water.

The propagation path (S_{21}) in the presence of water for the perpendicular configuration is better than the free-space case, for small antenna-to-water separations and for low frequencies. Increasing frequency and increasing the body-to-antenna distance improves the performance of the parallel configuration compared to the perpendicular case. When the two antennas are not polarization matched, the performance is degraded, as expected. This corresponds to the worst performance, because the S_{21} intensity is due to the cross-polarized components of the two parallel and perpendicular polarizations. The presence of the layer of water improves the wave propagation at low frequency and for small distances.

Table 3.2 summarizes the frequency (f_x) for which the parallel polarization S_{21} is better than perpendicular polarization for different body-to-antenna distances with the average path loss values over the 4 to 12 GHz bandwidth.

Table 3.2. Simulated f_x and average path loss for perpendicular, parallel and mixed configuration.

Antenna-Water Separation	f_x [GHz]	Average Path Loss [dB] over 4 to 12 GHz		
		Parallel	Perpendicular	Mixed
3 mm	8.2	36.6	33.4	61.1
18 mm	6.14	31.6	34.6	54.5
33 mm	4.56	27.7	36	53.5

With increase of the antenna-to-body distance, f_x becomes smaller. The average path loss decreases by increasing the antenna-water separation distance because the antenna becomes more efficient for the parallel configuration. Considering that the antenna in the perpendicular configuration is less sensitive to the water proximity, the efficiency improvement as a function of the antenna-to-water distance increment is not as great as the parallel polarization case. The average path loss is greater for the parallel polarization than the perpendicular polarization for small antenna-to-water separation, but it becomes smaller than the perpendicular case with increasing separation. In Fig. 3.14 the normalized E-field for the perpendicular configuration with 3 mm separation is shown for 4 and 10 GHz. It can be observed that there is an E-field component all along the water layer surface to the receiving antenna. The electric field interacts with the medium, helping the propagation of the wave along the end-fire direction of the antenna. At 10 GHz the penetration of electric field into the layer of water is smaller compared to the 4 GHz case. In Fig. 3.15 the E-field for the parallel configuration at a separation of 3 mm is shown.

In this case the E-field intensity is large in a portion of the water layer just below the antenna, but the field doesn't interact with the water layer and is then reflected away from the water surface, particularly at the lower frequency of 4 GHz. However, at 10 GHz, the reflection angle is smaller, and the beam illuminates the second antenna, decreasing the path loss.

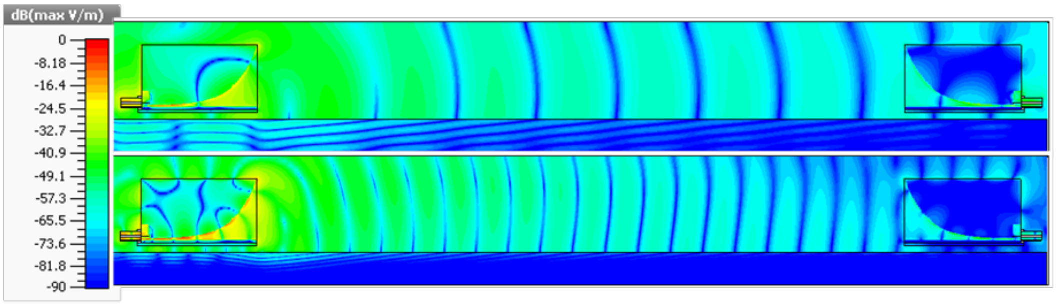

Figure 3.14. Absolute normalized simulated E-field for the perpendicular polarization case at 4 GHz (top) and 10 GHz (bottom) for a separation of 3 mm.

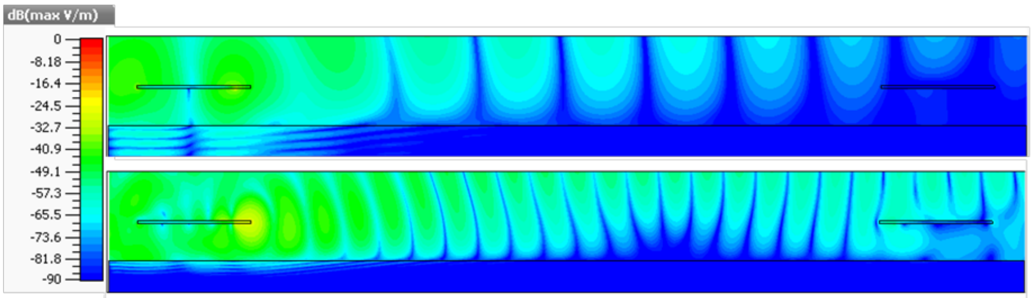

Figure 3.15. Absolute normalized simulated E-field for the parallel polarization case at 4 GHz (top) and 10 GHz (bottom) for a separation of 3 mm.

3.5. Measured Transmission between Two Vivaldi Antennas on Water Layer

Measurements of two Vivaldi antennas on a layer of water are presented. The measurement setup corresponds to the simulated model described in the previous section. The S_{21} results for the different polarizations are shown in Fig. 3.16. The simulated average path loss is smaller than the measured one. Table 3.3 summarizes the frequency where the parallel polarization S_{21} becomes better than perpendicular polarization for different body-to-antenna distances.

Discrepancies between the simulated and measured values are due to

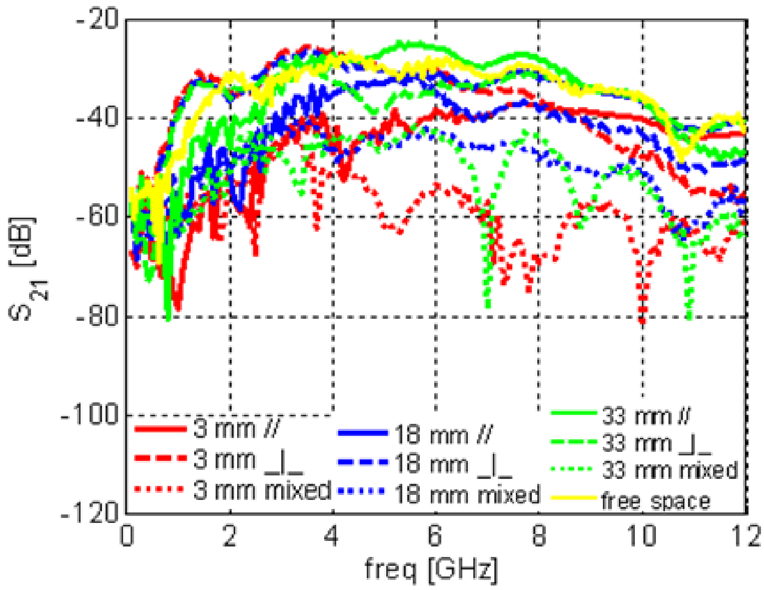

Figure 3.16. Measured S_{21} (dB) for perpendicular, parallel and mixed configuration on a layer of water for different antenna/water separations and water-less case for same polarization case.

a non-perfect alignment between the two antennas and to challenges to control the antenna-to-water separation.

Also in the measurements the perpendicular polarization is characterized by a greater S_{21} at low frequency and for low antenna-water separation with respect to the parallel polarization case. The difference in f_x between the simulation and the measurement is equal to 200 MHz for small

Table 3.3. Measured f_x and average path loss for perpendicular, parallel and mixed configuration.

Antenna-Water Separation	f_x [GHz]	Average Path Loss [dB] over 4 to 12 GHz		
		Parallel	Perpendicular	Mixed
3 mm	8.4	40.8	39.5	61.4
18 mm	5.25	34.9	39.4	49.5
33 mm	3.5	32.9	35.5	51.9

antenna-water separation and increases with the distance. No further simulation models are required because the obtained f_x is very close to the measured values. Also in the measurement the performance for the mixed configuration is worse, as expected. In this case the path loss increases when the antennas are closer to the water layer.
While in [83] it is stated that a vertical E-field is characterized by greater intensity, in this study it was demonstrated that this is not always valid, but that it is function of the electrical distance between the antenna and the media.

3.6. Conclusions

In this chapter a halved Vivaldi antenna was optimized to operate in close proximity to materials with high relative permittivity and loss tangent values. A LOS link is investigated considering two different polarizations with respect to the surface of a water layer. For the first time it was shown that parallel polarization can perform better than perpendicular polarization under certain circumstances for a LOS links. Measurement and simulation results show that for higher frequency values and for large antenna-to-body separations the parallel polarization behaves better than perpendicular polarization. In particular an antenna with a polarization normal to a lossy and high permittivity material is able to excite a thin layer of current that improve the propagation at low frequency. If the distance between the antenna the material increases or if the frequency is above 8 GHz an antenna with a polarization tangential to the material is suggested for LOS communication.

4. Study of a Footwear to Wrist Channel

4.1. Background

Wearable technologies are electronic devices located in everyday garments and clothes. Sensors are placed in footwear to measure various biological parameters, including plantar pressure [96], speed [97], walking and running gait [98]. Different technologies are used for on-body communication links. They are mainly based on the 2.4 GHz frequency bands thanks to the several available technologies, such as bluetooth [99] , wi-fi [100], zigbee [101], etc. New emerging technologies have greater data rates and are characterized by an greater degree of security. Within this framework, UWB technologies are characterized by wider bandwidths, lower power consumption and smaller range in comparison to the narrowband systems. Because of these advantages, UWB is a promising technology for the development of Body Area Networks [28].
In this chapter the propagation channel between footwear and wrist is investigated for both narrowband and wideband channels in different frequency bands. A 0.2 mm single side FR4 monopole antenna is designed to cover the 2.4 GHz and the European UWB bands for on-body communications. The antennas are located on the footwear toe cap and on the wrist. Initially the free space and the on-body antenna performances are investigated functioning in the different locations. The simulated data are validated with measurements. Finally the antenna is used to characterize

the footwear to wrist channel for a walking subject for different frequency bands with different bandwidths. Results show how the multipath fading and the horizontal spread change in function of the chosen frequency and bandwidth. An antenna is designed to cover the 2.4 GHz and UWB bands and can be integrated with multimode transceivers to mitigate on-body multipath effects and to adjust the data rate to the particular request.

4.2. Antenna Design and Characterisation

The antenna is designed on single-sided 0.2 mm FR4 and optimized to be matched in close proximity of the human body. The geometry of the front and the side and a photograph of the manufactured antenna are shown in Fig. 4.1.

The antenna is fed by straight SMA connector located on one side of the PCB to facilitate integration on the toe cap surface. The antenna size is 40 x 50 mm and the dimensions of the splines are shown in Table 4.1.

A transition in the Coplanar Waveguide (CPW) is required for matching due to the connector flange. The widths of the feed line and slot line under

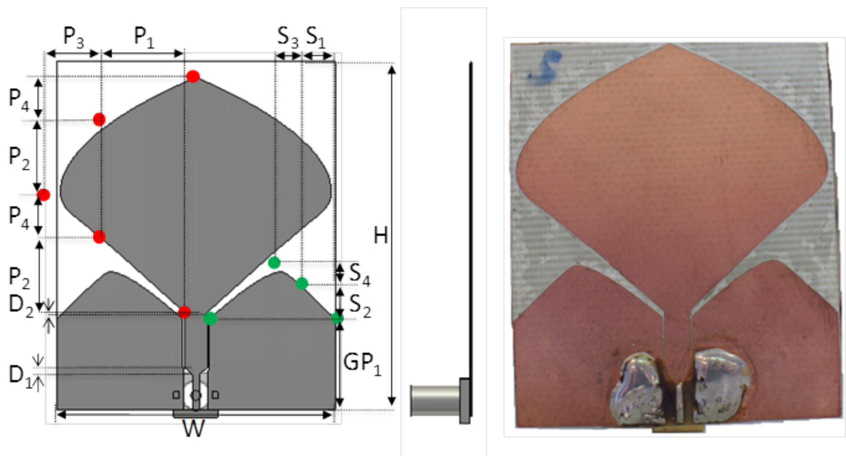

Figure 4.1. Geometry and dimensions of the optimized monopole antenna.

Table 4.1. Dimensions of the optimized monopole antenna.

Parameter	Dimension [mm]	Parameter	Dimension [mm]
P_1	12	S_1	5
P_2	11	S_2	5
P_3	8	S_3	4
P_4	6	S_4	3

the connector is 1 mm and 1.2 mm respectively. Beyond the connector, these become 3.3 mm and 0.2 mm respectively. The ground plane shape is also optimized to increase the bandwidth of the antenna with the dimensions GP_1 =13 mm , D_1=1 mm and D_2=0.8 mm . The antenna free-space reflection coefficient is shown in Fig. 4.2. In simulation, $S_{11} \leq$ -10 dB from 2.1 GHz to 10 GHz, whereas in measurement, it is from 2 GHz to 8 GHz. In the measurement there is a shift of the lower -10 dB frequency of 177 MHz.

The small disagreement between simulation and measurement is due to an imperfectly flat dielectric layer and non-uniform distance between the printed copper feed line on the dielectric of the CPW and the flange of the connector. The antenna on-body performance is evaluated for the footwear

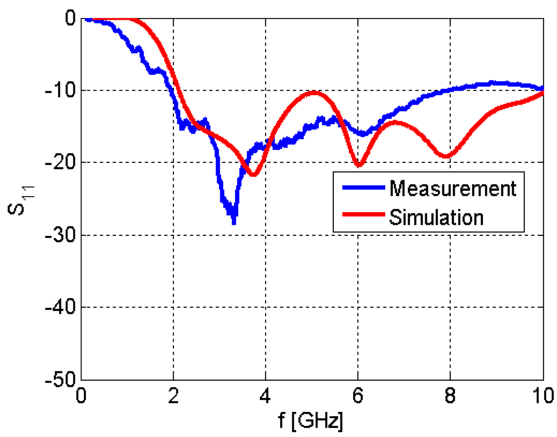

Figure 4.2. Free-space simulated and measured S_{11} (dB) for the optimized monopole antenna.

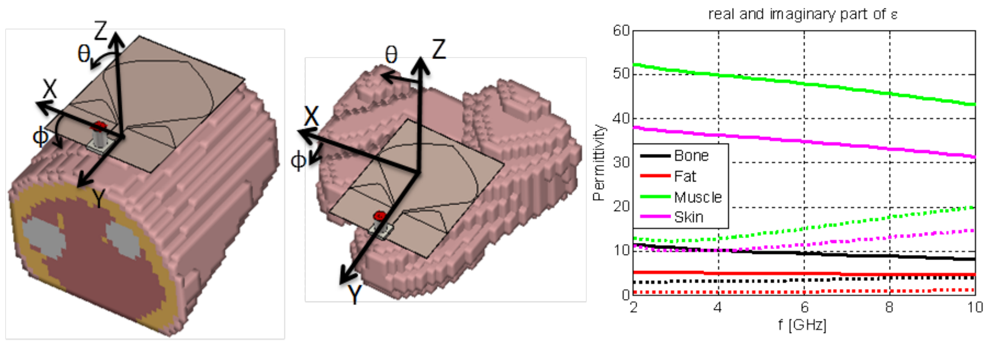

Figure 4.3. Optimized monopole antenna on wrist and foot and electrical properties for bone, fat, muscle and skin.

and the wrist locations. The simulation models include sections of the voxel files from the Gustav model [102]. The models with the antenna and the electrical properties of the different body tissues are shown in Fig. 4.3.

The foot and wrist models include different body tissues, such as skin, fat, muscle and bone. The electrical properties of these materials are frequency dependent [73]. The voxel file resembles the shape of the human body parts and it reproduces the internal geometry with a resolution of 2.08 x 2.08 x 2 mm. Considering the wrist case, the distance between the antenna and the body is 5 mm. The morphology of the foot voxel model is non-planar, so the distance varies from 0.5 mm to 9 mm considering the overall antenna dielectric surface. A comparison between simulation and measurements is shown in Fig. 4.4.

The shoe materials are not considered in the simulation model. The thin toe cap layer is negligible compared to the close proximity to the high dielectric constant and lossy body tissues. The measured S_{11} for the on-body antennas is less than -8.5 dB in the band of interest. Reasons for the differences between simulated and measured values may include differences in the shape of the voxel models, compared to the actual measured models. The antenna is perfectly centred on the wrist and the tissues are evenly distributed below the antenna. The toe loading in the footwear case is not

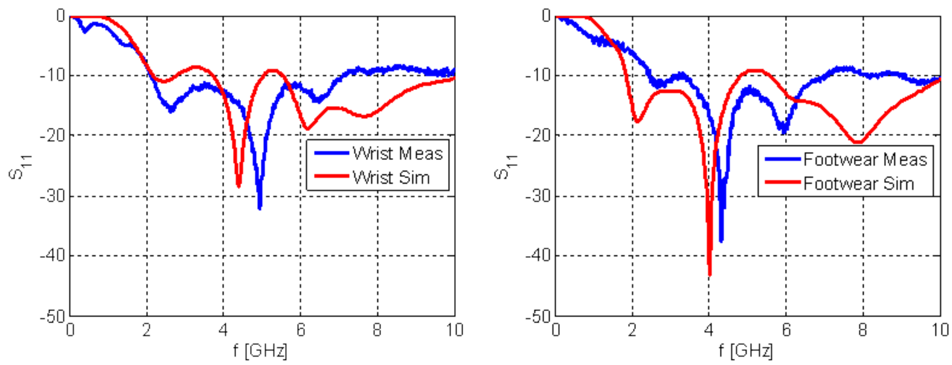

Figure 4.4. Simulated and measured S_{11} (dB) for the wrist and footwear on-body optimized antennas.

symmetrical, with air gaps and non-uniform antenna-foot spacing. The simulated radiation patterns are shown in Fig. 4.5 for the foot and Fig. 4.6 for the wrist.

The realized gain as a function of frequency is summarized in Table 4.2. The antenna radiation efficiency increases with frequency because the electrical distance between the antenna and the body increases. The difference in the radiation pattern shapes for the footwear and wrist locations is due

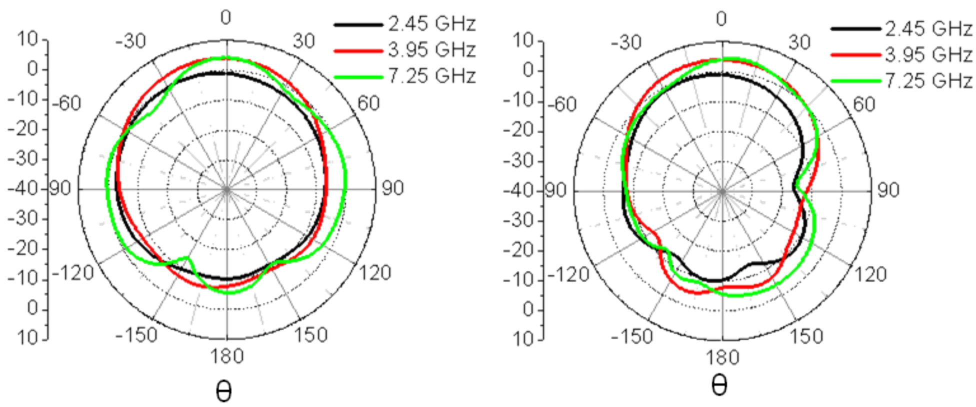

Figure 4.5. Realized gain patterns (dBi) for the optimized monopole antenna on footwear for $\phi = 0°$ and $\phi = 90°$.

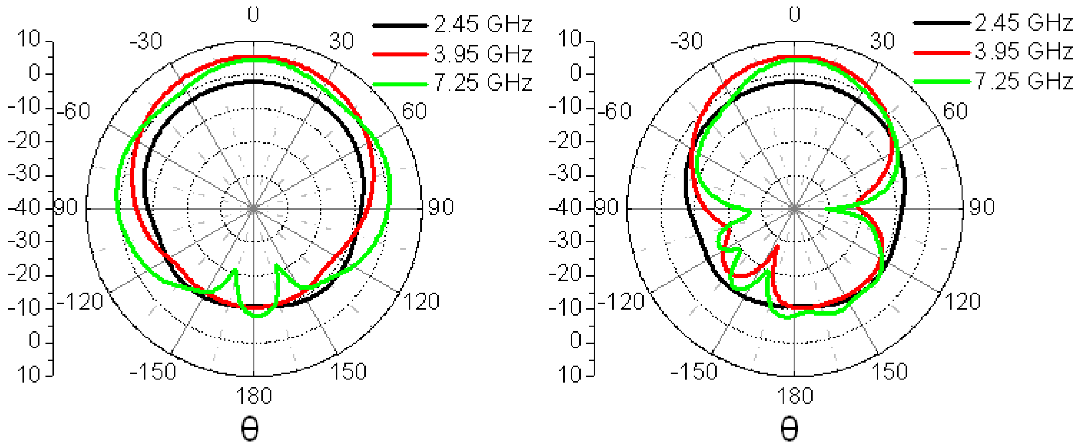

Figure 4.6. Realized gain patterns (dBi) for the optimized monopole antenna on wrist for $\phi = 0°$ and $\phi = 90°$.

to dissimilar body geometries and to the different positions of the antenna with respect to the body. The antenna exhibits the maximum realized gain for the wrist case at 3.95 GHz. Considering a walking person, the 3 dB beamwidth for $\phi = 90°$ for the footwear antenna is wide enough to cover the full swing cycle of the right arm. No further numerical models are required because all the simulated models are validated by measured performances with good match. For the purpose of the chapter, the antenna has to be matched in the investigated frequency range. This is demonstrated by the measured on-body performances.

Table 4.2. Directivity parameters for the on-body antennas.

Frequency [GHz]	Maximum Realized Gain Magnitude [dBi]		3-dB beamwidth for $\phi = 0°$ [deg]		3-dB beamwidth for $\phi = 90°$ [deg]		Radiation Efficiency	
	Wrist	Footwear	Wrist	Footwear	Wrist	Footwear	Wrist	Footwear
2.45	-2.09	-0.16	131.3	131.9	86.6	84.3	21%	30%
3.95	5.37	4.07	86.6	83.4	61.4	80.5	54%	55%
7.25	4.41	4.46	57.1	42.7	44.3	46.1	65%	64%

4.3. Wrist to Footwear Channel Characterisation

The S_{21} parameter was measured using a Rohde & Schwarz ZVA 24 for a standing and walking subject. The measurements were made in a room 8.1 m x 7.9 m with furniture and reinforced concrete walls and floors. The subject walked along one side of the room as shown in Fig. 4.7.

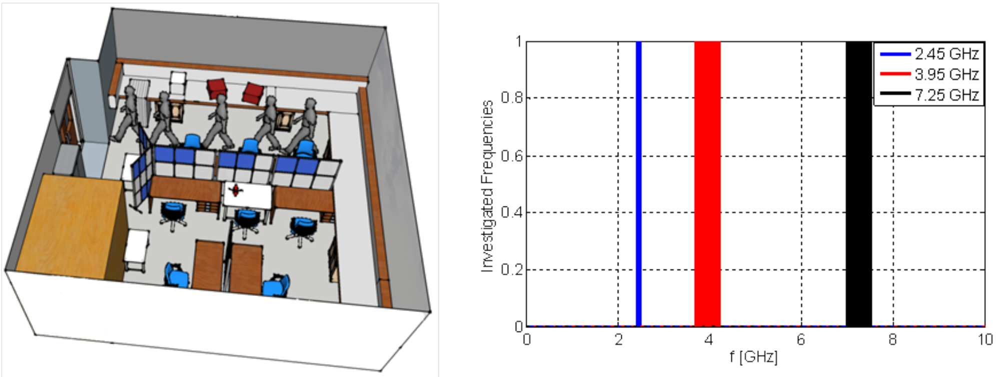

Figure 4.7. Layout of the room and investigated frequency bands.

The first antenna is located on the right-side toe-cap and the second antenna is located above the right wrist, as shown in Fig. 4.8. Three different frequency bands are analysed as shown in Fig. 4.7: a 50 MHz channel centred at 2.45 GHz, a 500 MHz channel centred at 3.95 GHz and a 500 MHz

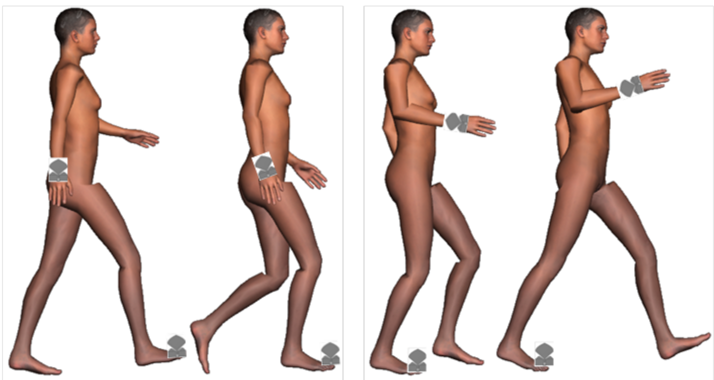

Figure 4.8. Walking subject with antennas on wrist and toe-cap footwear.

band centred at 7.25 GHz. The three frequencies represent the centre frequencies for the narrowband and UWB physical layer for wireless BAN networks in IEEE 802.15.6. In total 5 measurements were made with 330 frequency sweep samples for a walking and standing subject of mass 70 kg and height 1.75 m. The first 10 seconds relate to a stationary subject at one side of the room. Then the subject walks to the other side of the room. Finally the person stands still at the other side of the room. The measurement were repeated every 100 ms. The total time for each measurement was 33 seconds. Path loss results are displayed in terms of Cumulative Distribution Function (CDF) and compared with the Rician distribution using the Maximum Likelihood Estimation (MLE) criteria. To plot the CDF of the measurements, the data are collected in a vector and plotted with the $CDFplot$ function of Matlab. The function automatically displays the empirical cumulative distribution function of the input data. Considering the absolute value of the measured S_{21}, path loss values are obtained.

4.3.1. Narrowband Channel - 2.45 GHz

In this paragraph the results for the 2.45 GHz narrowband channel is investigated. The link channel measured in the five sets of measurements as a function of time is shown in Fig. 4.9. For the first 10 s, the variation in the channel is small (between -59 dB and -50 dB). When the subject starts walking the S_{21} oscillation increases, but remaining between -67.8 dB and -48 dB. Finally the subject is standing in front of a wall, and the S_{21} parameter is almost constant for each set of measurements.

The CDF of the 5 measurements is shown in Fig. 4.9. The minimum and the maximum values of the 5 measurements are summarized in Table 4.3. Considering all the measurements, the maximum range is equal to 19 dB. The CDF is compared with the MLE for the corresponding Rician Distribution, assuming that there is a dominant path between the foot and the wrist.

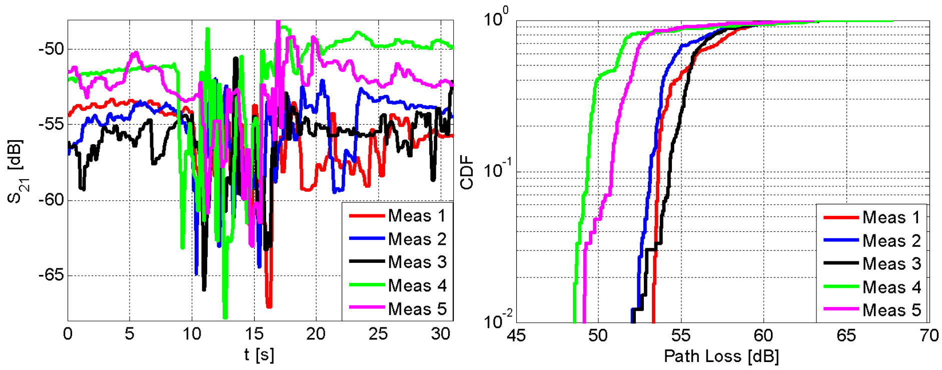

Figure 4.9. Measured S_{21} (dB) for a subject walking and path loss CDF (dB) for the 5 cases at 2.45 GHz.

Inspection of the CDF plots make evident that the path loss of 90% of the measurements is smaller than 59 dB and the path loss of 50% of the measurements is less than 55 dB.

The Rician distribution K-factor is summarized in Table 4.3. The measurements are characterized by a K-factor always greater than 7.5 dB, evidencing the presence of a dominant component of the received signal which is greater than the scattered components. The range of K-factors spans from 7.5 dB to 10.5 dB. The path loss is always smaller than 67 dB.

Looking at the curves of Fig. 4.9, it is clear that the effect of the body movement has a greater effect on the channel performance compared to multipath effects due to the body position in the room. However the multipath effects are greater in the starting position compared to the final position.

Table 4.3. Minimum path loss, maximum path loss and K-factor estimation for the different measurements for the 2.45 GHz channel.

	Minimum path loss [dB]	Maximum path loss [dB]	K-factor [dB]
Meas 1	53	67	9.16
Meas 2	52	65	9.97
Meas 3	50	66	10.5
Meas 4	48	67	7.5
Meas 5	48	63	9.7

4.3.2. Lower UWB Channel 3.95 GHz

In this section the results of the lower UWB channel are shown. The investigated centre frequency is 3.95 GHz with 500 MHz bandwidth. The S_{21} measurements of a walking subject as a function of the time, is shown in Fig. 4.10. The S_{21} parameter is almost constant for the stationary subject at the starting point and in front of the wall. When the subject is walking the S_{21} parameter oscillates with a greater range of values, with peaks of maximum S_{21} equal to -51.89 dB and minima of -57.23 dB. The CDF of the 5 measurements is shown in Fig. 4.10.

The CDF distributions are quite similar to each other. Table 4.4 summarizes the minimum and maximum values and the K-factor for the corresponding Rician distribution. The K-factor for the 3.95 GHz frequency range is always greater than 16.2, corresponding to a more directive link between the footwear and the wrist in comparison to the 2.45 GHz case. This is also due to a greater realized gain of the antenna compared to the 2.45 GHz case (See Fig. 4.5 & Fig. 4.6).

The increased bandwidth decreases the fading, reducing the minimum path loss range to 4 dB. The greater K-factor compared to the narrowband channel can also be explained by the smaller antenna beamwidth, reducing

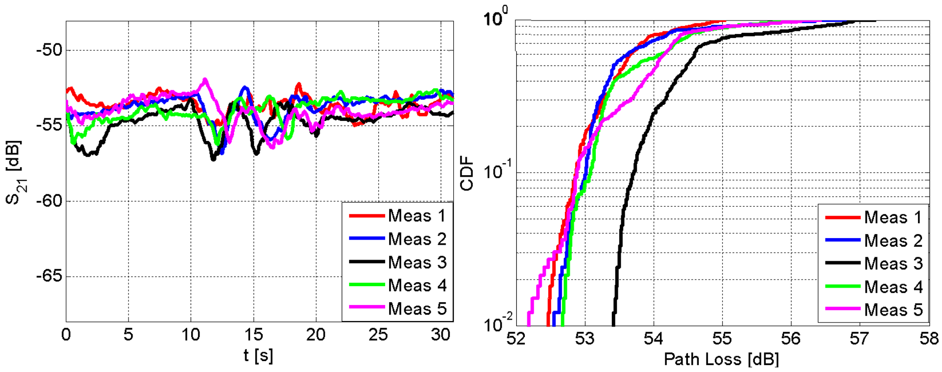

Figure 4.10. Measured S_{21} (dB) for a subject walking and path loss CDF (dB) for the 5 cases at 3.95 GHz.

Table 4.4. Minimum path loss, maximum path loss and K-factor estimation for the different measurements for the 3.95 GHz channel.

	Minimum path loss [dB]	Maximum path loss [dB]	K-factor [dB]
Meas 1	52	52	20.5
Meas 2	53	57	18.0
Meas 3	53	57	16.2
Meas 4	55	56	17.2
Meas 5	52	57	17.3

the reflected signals from the surrounding environment.

4.3.3. Upper UWB Channel 7.25 GHz

The performance for the upper UWB band was investigated. The centre frequency is 7.25 GHz with a 500 MHz bandwidth. In Fig. 4.11 the measured S_{21} for the walking subject as a function of time is shown. As observed for previous cases, the S_{21} parameter is almost constant for the first 10 seconds, with an S_{21} value equal to $\sim$ -53.5 dB. When the subject is walking, the S_{21} range remains between -54.2 dB and -51.6 dB. Finally when the subject is standing at the end of the room the S_{21} parameter is almost constant and equal to -53.8 dB. The CDFs of the 5 measurements are shown in Fig. 4.11.

In this case the measurements are much closer to each other. The measured path loss values and K-factors are summarized in Table 4.5.

Table 4.5. Minimum path loss, maximum path loss and K-factor estimation for the different measurements for the 7.25 GHz channel.

	Minimum path loss [dB]	Maximum path loss [dB]	K-factor [dB]
Meas 1	52	54	20.9
Meas 2	52	54	23.7
Meas 3	52	54	26.0
Meas 4	52	54	24.9
Meas 5	52	54	23.3

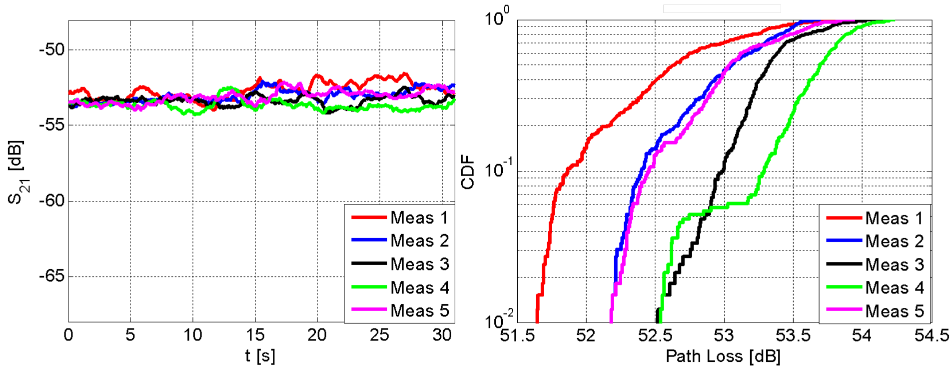

Figure 4.11. Measured S_{21} (dB) for a subject walking and path loss CDF (dB) for the 5 cases at 7.25 GHz.

The K-factor is greater than the previous case and always greater than 20.9 dB. The difference between the maximum and the minimum K-factor is equal to 5.1 dB. As expected, the K-factor is greater than the previous cases. Although the maximum realized gain is less than the 3.95 GHz case, the beamwidth of the antenna is smaller, resulting in a decreased signal scattering in the surrounding environment. The minimum path loss values are similar to 3.95 GHz because of the greater realized gain for the footwear antenna.

4.4. Conclusions

In this chapter a wideband monopole antenna is optimized to operate in close proximity of different areas of the body for on-body communications. The antenna is -10 dB on-body matched within 2.4 GHz and 10 GHz and it has been fully characterized in terms of radiation patterns. The S_{21} link between the wrist and footwear toe-cap is reported for a subject standing and walking considering a communication link between the right wrist and foot for different frequency bands and different bandwidths. The different measurements performed are reliable and witness the good capability of the antenna. The obtained fading values are greater for the narrowband channel, due to the greater beamwidth of the antenna. The MLE criteria is used to compare the CDF distributions of the measured loss with Rician channel models. All the measurements were characterized by a high K-factor due the LOS link between the footwear and the wrist. The measured K values increases with the increment of the frequency band, due to a reduction of the -3 dB beamwidth of the antenna and to the increment of the directivity with the frequency for the antenna on both locations. The communication link complies with the standard for each of the measured cases for a subject standing and walking. Further work will consider the receiving node in different body locations; hence it will establish the optimum frequency band for different body locations. The antenna will be tested in an outdoor environment and with different transceivers to mitigate cable effects.

5. 433 MHz Insole Antenna

5.1. Introduction

In Section 4 the propagation channel between a footwear-mounted antenna and an on-body link is investigated at 2.4 GHz and for the UWB frequencies. In this chapter a 433 MHz dipole-type antenna is designed to be embedded below the insole of the shoe and the low frequency channel between the footwear and on-body links is investigated. The 433 MHz Industrial Scientific Medical (ISM) frequency is less prone to body shadowing effects because of the longer wavelength and less prone to interference from other devices [103]. This band improves the link quality with sensor nodes located on various areas of the body and the shoe is suitable to embed the antenna due to the available volume. There are issues to be considered in designing a 433 MHz antenna in the shoe. The antenna-to-foot distance is electrically very small at this frequency. The antenna, which is in close proximity to lossy and high dielectric foot tissues, must be matched and also radiate from the sides, retaining as much efficiency as possible. Also the presence of the ground below the antenna must be taken into account because of the proximity to high conductivity and dielectric materials of many floors. The floor/ground electrical properties display a wide range of relative permittivity and conductivity values. The antenna should operate regardless of the ground type and proximity. Normally the outdoor ground scenario has a relative permittivity value between 5 and 100 and a conductivity value between 10^{-4} and 1 S/m [67]. Various on-body devices already operate in this band, such as antennas embedded in a belt for medical RF applications [104], intra oral wireless devices [105], biotelemetry for implanted devices [106] and small 433 MHz antennas for sensing telemetry [107].

Lightweight miniaturized devices have a low impact on natural gait and the rigidity in footwear, and compared with other types of clothing, can support larger components. In proximity to the human body, the long wavelength related to the 433 MHz frequency has an improved propagation range, resilience to variations of posture, physiology and ground surface conductivity and has lower spectrum congestion. It has been demonstrated that low UHF on-body communication links can be characterized by a path loss distribution independent of distance [108]. An integrated solution for a 433 MHz antenna located between the footwear sole and insole is proposed for a coordinating hub in a Body Area Sensor Network. Printed on single-sided 0.2 mm FR4, the radiation pattern emerges from the lateral edges to minimize radiation loss in the foot. In order to assess the matched impedance for different ground conductivity conditions and the propagation link performance with upper body areas, modeling is validated using indoor measurements of subjects in static and dynamic postures. The study also reports the specific absorption rate.

5.2. Antenna Design

The antenna footprint must be smaller than the insole surface avoiding discomfort or distraction to the user, which for this case was 275 mm long and varied from 60 mm to 90 mm wide. The antenna is prototyped on 0.2 mm single-sided FR4 which is flexible and can easily be located beneath the insole or embedded in the shoe. The insole and the external sole were 2 mm thick and 25 mm thick, respectively. The antenna can be manufactured on more robust and flexible substrates where necessary. CST Microwave Studio was used to simulate the electromagnetic environment. The hetero-

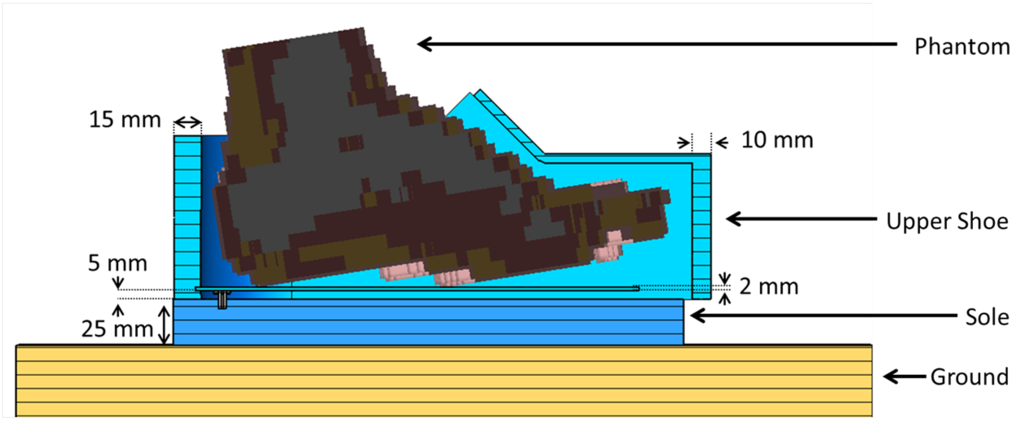

Figure 5.1. CST model of antenna under heterogenous voxel foot in shoe over reinforced concrete ground

geneous anatomical foot and shoe model used in the simulation is shown in Fig. 5.1, with material properties listed in Table 5.1 [73].

The shoe-embedded antenna with the insole removed is shown in Fig. 5.2. It was inserted through a horizontal slot between the heel and the upper area and the connector was accommodated with a cavity in the sole. A 0.2 mm thick single sided FR4 substrate is used for the antenna, shown in Fig. 3.

The antenna uses an unbalanced feed but is essentially a dipole-like antenna. The radiating element is a long rectangular loop and surrounded by a modified ground plane at the edges as well as inside the loop. This con-

Table 5.1. Electrical properties of body shoe material and ground.

	ϵ'	σ	$\tan\delta$
Muscle	56.88	0.80	-
Skin	46.10	0.70	-
Fat	5.57	0.04	-
Bone	13.10	0.09	-
UpperShoe	1.4	-	0.04
Sole	3	-	0.06
ReinforcedConcrete	6	0.00195	-
PEC	-	∞	-

Figure 5.2. Photographs of the shoe-embedded antenna with the insole removed.

figuration allows radiation from the side elements rather than the centre. The antenna was optimized with the CST Trust Region Framework technique. The optimized geometry for the insole antenna is shown in Fig. 5.3.

The antenna is fed by a CPW using a SMA connector below the dielectric. A CPW impedance transition is required because of the proximity to the

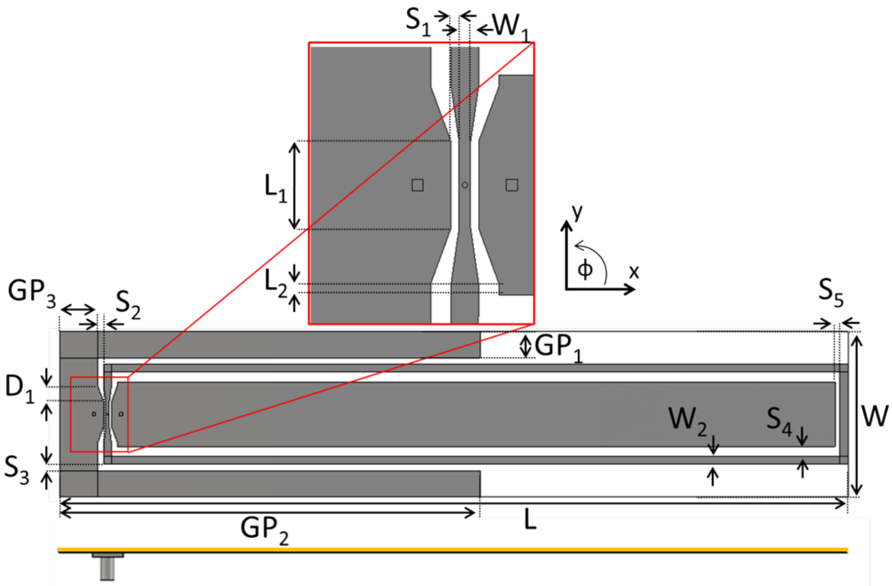

Figure 5.3. Geometry of the optimized insole antenna.

Table 5.2. Dimensional parameters of the antenna.

Parameter	Dimension [mm]	Parameter	Dimension [mm]
W	51	S_5	1.5
L	243.61	GP_1	8
W_1	1.04	GP_2	130
W_2	2.5	GP_3	11.75
S_1	0.73	L_1	7.87
S_2	1.83	L_2	1
S_3	2	D_1	5
S_4	3.12		

connector flange. The different slot widths between the feed line and two grounds increase the coupling to the external ground, keeping the antenna matched. The antenna dimensions are listed in Table 5.2.

The overall dimensions of the optimized antenna are 243 mm x 51 mm. To refine the input impedance, the groundplane length was assessed for 90 mm $< GP_2 <$ 150 mm. The matched impedance bandwidth was varied with S_5 and the longer length L lowered the resonance frequency.

The simulated and measured free-space S_{11} are shown in Fig. 5.4. The antenna is -10 dB matched from 442 to 634 MHz in the simulation. In the measurement this band is shifted down by $\sim$ 20 MHz, covering 433 MHz.

A plot of the current density on the insole antenna is shown in Fig. 5.5.

The antenna is designed to radiate from the edges, where the presence of the foot is limited. The current is mainly distributed on the ground plane outside layers and on the transmission line with lower concentrations at the centre of the ground plane. This is due to the asymmetric groundplane dimensions, S_3 and S_4 which control the coupling with the external ground plane.

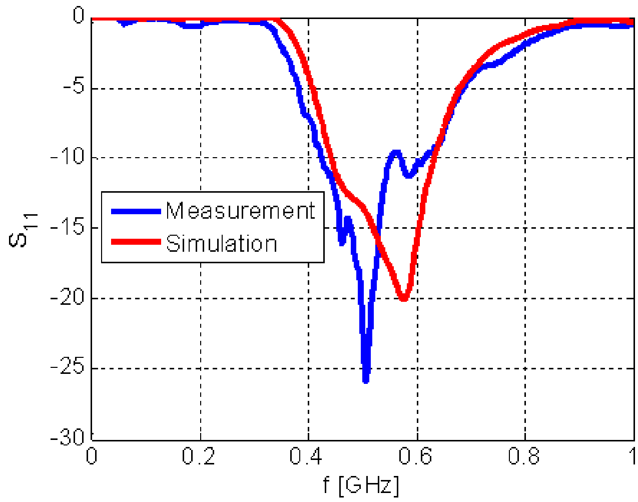

Figure 5.4. Simulated and measured S_{11} (dB) for the antenna in free space.

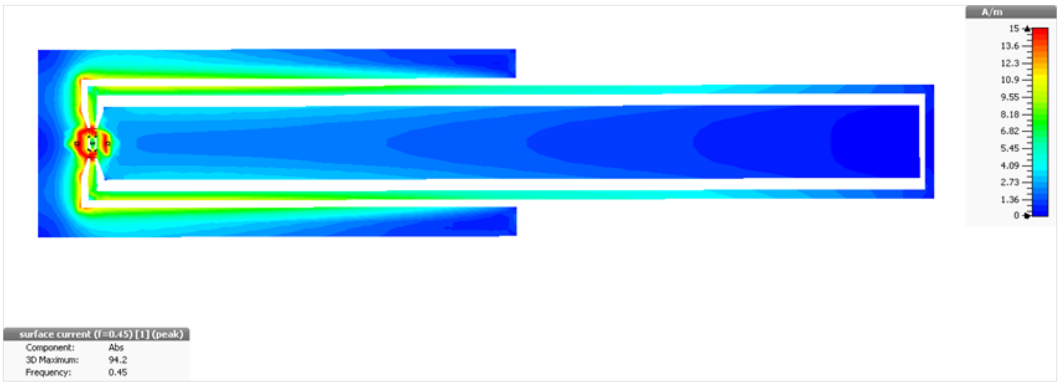

Figure 5.5. Maximum amplitude of the current (A/m) at 450 MHz for free-space antenna.

5.3. Ground and Human Body Performance

The antenna on-body and on-ground performances are investigated. To include different scenarios, three ground conditions are considered, PEC, reinforced concrete (ϵ_R = 6, σ = 0.00195 S/m) [109] and ground-less.

While walking or running, the foot can lift off the surfaces for a "ground-less" condition. Some typical underfoot scenarios are emulated with free

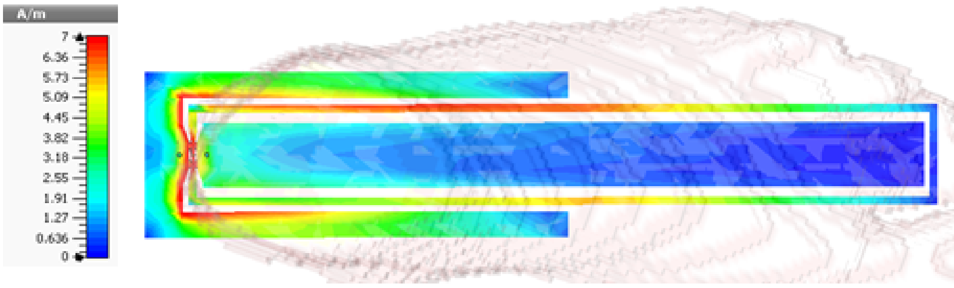

Figure 5.6. Maximum amplitude of the current(A/m) at 433 MHz for body loaded antenna.

space, reinforced concrete [109] and Perfect Electrical Conductor (PEC), where PEC represents high conductivity associated with a running treadmill or bridge structure.

The final simulation models on reinforced concrete ground are shown in Fig. 5.1. The antenna-foot separation is 2 mm due to the typical insole thickness and 20 mm above the ground because of the sole height.

Also when the antenna radiates in close proximity of the body, the current distribution peak is located on the edges of the lateral ground planes, as it is shown in Fig. 5.6.

The simulated and measured S_{11} for various ground types are shown in Fig. 5.7.

The simulation and measurement are in reasonable agreement for all cases. The presence of the reinforced concrete ground doesn't impact the S_{11} parameter compared to the ground-less case for both simulation and measurement. The presence of the PEC ground degrades the S_{11} parameter for some frequencies. In particular there are two bands where the antenna is -10 dB matched. In all cases, the -10 dB impedance bandwidths are shifted downwards compared to free-space. The discrepancies between simulation and measurement are due to different antenna-to-foot separations, differences in the numerical phantom morphology and differences in the electrical properties. However, the measured S_{11} is better than -10 dB

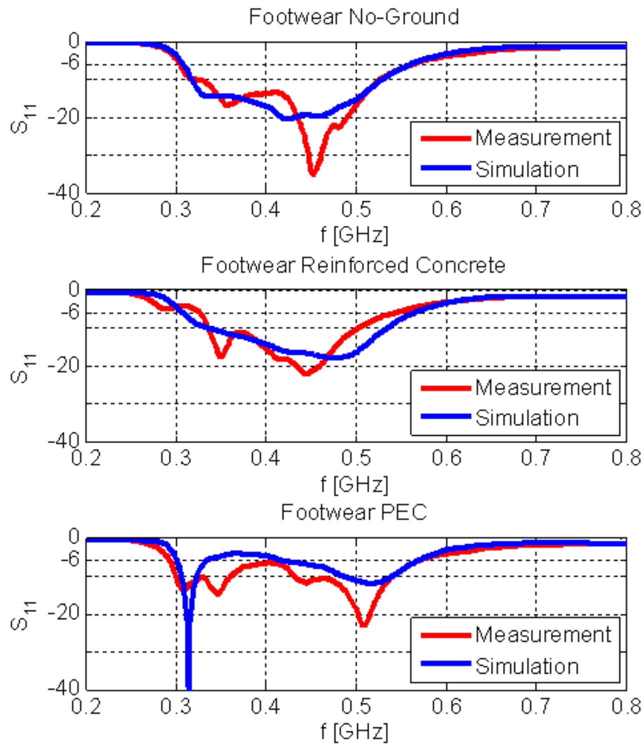

Figure 5.7. Measured and simulated S_{11} (dB) for ground-less (first row), reinforced concrete (second row) and PEC (third row) ground for the on-body antenna.

for the frequency of operation for the different ground types.

The simulated and measured S_{11} values are summarized in Table 5.3 for the ground-less, reinforced concrete and PEC cases, listing the lower (f_{low}) and upper (f_{high}) edge frequency for the -10 dB and -6 dB S_{11} values.

Both simulations and measurements meet the S_{11} (-6 dB) matching bandwidth and the measurements meet the S_{11} (-10 dB) matching bandwidth. The -10 dB measured fractional bandwidth for the footwear no ground case is 48%. When the ground is added, the bandwidth decreases to 39% for the reinforced concrete case and to 22% for the PEC case. The PEC ground degrades the S_{11} for the -10 dB matched mid-band. This shows that the antenna performances are more limited when the antenna is located over

Table 5.3. Comparison of the lower and upper frequency for the -10 and -6 dB bandwidth for the On-body simulated and measured S_{11} for different ground types.

		Simulated		Measured	
		f_{low}	f_{high}	f_{low}	f_{high}
Ground-less	-10 dB	318	528	322	526
	-6 dB	308	560	306	564
Reinforced Concrete	-10 dB	336	534	336	500
	- 6 dB	306	564	328	540
PEC	-10 dB	306	324	300	360
	-10 dB	486	540	432	540
	- 6 dB	302	568	294	568

PEC. The on-body simulations for the ground-less case and the reinforced concrete case are in good agreement with the measured reflection coefficient. However the agreement of the antenna close to a PEC material is acceptable, although better results can be further researched. For the purpose of the paper, the measured values demonstrated the antenna resilience to different ground types.

5.4. On-Body Communications Link

In this section the antenna on-body performance in an indoor environment is investigated. The insole antenna performance is using S_{21} measurements between the insole antenna and a small 433 MHz antenna. The communications link from the shoe-embedded hub antenna to several body area nodes is considered. The influence of the body movement on the link performance is evaluated for a walking subject.

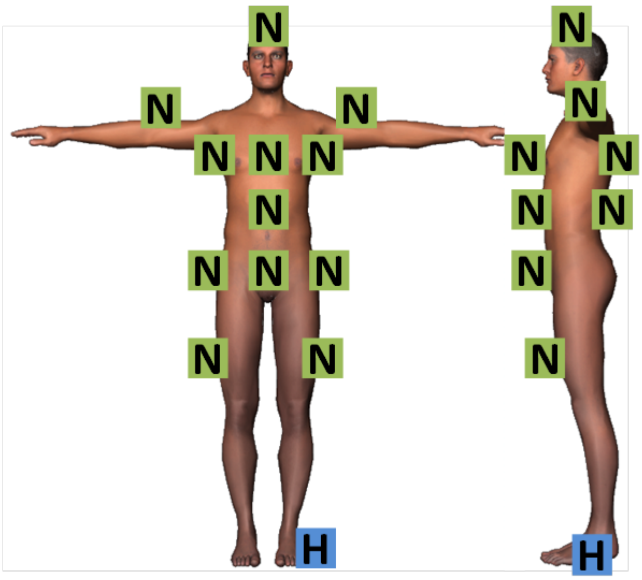

Figure 5.8. Positions of the hub and the different nodes.

5.4.1. Measurement Setup

In total, there is one footwear-located hub and 14 nodes deployed around the body as follows: front of head, upper arm (left and right), upper chest (left, right, front and rear), chest, lumbar spine, waist (left, right and front) and upper leg (left and right) as shown in Fig. 5.8.

These positions correspond to potential positions of on-body sensors and cover the whole body surface. The measurements are performed for a stationary subject with the arms alongside the hips.

5.4.2. On-Body 433 MHz Antenna for Nodes

A small 433 MHz Inverted-F antenna is designed for the on-body node as shown in Fig. 5.9. The antenna ground is placed on the body surface, to ensure a perpendicular polarization.

The antenna geometry is shown in the Fig. 5.10. The antenna substrate

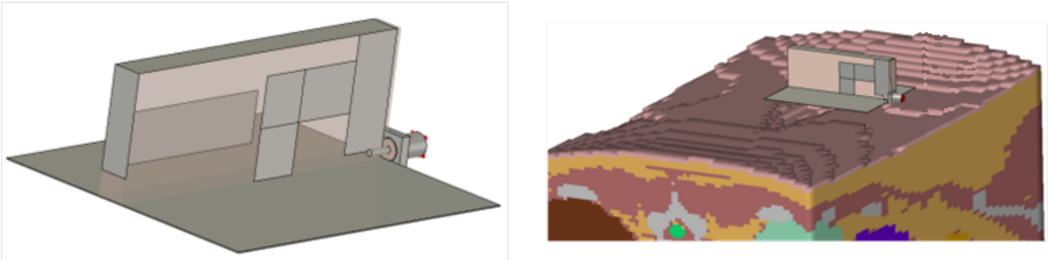

Figure 5.9. Geometry of the 433 MHz node antenna and antenna located on the front of the waist .

is Taconic RF-35 (ϵ_R=3.5, $tan(\delta) = 0.0018$) with a thickness of 6.2 mm. The antenna ground plane is 0.2 mm FR4 allowing conformal deployment on the body surface. The antenna overall dimensions (excluding the ground plane) are 70 mm x 25 mm. To provide adequate electric length at 433 MHz, the conducting strip is fed at the side, then wrapped across the top substrate edge to the side edge and finally across to the opposite side as shown in Fig. 5.10. The thick substrate (6.2 mm) is used to keep a wide width of the antenna strip.

A short circuit between the feed line and the ground is used to match the impedance at the chosen frequency. The antenna dimensions are optimized when located on the front waist of the Gustav voxel model.

The antenna is smaller than $\lambda_0/9$ at 433 MHz. The measured on-body S_{11} for different node locations is shown in Fig. 5.11 and then summarized in Table 5.4.

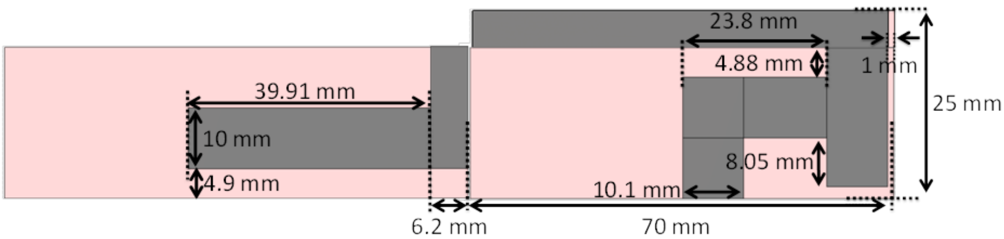

Figure 5.10. Geometry of the extended 433 MHz node antenna.

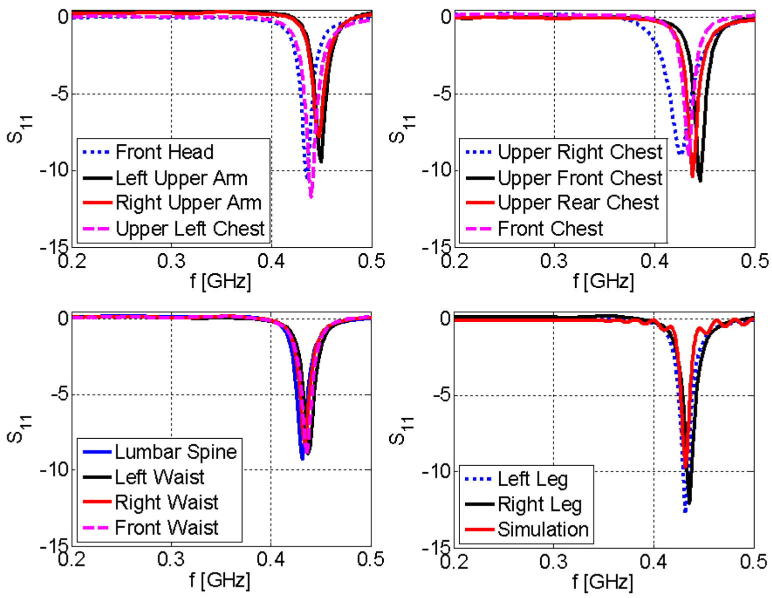

Figure 5.11. Measured S_{11} (dB) for the 433 MHz node antenna for different on-body locations.

Table 5.4. Resonant frequency and S_{11} value for the small 433 MHz antenna for different on-body locations.

	f_{min} [MHz]	S_{11} value [dB]
Front Head	436	-10.63
Left Upper Arm	450	-9.40
Right Upper Arm	448	-7.79
Upper Left Chest	440	-11.72
Upper Right Chest	426	-9.01
Upper Rear Chest	446	-10.68
Upper Back Chest	438	-10.35
Front Chest	434	-8.94
Lumbar Spine	432	-9.26
Left Waist	438	-8.91
Right Waist	434	-8.26
Front Waist	436	-9.03
Left Leg	432	-12.75
Right Leg	436	-12.06
Simulation on the front waist	432	-9.67

The S_{11} minima are always between 426 MHz and 450 MHz, with the measured S_{11} always better than -7.8 dB. The radiation pattern shape is reasonably omnidirectional when the antenna is located on the body with a simulated maximum realized gain value of -6 dBi.

5.4.3. On-Body S_{21} Measurements between the Footwear Embedded Antenna and Node Antennas on Various Body Locations

In this section S_{21} measurements are recorded for a communication link between the insole-antenna and node antenna for different body locations as previously described. The measurements were performed on a subject of 1.75 m height with weight of 70 kg in an 8.1 x 7.9 m laboratory area with metallic furniture and a reinforced concrete floor and ceiling. The results are shown in Fig. 5.12.

There is always a peak in the S_{21} parameter in the 433 MHz frequency region and the measured S_{21} results are summarized in Table 5.5. The frequency for the S_{21} peak shows some dependence on the on-body node antenna resonant frequency, due to variations in body coupling. The S_{21} value is also a function of the distance between the insole antenna and the node, with better values for closer locations such as the left leg. The horizontal spread of the measured S_{21} for all the locations is 16.9 dB.

The lower values of S_{21} are observed for the upper sides of the body (right and left upper arm) and for the upper chest positions. Nevertheless, the insole-embedded antenna efficiently covers all body locations with S_{21} always better than -45.8 dB in the frequency band close to 433 MHz. Although the best S_{21} shows some location dependency, its value at 433 MHz is always better than -46.9 dB.

The average S_{21} is equal to -40.71 dB at 433 MHz, while considering the peak it is -29.55 dB. The difference between the average at 433 MHz and at

Table 5.5. S_{21} Frequency peak and intensity for different on-body locations.

	f_{max} [MHz]	S_{21} value [dB]	S_{21} value [dB] for f = 433 MHz
Front Head	436	-41.57	-42.28
Left Upper Arm	452	-38.03	-46.45
Right Upper Arm	448	-36.61	-43.09
Upper Left Chest	438	-45.57	-46.93
Upper Right Chest	426	-45.83	-46.40
Upper Front Chest	440	-42.10	-44.17
Upper Rear Chest	438	-40.35	-40.78
Front Chest	432	-32.55	-32.60
Lumbar Spine	428	-44.47	-44.90
Left Waist	436	-38.26	-38.46
Right Waist	438	-40.92	-42.53
Front Waist	430	-35.86	-36.41
Left Leg	430	-29.55	-30.04
Right Leg	430	-34.00	-34.90

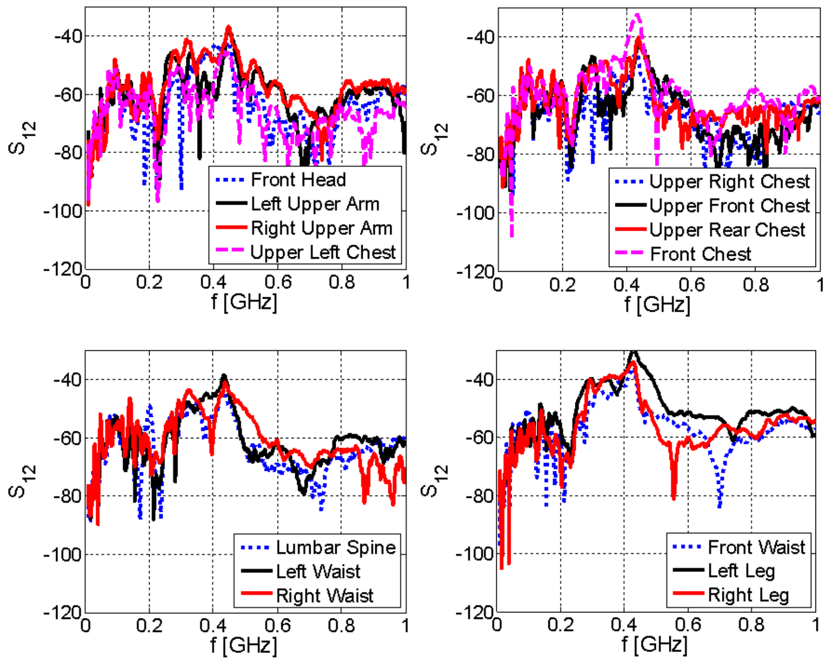

Figure 5.12. Measured S_{21} (dB) between insole-embedded antenna and the node antennas on various body locations.

the peak value is 10 dB. These measurements took into account different aspects, such as:

- the different composition of the human body that is different for different node locations;
- the distance between the footwear hub and the node, that varies from 60 cm to 1.7 m;
- shadowing and fading, considering the multipath scenario.

5.5. Evaluation of Specific Absorption Rate

The evaluation of Specific Absorption Rate (SAR) is important to quantify the health hazard due to absorption of electromagnetic energy into the body. The international standards and guidelines for exposure of personnel to electromagnetic energy in Europe [78] and United States [79] limit the local peak SAR to 4 W/Kg averaged over 10 g of tissue for the limbs.

The greater value of the SAR limit in the limbs compared to the other body locations is due to different tissue compositions because the limbs are not characterized by vital organs.

The SAR is calculated here using the numerical anatomical voxel foot on a reinforced concrete ground, on PEC as well as for the ground-less condition. The input power is 1 W. The SAR distribution for different ground conditions is shown in Fig. 5.13 the side and bottom view of the foot are represented. The SAR values are summarized in Table 5.6.

Table 5.6. 433 MHz Simulated SAR.

	10 g [W/KG]
Ground-less	2.55
Reinforced Concrete	2.08
PEC	1.87

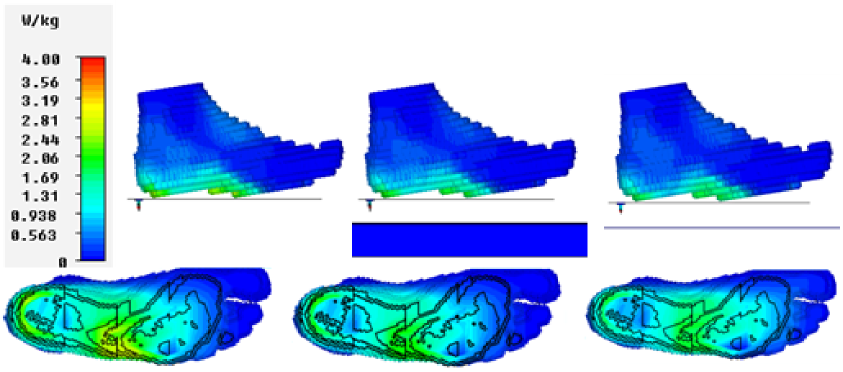

Figure 5.13. SAR for ground-less, reinforced concrete and PEC ground.

The local peak SAR value was found to be 2.55 W/kg at the lateral quarter area of the foot for the ground-less case as shown in Fig. 5.13.

In general, the SAR is greater where the lateral quarter area of the foot is closer to the radiating element and feed point. The SAR maximum peak position and distribution along the foot surface does not change for the different grounds. The lower value of SAR in the presence of the ground is due to a greater power absorption in the shoe sole. In general the presence of the ground decreases the SAR due to a greater dissipation of the electric field in the shoe materials. These calculated SAR values fully comply with the US and ICNIRP limits and guidelines for an input power of 1 W, regardless of the type of ground considered.

5.6. Antenna Performance for a Walking Subject

The link between the footwear-embedded antenna and the left waist is reported for a walking subject. Each link measurement is performed on a subject of 1.75 m height with weight of 70 kg in a 8.1 x 7.9 m laboratory area with metallic furniture and a reinforced concrete floor and ceiling, as shown in Fig. 5.14. S_{21} values are recorded at 433 MHz. The link measurements are recorded in a static channel considering the subject repeatedly

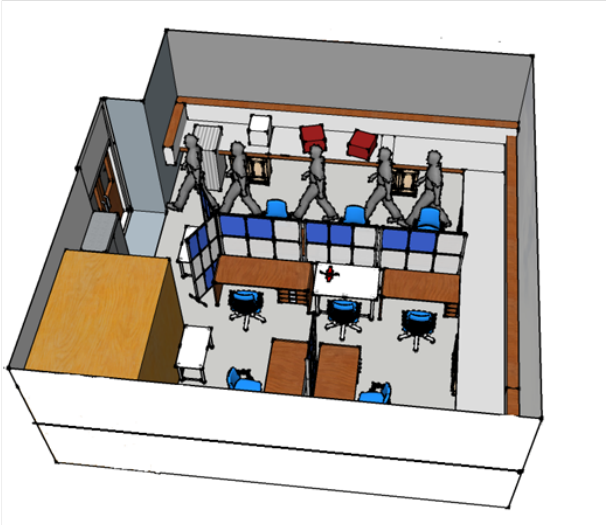

Figure 5.14. Measurement environment.

walking from one side of the room to the other over a total time of 60 seconds. The subject changes direction every $\sim$ 5s, turning in the opposite direction and returning to the starting point.

One measurement sample is recorded every 0.1 s, with 640 link measurements in total. A series of 5 measurements are made with the same measurement setup, same subject and the same environment. The recorded S_{21} values as a function of the time for one measurement are shown in Fig. 5.15.

There is no significant change in the S_{21} parameter when the subject changes walking direction. The rapid change of the S_{21} parameter is due to the shadowing of the arm and the multipath effects in the indoor environment. The cumulative distribution function (CDF) of the 5 series of measurement are shown in Fig. 5.15 . Inspection of the CDF data indicates that 90% of the observed cases are characterized by an S_{21} greater than -35 dB. Considering all measurements, the horizontal spread is slightly greater than 44 dB. These results demonstrate the antenna resilience to body movement in an indoor environment. Based on the S_{21} measurements, a reliable

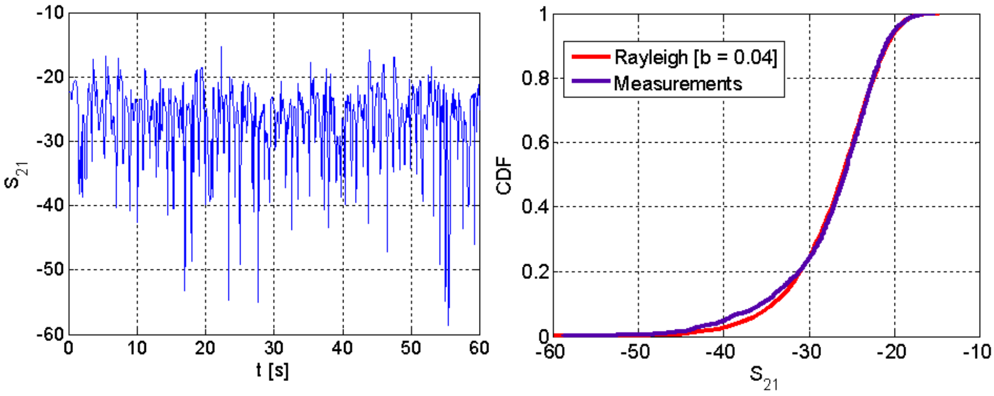

Figure 5.15. Measured S_{21} (dB) for walking subject and CDF for walking subject with the receiving antenna on the left waist.

communication link is always possible within the WBAN standard [10]. The cumulative distribution function (CDF) of the 5 series of measurement are shown in Fig. 5.15 . Inspection of the CDF data indicates that 90% of the observed cases are characterized by an S_{21} greater than -35 dB. Considering all measurements, the horizontal spread is slightly greater than 44 dB. These results demonstrate the antenna resilience to body movement in an indoor environment. Based on the S_{21} measurements, a reliable communication link is always possible within the WBAN standard [10].

It should also be noted that the antenna alignments change with body movements, however, a reliable communication link is maintained [10]. The distribution of the path loss of each set of measurement is compared with

Table 5.7. S_{21} peak value and frequency for different on body locations.

Measurement		1	2	3	4	5
Rician	K [dB]	-1.0	-20.0	0.56	-24.0	-2.0
Nakagami	μ	1.03	0.9	1.13	0.76	1.01
	σ	0.005	0.003	0.003	0.004	0.004
Rayleigh	b	0.05	0.04	0.04	0.04	0.04

the Rician, Nakagami and Rayleigh distribution using the maximum likelihood criteria. The information about the distribution parameters are summarized in Table 5.7. The Nakagami μ parameter and the Rician k factor indicate a high multipath environment. The low value of σ in the Nakagami distribution indicates a small spread for each set of measurements. The Rayleigh distribution fits well all the measurements with a constant scaling factor. The cumulative distribution function CDF of the 5 sets of measurements is represented in Fig. 5.15.

5.7. Conclusions

In this chapter an insole integrated antenna is designed for BAN applications. The antenna is the first 433 MHz antenna embedded in footwear, is lightweight, low-cost and the user is oblivious to the presence of the antenna. It doesn't impact on the gait of a walking or running subject and still provides high user comfort. The antenna radiation mechanism is optimised for the close proximity of the foot and ground. It can be used to relay footwear sensor signals to hubs located on the body or to collect data from different body sensors. The antenna is tested for different ground types, demonstrating that a good impedance match can be achieved for different environments. A second 433 MHz antenna was designed and used to probe the footwear antenna performances, demonstrating good coupling for transceivers located at various on-body areas. The communication link is tested for a standing subject for 14 different locations. In all cases, a reliable link was achieved with S_{21} values always better than -46.9 dB. The body movements are investigated by S_{21} measurements with the receive antenna on the left waist for a walking subject in a realistic office scenario, demonstrating good resilience to the different body postures during normal gait. The measured S_{21} is always greater than -58.7 dB and 90% of the cases are greater than -35 dB. This investigation demonstrates the resilience to body movement and guarantees a quality link with sensors deployed on all body locations.

6. UWB Antennas for Footwear

6.1. Introduction

In Section 4 it has been demonstrated that a UWB link is reliable for communication between the footwear and on-body nodes. In this chapter UWB antennas are designed and compared for footwear wireless sensor telemetry for different UWB positions. UWB technology is suitable for BAN because of the greater data rate, the lower power and small communication range [110]. The European UWB includes a lower and an upper range equal to 3.1-4.8 GHz and 6-8.5 GHz. In this section the antenna investigation is limited to the 6-8.5 GHz range. The antennas have to be low profile and easily integrated on the shoe surface. The antennas are chosen to illuminate the upper region of the body for reliable on-body communications. As it has been observed in the previous chapters, the antenna design should take in account the proximity of the body and of the ground. A physical UWB phantom that resembles the foot shape has been realized and used for the measurements. Frequency and time-domain performances for two antenna types are investigated when located on three footwear locations.

6.2. Shoe and Foot Model

A numerical 3-D shoe model was derived using orthographic perspective photographs with the Blender [76] software application to construct a 3D model for import into CST Microwave Studio, shown in Fig. 6.1.

A foot-shaped homogeneous tissue-equivalent phantom was manufac-

Figure 6.1. Photograph of the footwear, blender model and CST imported model.

tured. The materials listed in Table 6.1 [111] were mixed with the prescribed volumes and were formed in a foot-shaped mould. The formula provides a 2/3rd muscle relative permittivity. Dielectric probe measurements of the phantom material were then used to define the properties of the simulated foot model [64]. Two interconnecting Velcro layers with a mated thickness of 3 mm were used to fix the prototype antennas to the various positions on the shoe.

The shoe upper layer comprises fabric and leather materials, for which the relative permittivity was measured using a coaxial probe [64] at conceivable mounting positions on the toe-box, lateral quarter and heel counter. Similar dielectric values were recorded and the average was used to define the shoe upper electrical properties. The rubber sole was also measured and the values used in the model are shown in Fig. 6.2.

The physical and the numerical model with the 3 antenna locations are shown in Fig. 6.3.

Table 6.1. Phantom ingredients.

Material	Quantity [g]
Deionized water	481.3
Agar	14.9
Polyethylene Powder	144.4
Sodium Chloride	1.0
TX-151	4.3
Dehydroacetic Acid Sodium Salt	0.3
Total	646.2

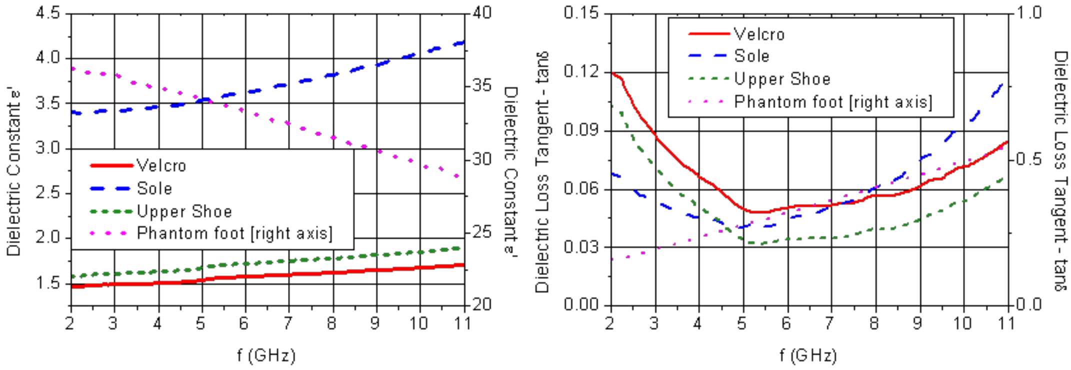

Figure 6.2. Measured dielectric properties of the shoe and phantom foot.

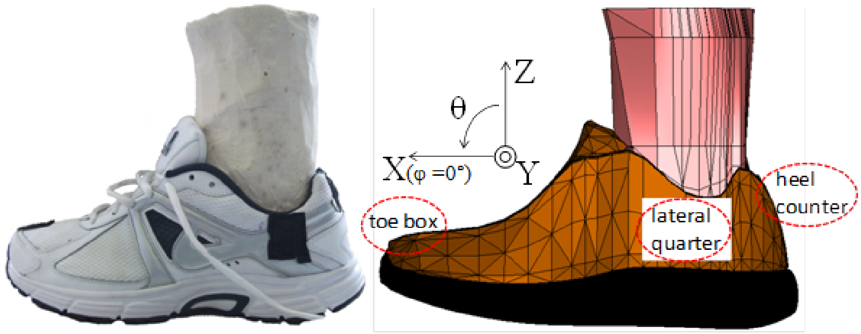

Figure 6.3. Photograph and CST model of the dielectric-loaded shoe.

6.3. Antenna Designs

6.3.1. Monopole Antenna

The monopole antenna is designed on a single-sided FR-4 dielectric with 0.2 mm thickness shown in Fig. 6.4. A coplanar waveguide feed is used to connect the SMA connector to the antenna input.

The geometric parameters were optimized [112] for the footwear with a multi-objective algorithm for a quasi-omnidirectional pattern with impedance matching in the 6-8.5 GHz band [113]. The final dimensions were W = 15.7 mm, L = 25.63 mm, W_f = 1 mm, S_f = 0.56 mm, L_g = 2.4 mm, H_g = 3.6 mm, L_{a1} = 6.17 mm, L_{a2} = 2.96 mm, L_{a3} = 2 mm, D = 1.47 mm,

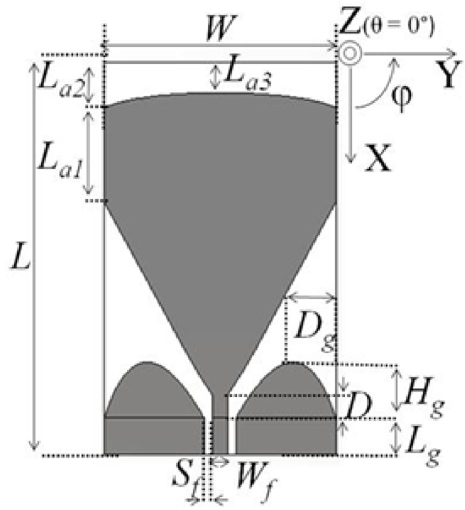

Figure 6.4. Monopole antenna.

D_g = 3.2 mm. The simulated and measured free-space S_{11} are shown to be in good agreement in Fig. 6.5.

Small discrepancies at the low frequency are due to the small ground plane size. The frequency shift in the measured reflection coefficient com-

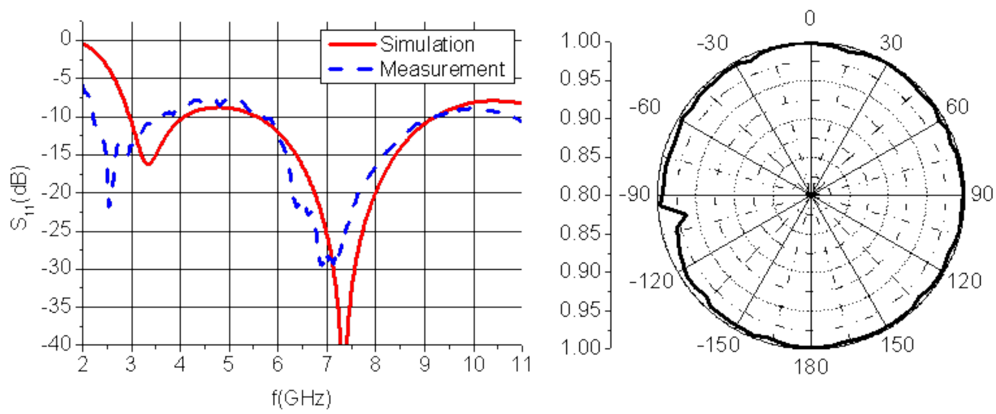

Figure 6.5. Simulated and measured S_{11} (dB) and simulated fidelity factor for ϕ = 0° for the optimized free-space monopole antenna.

pared to the simulated one is due to the cable. However the purpose of the chapter is to investigate the antenna between 6 and 8.5 GHz, so discrepancies at low frequencies are not considered. The time-domain performance of the free-space antenna are evaluated using a 500 MHz Root Raised Cosine (RRC) signal centred at 7.25 GHz with 73 probes surrounding the antenna (angular step = 5°). The spectrum of the RRC is able to fit more efficiently to the UWB mask defined in the standard thanks to the bell-like shape [69] compared to the several derivatives of the Gaussian pulse. The human body sagittal plane for the monopole antenna is selected for the Fidelity Factor (FF) simulation.

The free-space FF is always greater than 0.96 for the monopole antenna with a mean value equal to 0.994. In the free space, the antenna did not influence the impulse shape for any investigated direction.

6.3.2. Vivaldi Antenna

A Vivaldi antenna, shown in Fig. 6.6 is designed on a single-sided FR-4 dielectric with 0.2 mm thickness for operation in the 6-8.5 GHz bandwidth.

A coplanar waveguide feed is matched to a 50 Ω SMA connector. One edge of the CPW forms a slot line T-junction that works as a power divider, where one side is an open circuit and the other is the Vivaldi slot. Considering this geometry, the antenna was optimized to provide good matching in the selected bandwidth and to maximize the realized gain in the boresight direction, $\theta = 0°$, $\phi = 0°$[112]. The optimized design parameters, shown in Fig. 6.6 are L = 28.6 mm, W = 26.2 mm, W_f = 3.34 mm, S_f = 0.423 mm, W_g = 10.59 mm, L_{g1} = 5.37 mm, L_{g2} = 1 mm, L_v = 18 mm, S_v = 1 mm. The equation to define the flared Vivaldi curve is Equation 6.1.

$$Y = 0.125e^{0.24L_V} \tag{6.1}$$

with

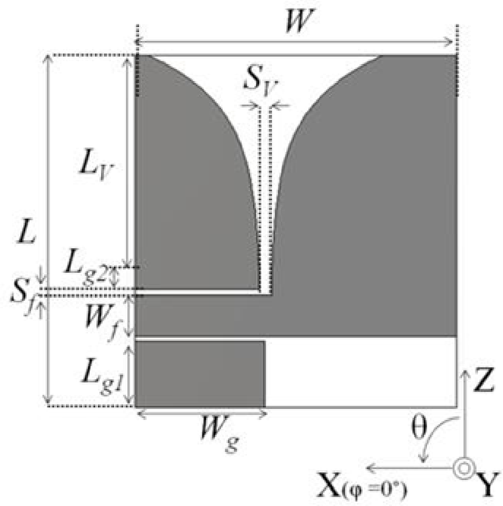

Figure 6.6. Vivaldi antenna.

$$0 < L_V < 18[mm] \tag{6.2}$$

The Vivaldi antenna free-space performance is shown in Fig. 6.7. The antenna was fabricated and measured to have a -15 dB bandwidth for 6-8.5 GHz in simulation, reduced to -14 dB in the measurement. There is a good match between simulations and measurements, so no further numerical analysis is required. The time-domain performance was evaluated using a 500 MHz RRC signal centred at 7.25 GHz with 73 probes surrounding the antenna (angular step = 5°).

The human body sagittal plane for the Vivaldi antenna on the heel counter and the coronal plane for the Vivaldi antenna on the lateral quarter are considered. The free-space FF is always greater than 0.93 with a mean value equal to 0.993. In the free space, the antenna has no influence the impulse shape for the investigated directions.

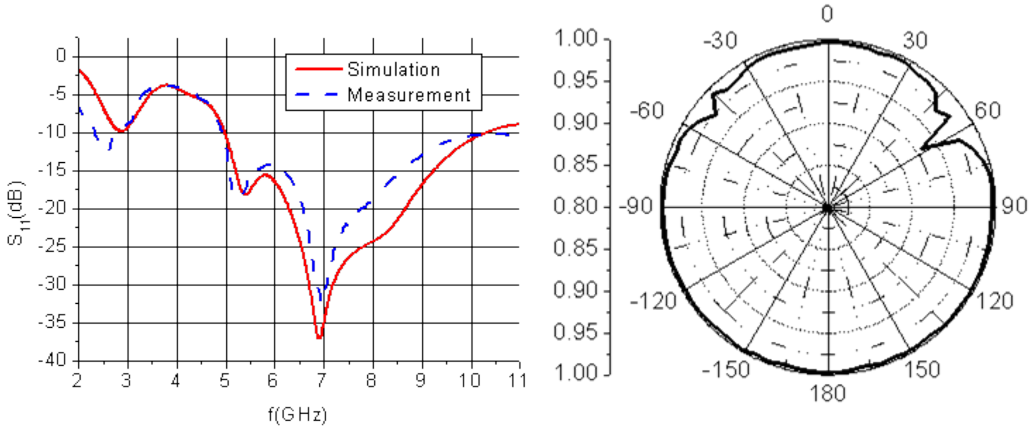

Figure 6.7. S_{11} (dB) and fidelity factor for $\phi = 90°$ for the optimized free-space Vivaldi antenna.

6.4. Frequency Domain On-Body Performance

6.4.1. Monopole Antenna on Toe-Box Loaded with Phantom Foot

The monopole antenna is located on the shoe toe cap, as shown in Fig. 6.8.

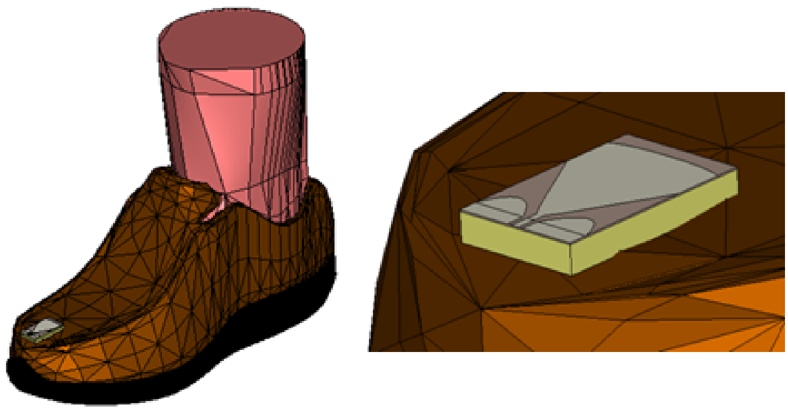

Figure 6.8. Velcro-attached monopole antenna located on the phantom-loaded shoe toe-box.

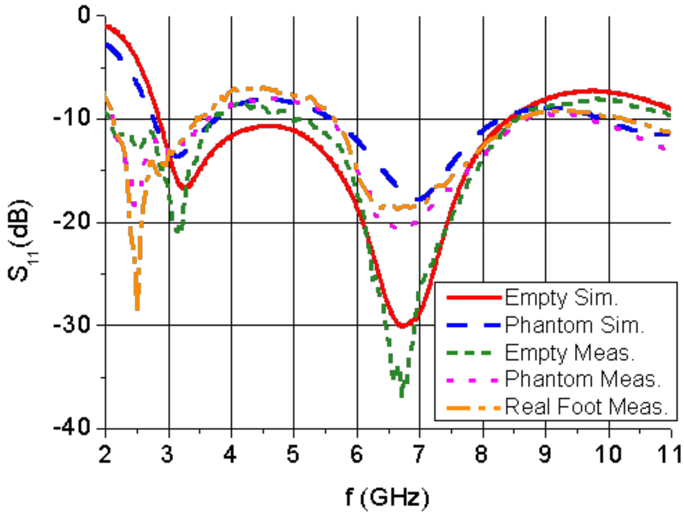

Figure 6.9. S_{11} (dB) simulation-measurement comparison for the monopole antenna located on the toe-box of an empty/phantom/human loaded shoe.

The antenna is attached to the lower edge of the footwear with a layer of velcro. The omnidirectional characteristic exhibited in free space changed predominantly in the back-lobe due to the presence of the human body. This corresponds with an increase in the realized gain in the $\theta = 0°$ direction. While there is an approximate 3 dB drop in the frequency-averaged realized gain for the -180° $< \theta <$ 180° plane compared with the empty shoe case, the average simulated realized gain is greater than 1 dBi for -90° $< \theta <$ 90° for all the UWB frequencies. There is good agreement between the simulation and the measurement.

Fig. 6.9 shows the simulated and measured S_{11} for the phantom loaded shoe. Measurements with a real foot produce similar results to the phantom. The radiation patterns are shown in Fig. 6.10 and in Fig. 6.11.

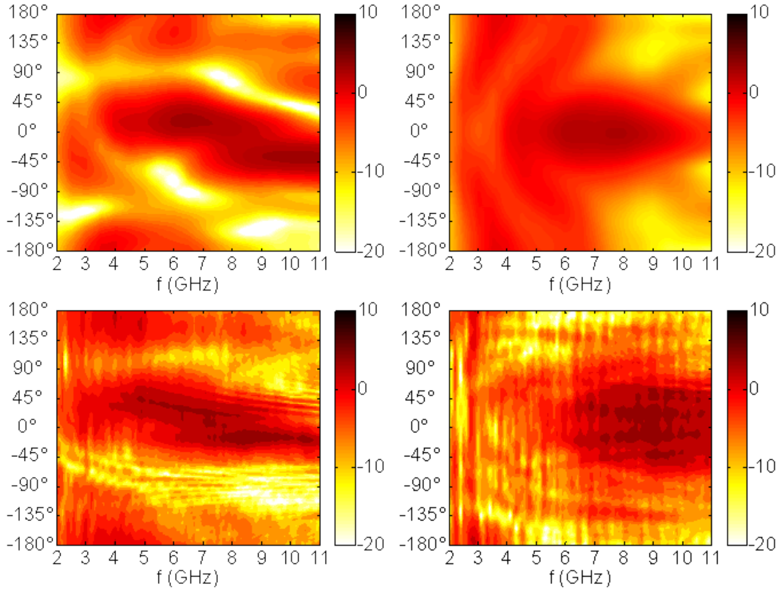

Figure 6.10. 3-D realized gain patterns (dBi) for the monopole antenna on the phantom-loaded shoe toe-box. Simulated (first row) and measured (second row) for $\phi = 0°$ (first column) and $\phi = 90°$ (second column).

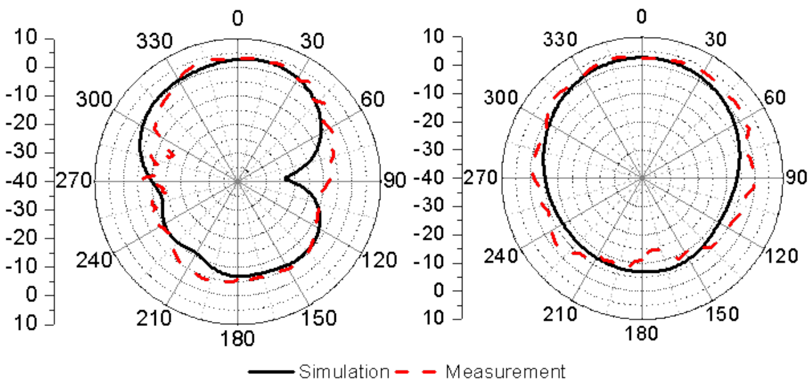

Figure 6.11. 2-D realized gain patterns (dBi) for the monopole antenna on the phantom-loaded shoe toe-box for $f = 7.25GHz$. Simulated (first row) and measured (second row) for $\phi = 0°$ (first column) and $\phi = 90°$ (second column).

6.4.2. Vivaldi Antenna on the Shoe Heel Counter Loaded with Phantom Foot

The model of the Vivaldi antenna placed on the shoe heel counter is shown in Fig. 6.12. Fig. 6.13 shows the simulated and measured results for the antenna mounted on the heel counter for the phantom-loaded shoe, the real foot-loaded shoe and the empty shoe.

There is good agreement between the simulation and the measurements. Considering the empty shoe and the body loaded case, there is a frequency shift of 400 MHz due to the dielectric loading of the foot. Although the simulated 6-8.5 GHz band is -15 dB matched, the measured S_{11} match is reduced to 11 dB. The pattern comparison is shown in Fig. 6.15 and in Fig. 6.14.

When mounted on the heel counter, the principle pattern points towards $\theta = 27.5°$, $\phi = 180°$ with an 8.5 dBi gain at 8.5 GHz. The common -3 dB beamwidth across 6-8.5 GHz is $20° < \theta < 35°$, $\phi = 180°$. While the heel counter aligns the antenna towards the body, the main radiation lobe is pointing to an off-body direction. This is attributed to the high reflection coefficient due to the high permittivity of the body tissues.

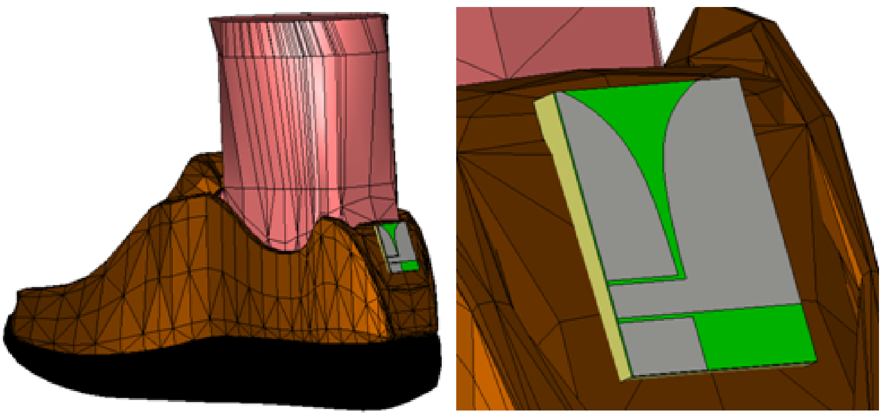

Figure 6.12. Velcro-attached Vivaldi antenna located on the phantom-loaded shoe Heel Counter.

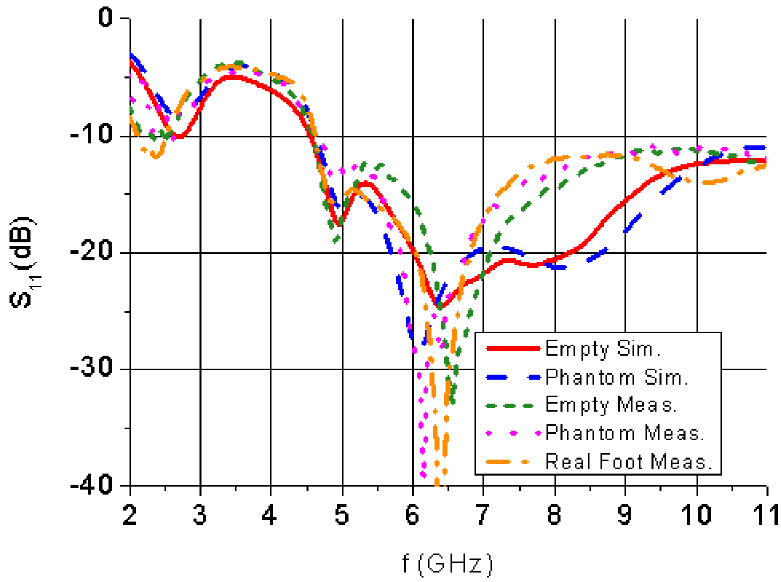

Figure 6.13. S_{11} (dB) simulation-measurement comparison for the Vivaldi antenna located on the the heel counter of an empty/phantom/human loaded shoe.

From the 2-D polar plots of Fig. 6.14, it is clear that the agreement between simulation and measurement is good.

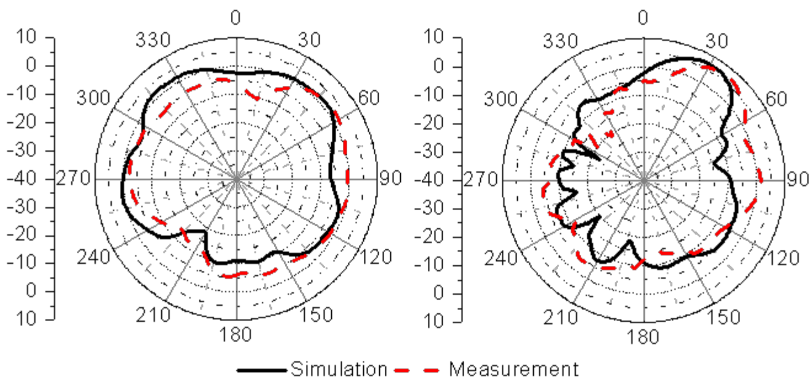

Figure 6.14. 2-D realized gain patterns (dBi) for the heel counter Vivaldi antenna simulated and measured for $\phi = 90°$ (first) and $\phi = 180°$ (second) at 7.25 GHz.

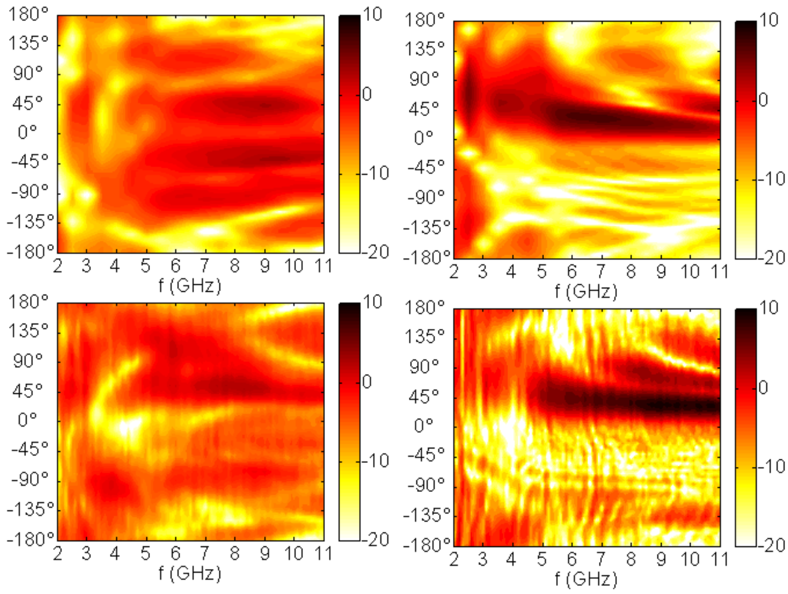

Figure 6.15. 3-D realized gain patterns (dBi) for the Vivaldi antenna on the heel counter of the phantom-loaded shoe. Simulated (first row) and measured (second row) for $\phi = 90°$ (first column) and $\phi = 180°$ (second column).

6.4.3. Vivaldi Antenna on the Shoe Lateral Quarter Loaded with Phantom Foot

The lateral quarter of the shoe, shown in Fig. 6.16, was selected for its increased rigidity compared with the vamp (midfoot) area which flexes with the kinematic function of the foot. The S_{11} results are shown in Fig. 6.17.

There is good agreement between the simulations and the measurements. The antenna is -11 dB matched in the 6-8.5 frequency band considering the measured phantom-load case. The phantom loaded response is similar to that of a real foot and while the frequency shifts downwards the antenna remains impedance matched.

The pattern comparisons are shown in Fig. 6.19 and in Fig. 6.18. The beam shape remains consistent in the UWB frequency range.

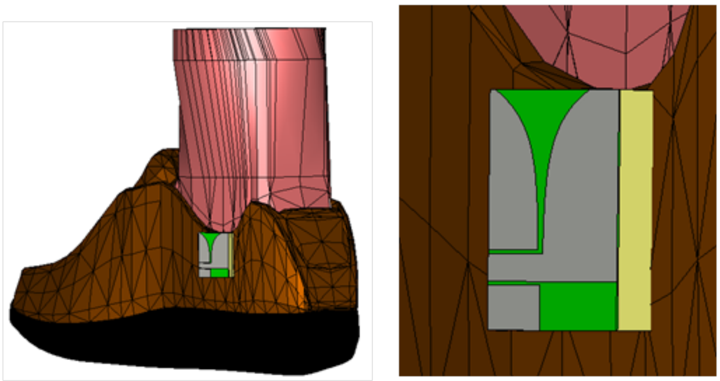

Figure 6.16. Velcro-attached Vivaldi antenna located on the phantom-loaded shoe lateral quarter.

The maximum realized gain is equal to 7.32 dBi at $\theta = 50°$, $\phi = 90°$ with a -3 dB beamwidth of $40° < \theta < 72°$.

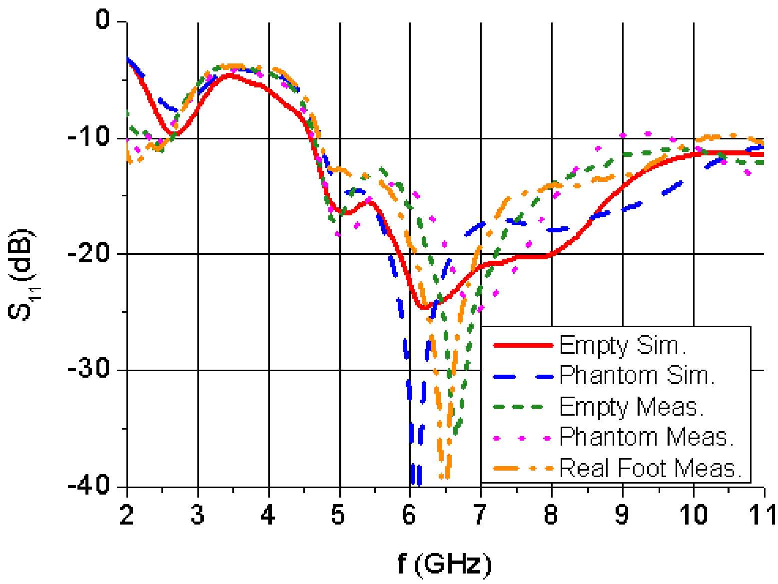

Figure 6.17. S_{11} (dB) simulation-measurement comparison for the Vivaldi antenna located on the lateral quarter of an empty/phantom/human loaded shoe.

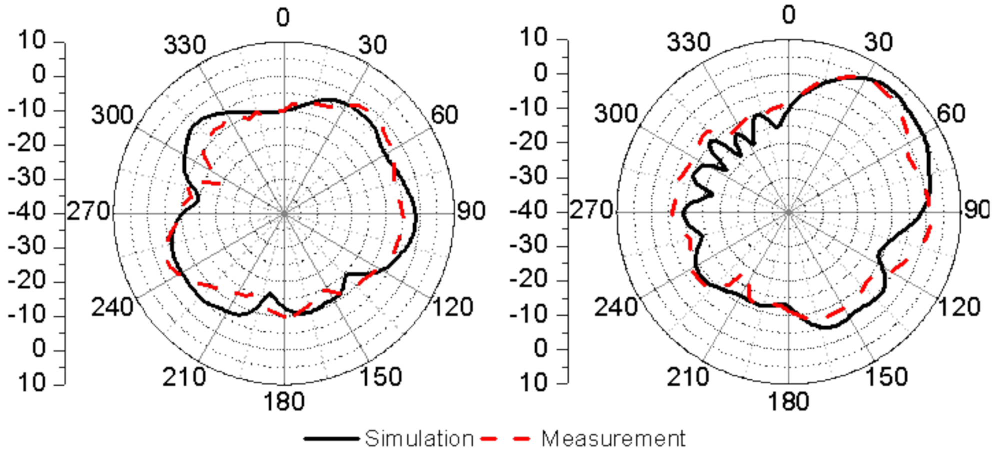

Figure 6.18. 2-D realized gain patterns (dBi) for the lateral quarter Vivaldi antenna simulated and measured for $\phi = 0°$ (first) and $\phi = 90°$ (second) at 7.25 GHz.

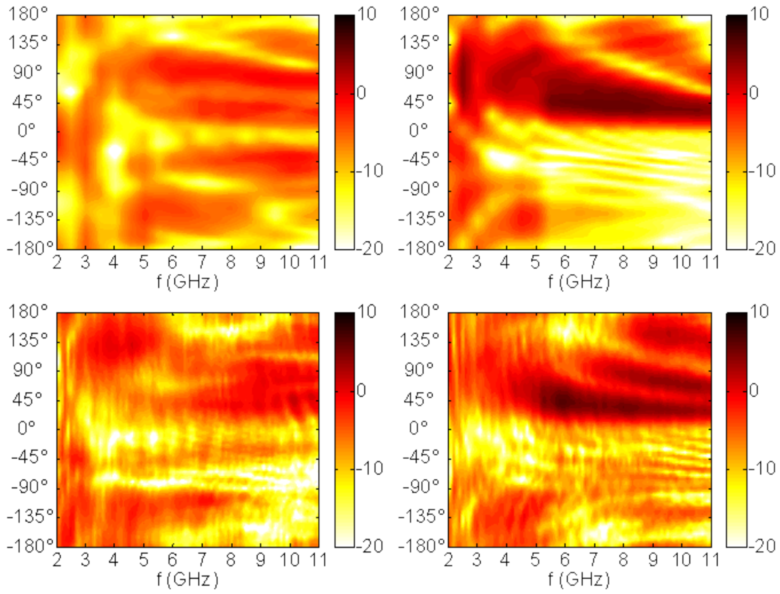

Figure 6.19. 3-D realized gain patterns (dBi) for the Vivaldi antenna on the lateral quarter of the phantom-loaded shoe. Simulated (first row) and measured (second row) for $\phi = 0°$ (first column) and $\phi = 90°$ (second column).

6.5. Analysis of Human Gait

The distribution of the E-field [19, 114] is investigated to gauge the effects of the path loss, multipath, and shadowing that would occur between footwear antennas and the upper/off-body areas. While the E-field is strictly correlated to the S_{21} parameter, the alternate simulation of two antennas would have limited results to the characteristics (polarization, alignment efficiency, matching, etc.) of the receiving antennas in upper body areas. The E-field intensity for the upper body areas provides generic insight for the performances of the footwear antennas and their positions. The upper body area E-field was investigated for the 7.25 GHz centre frequency and the reported values were normalized with respect to the maximum value at the antenna feed. Three full body models, which were selected from a 120 frame walking cycle sequence using the Make Human software application, are shown in Fig. 6.20.

The models represent a 25 year old female, 1.68 m in height, for the walking phases of left-leg terminal-swing phase (pose frame 7), left-leg mid-stance (pose frame 40) and the left-leg toe-off (pose frame 85) [115]. The poses summarize the maximum stride ranges and the mid-stride po-

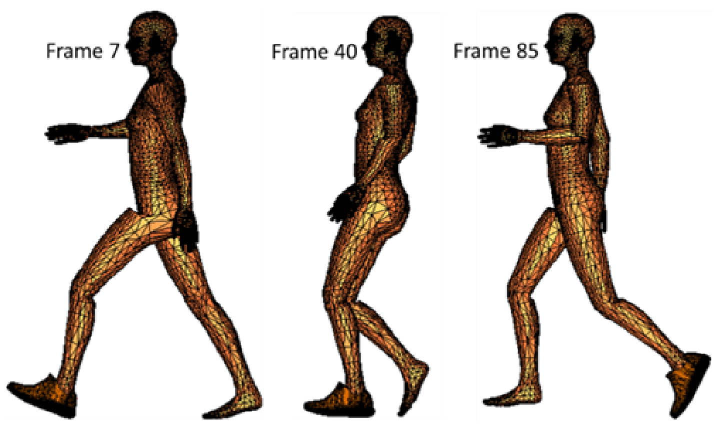

Figure 6.20. CST models of three phases of human gait motion; left leg terminal-swing phase, left-leg mid-stance and left-leg toe-off.

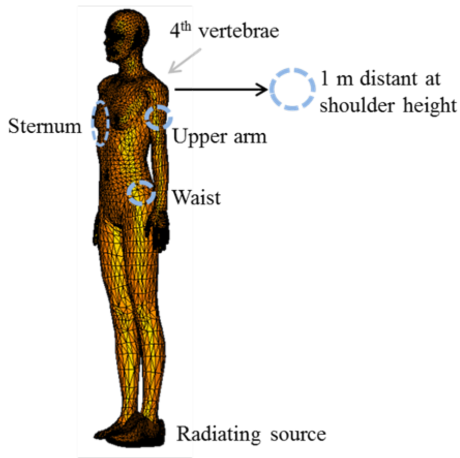

Figure 6.21. Human body locations for E-Field monitors.

sition of the human gait cycle. For partial indoor conditions, the models were configured above a steel-reinforced concrete floor surface [109]. The human body is characterized as 2/3rd the electrical properties of the muscle. Five locations were selected shown in Fig. 6.21, namely the left waist, the left upper arm, the sternum area, the 4th vertebra area and off-body at 1 m distant from the shoulder.

These positions represent communication scenarios for links with the foot area; a waist-belt clipped device, an arm strapped device, chest and back sensors or an off-body device. The simulated normalized E-field values are reported in Table 6.2 from inspecting $\pm$ 2.5 dB resolution field plots of the received fields at the upper-body probe points. The fluctuations are due to body or hand shadowing during the gait cycle. A shoulder-height off-body link at a 1 m distance was used to evaluate the footwear antenna performance with the least shadowing from the limbs or torso. The toe-box antenna has a good connection with the upper arm until the shadowing in the left-leg toe-off stance degrades it, corresponding to frame 85.

While the lateral quarter antenna link to the upper arm incurs less variability, the heel counter design is the most effective when the heel rises in the left-leg toe-off. Direct line of sight conditions produce a normalized value of E-field equal to -65 dB for full leg extensions, i.e. the toe-box antenna connects to the sternum area or correspondingly the heel counter antenna with the 4th vertebra area for frame 85. However, with the opposite stance the intensity decreases by $\sim$ 25 dB. In contrast, the lateral quarter antenna connectivity to the sternum area is steady at -90 dB for each stance, while it fluctuates by 25 dB in the 4th vertebra area. This is attributed to shadowing from the arm swing or the torso. Connectivity to the waist is the least to fluctuate during the gait cycle, with some shadowing of the hand producing additional reduction from a typical -85 dB value. If a combination of antennas were considered from the three positions on the foot, a minimum value of E-field equal to -90 dB would be achieved. The range of values in Table 6.2 indicate the impact of shadowing, multipath and line of sight performances on various footwear antenna positions for connection with the upper-body areas. In general, the toe-box monopole antenna offers a good communication link for the ventral side of the coronal plane which is suited to front belt clip or handheld devices. Alternatively, the Vivaldi antennas provide good coverage for dorsal side of the coronal plane and one side of the sagittal plane.

Table 6.2. Normalized E-field (dB) to upper body positions.

Position	Toe-Cap			Lateral Quarter			Heel Counter		
frame number	[7]	[40]	[85]	[7]	[40]	[85]	[7]	[40]	[85]
1 m from shoulder	-75	-70	-80	-75	-80	-82.5	-80	-80	-80
Upper arm	-75	-80	-90	-85	-85	-82.5	-90	-90	-75
Sternum area	-65	-70	-90	-90	-90	-90	-90	-100	-95
4th vertebra	-77.5	-90	-80	-100	-80	-75	-95	-90	-70
Waist	-90	-85	-85	-80	-85	-85	-85	-85	-85

6.6. Time-Domain On-Body Antenna performance

6.6.1. Simulation Model

For the analysis of the time-domain performance a homogeneous human body phantom with a tissue dielectric of $\epsilon_R = \sim 30$ (which is equivalent to frequency dependent 2/3rd permittivity of muscle) is used. The human body is a 1.75 m tall female in a standing posture with the arms along the body, as shown in Fig. 6.22.

The model was created using Make Human and the posture modified with Blender. The FF assessment of pulse distortion was calculated at different on-body locations: right and left upper arms, right and left waist, right and left ankles, sternum and 4th vertebra of spine as described in Fig. 6.22. Probes were located 10 mm distant from the body at each location except for the sternum and 4th vertebra where the distance was 20 mm. The simulation considered three different ground surface scenar-

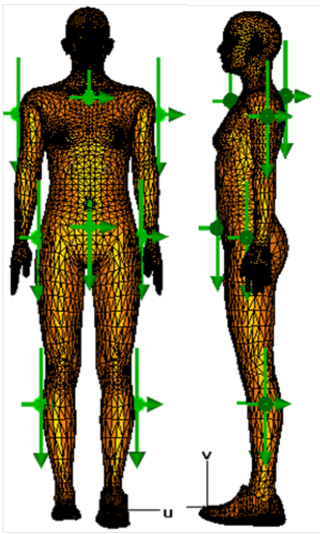

Figure 6.22. Human body model with probe locations for FF calculation.

ios for each transmitting antenna: no ground, PEC ground and reinforced concrete (ϵ_R=6, σ=1.95 mS/m) [109]. The input signal is an RCC with a roll-off = 0.5, centred at 7.9872 GHz and with a 499.2 MHz bandwidth, as shown in Fig. 1.12. The various ground scenarios represent a range of raised foot and underfoot surfaces in possible indoor and outdoor areas. The footwear upper material is leather and the sole is rubber.

6.6.2. Vivaldi Antenna on Heel Counter

The FF is calculated using E-Field probes in the described positions and a Vivaldi antenna on the heel counter as a transmitting antenna [69]. The results are summarized in Table 6.3.

The FF was greater than 0.8 for all the ground topologies and on-body positions. In particular, the sternum area is characterized by the lower values. While the presence of the PEC improves it slightly, the presence of the reinforced concrete ground causes deterioration. The ground did not influence the FF for the right ankle, and right and left upper arm, because they are located far away from the ground and the received scattered signal is small in comparison to the main component. The signal shape deteriorated more for the left waist with a PEC ground because it is a region closer to

Table 6.3. Simulated fidelity factor for the Vivaldi antenna on the heel counter.

Location	% of Fidelity Factor		
	Free Space	Reinforced Concrete	PEC
Right Ankle	99.5	99.6	99.6
Left Ankle	99.5	99.6	98.5
Right Waist	99.3	93.8	97.9
Left Waist	99.7	98.3	83.0
Front Waist	99.7	99.1	96.2
Right Upper Arm	99.7	99.5	99.1
Left Upper Arm	99.7	99.6	99.5
Sternum	84.7	82.6	85.2
4th vertebra	99.6	92.9	89.5

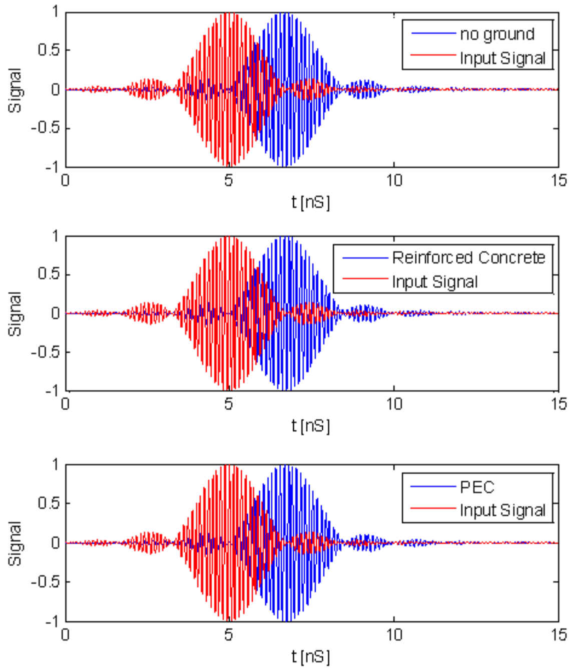

Figure 6.23. Received and input pulses for the right ankle locations for different grounds.

the ground and the antenna. An example of a signal, with a FF greater than 0.995, is shown for the right ankle for the different ground conditions in Fig. 6.23.

The three received signals preserved their shape for different grounds. The FF was always greater than 0.8 and the antenna preserved the shape of the transmitted pulse for the different grounds and for all the locations. A representation of simulated E-Field for the Vivaldi antenna on the lateral quarter is shown in Fig. 6.24. The signal in this case propagates from the bottom to the top, and there is no influence on the FF.

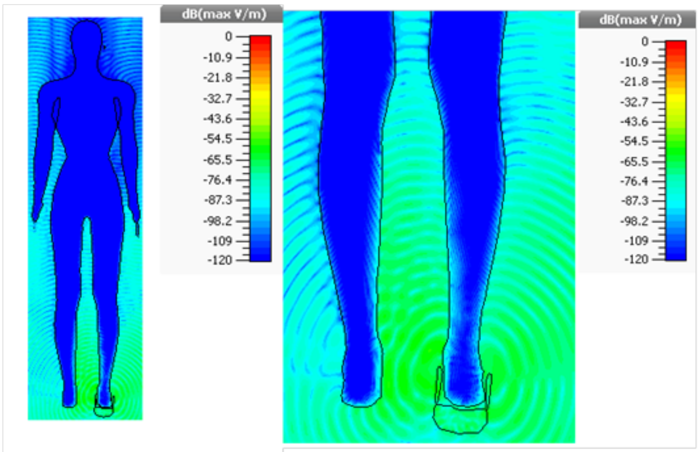

Figure 6.24. Normalized E-Field at 7.25 GHz for the transmitter located on the heel counter without ground.

6.6.3. Vivaldi Antenna on Lateral Quarter

In this section the result of the FF for the Vivaldi antenna located on the lateral quarter are described. The results are summarized in Table 6.4.

The FF was greater than 0.8 for all the cases except for the right upper arm, where the value was 0.720. However, as the ground plane becomes more conductive, there are signal components that reached the left upper arm with an improvement of the FF. The presence of the PEC ground

Table 6.4. Simulated fidelity factor for the Vivaldi antenna on the lateral quarter.

Location	% of Fidelity Factor		
	Free Space	Reinforced Concrete	PEC
Right Ankle	98.2	95.1	95.7
Left Ankle	99.7	99.7	99.7
Right Waist	98.6	96.6	99.1
Left Waist	97.8	99.4	99.6
Front Waist	98.1	97.2	95.5
Right Upper Arm	72.0	75.6	89.3
Left Upper Arm	99.4	99.5	99.4
Sternum	91.4	94.6	94.7
4th vertebra	99.1	99.2	99.5

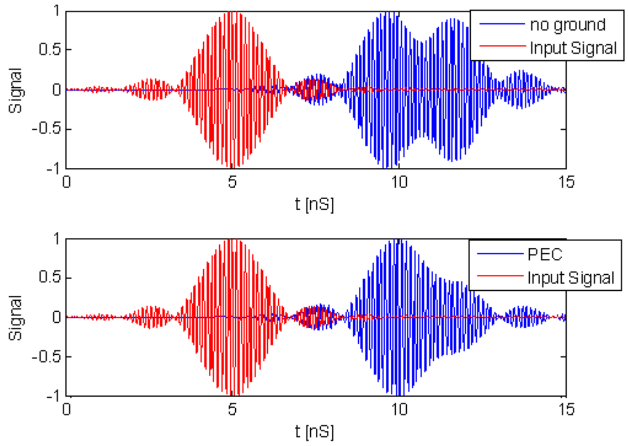

Figure 6.25. Received and input pulses for the right upper arm locations for different grounds.

generally improved the FF performance for all the locations except for the right ankle and front waist. To show the effect of the PEC ground on the improvement of the right upper arm, the received signal shape is shown in Fig. 6.25.

The presence of the PEC changed the shape of the received pulse, making it more similar to the transmitted pulse. Without the ground, there are two different pulses summed with different time shifts, distorting the symbol.

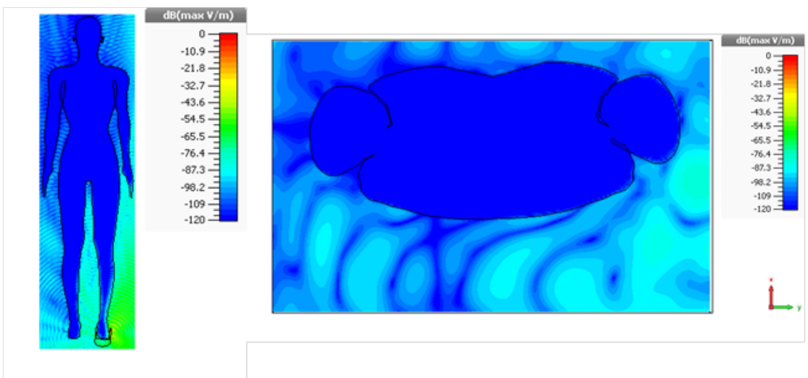

Figure 6.26. Normalized E-Field at 7.25 GHz for the transmitter located on the lateral quarter without ground.

They represent the two different components transmitted from each side of the body. With the PEC, one of these components is reduced, making the signal shape similar to the input symbol. The reinforced concrete ground improved the FF for the left side of the human body, and degraded it for the right side except for the upper arm location. A representation of the E-Field for the Vivaldi antenna on the lateral quarter is shown in Fig. 6.26. There are two components of the E-field propagating from the sides of the body, with constructive interferences of time-shifted pulses with similar amplitude at the right upper arm probe, decreasing the value of the FF.

6.6.4. Monopole Antenna on Toe Cap

The results of the FF for the toe cap antenna are shown in Table 6.5. The FF results were always greater than 0.8. However, the value of FF for the sternum area was just greater than 0.8. This is due to on-body reflections from the head that distort the pulse shape, as shown in Fig. 6.27.

The monopole antenna on the toe cap is slightly influenced by the presence of the different ground types, except for the sternum area and the 4th vertebra. This is due to its position on the shoe, because the antenna back lobe radiation is reflected back by the presence of the toes and foot,

Table 6.5. Simulated fidelity factor for the monopole antenna on the toe cap.

Location	% of Fidelity Factor		
	Free Space	Reinforced Concrete	PEC
Right Ankle	99.8	99.8	99.6
Left Ankle	99.5	99.8	99.7
Right Waist	99.2	98.5	99.6
Left Waist	99.7	99.7	99.7
Front Waist	99.8	99.8	99.8
Right Upper Arm	99.7	99.7	99.6
Left Upper Arm	99.7	99.7	99.7
Sternum	83.8	90.0	81.6
4th vertebra	99.3	99.6	98.2

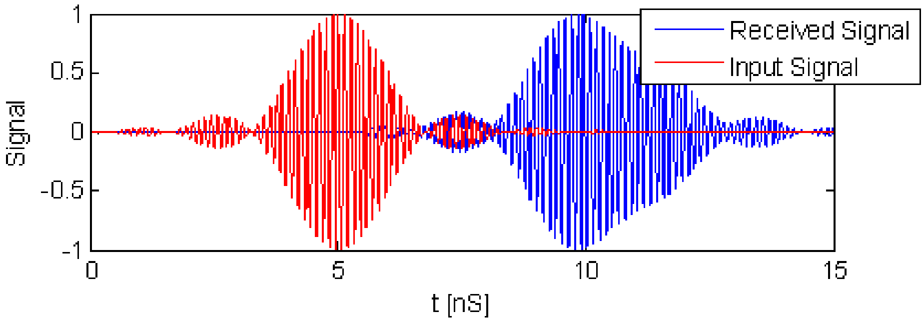

Figure 6.27. Received and input pulses for the sternum area without ground.

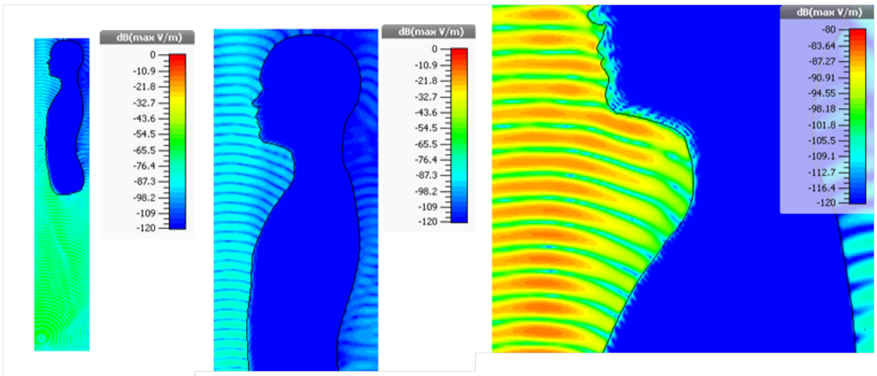

Figure 6.28. Normalized E-Field at 7.25 GHz for the transmitter located on the toe cap without ground.

reducing the interactions with the ground.

The greatest difference in FF is observed for the sternum area for which a reinforced concrete ground improves values while PEC impairs it slightly. This is due in part to the probe being offset by 20 mm from the body surface compared with the other probes which are offset by 10 mm. A representation of the E-field for the monopole antenna on the heel counter is shown in Fig. 6.28.

There is a small component of a reflected wave from the head, which alters the signal shape decreasing the FF.

6.7. Conclusions

In this chapter the performance of novel UWB antennas are investigated for three different footwear locations. The antennas are optimized to direct the main beam of the radiation pattern towards the upper body. The frequency domain performance of the antenna showed that the main beam for the Vivaldi antennas is reflected by the presence of the body. The radiation pattern shape of the monopole antenna is not modified by the presence of the body and it is characterized by greater intensity of realized gain above the ground. An investigation of the on-body E-field showed that human body movements influence the communication link, with the monopole antenna demonstrating the best performances. The investigation of the time-domain performance of the three footwear antenna locations demonstrates the high capability of the antenna to preserve the pulse shape for on-body communication links. The monopole antenna is not influenced by the presence of the ground due to the presence of the body. The Vivaldi antennas show greater sensitivity to ground types because of a non-perfect end-fire radiation pattern. The most difficult on-body area to reach for all the antennas is the sternum area, because of the presence of reflections from the head. All the antennas have a FF greater than 80% for all body locations except the right upper arm for the lateral quarter antenna. The investigated antennas are suitable for integration in the footwear because of the low profile and are suitable for UWB on-body communication due to high realized gain values and pulse preservation properties.

7. Comparison of Foot-centric and Waist-centric BANs

7.1. Introduction

In Section 6, monopole and Vivaldi antennas are investigated on various locations on footwear. It was shown that, for different body postures, the Vivaldi antenna performs better when mounted on the lateral quarter in comparison to the heel counter. The antenna substrate is 0.2 mm semi-flexible FR4 and can be easily embedded on the lateral quarter of the shoe surface. In this chapter a waist-centric model with omnidirectional antennas is compared with a footwear-centric model with directional antennas. A hub [10, 116] is a smarter node which coordinates other simpler nodes located on the body and usually acts as a gateway to relay the information to an off-body node. The conventional choice for the hub position is the waist region [26], because it is the on-body region equidistant from all the different on-body locations. Nodes can be located in various directions with respect to the hub position, thus omnidirectional antennas are required to cover the whole body area. The advantage of a footwear-centric location is that all the sensors are located on the upper side of the body, so the main beam of the antenna can be directed in one direction and efficiently cover the entire human body. In contrast to a waist-centric system, the nodes in a footwear-centric system are more distant, but this can be compensated for by using antennas with greater gain. In this chapter, both systems are compared using two different subjects walking in an indoor environment.

The results are described considering the 802.4.16 IEEE WBAN standard [10] that defines the maximum achievable data rate as a function of the path loss.

7.2. Antennas for Foot-Centric and Waist-Centric BANs

The antenna designs used here have evolved from those described in Section 6, but are slightly bigger.

7.2.1. The Monopole Antenna

A monopole antenna is designed on 0.2 mm single-sided FR4 as shown in Fig. 7.1. It is fed by a 50 Ω coplanar waveguide (CPW). Compared to the previous antenna in Section 6, the ground plane is larger in order to minimize the current flowing on the cable.

The antenna dimensions are shown in Table 7.1.

The ground plane employs two different spline combinations to improve

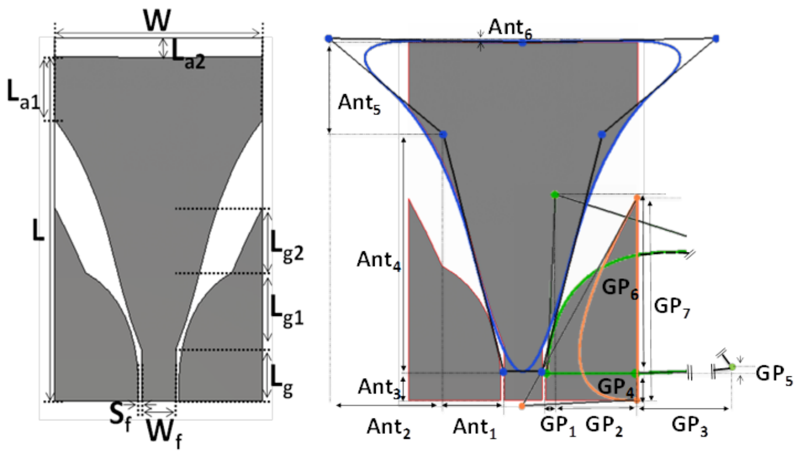

Figure 7.1. Geometry of the monopole antenna and with spline point.

Table 7.1. Dimensions of the monopole antenna.

Parameter	Dimension [mm]	Parameter	Dimension [mm]
W_f	3.33	L	32.8
S_f	0.28	L_{a1}	5.72
L_g	4.66	L_{a2}	1.69
L_{g1}	6.97	W	20
L_{g2}	5.87		

Table 7.2. Dimensions of the spline of the ground plane and antenna.

Parameter	Dimension [mm]	Parameter	Dimension [mm]
Ant_1	5.20	GP_1	0.75
Ant_2	9.86	GP_2	7.3
Ant_3	2.64	GP_3	40
Ant_4	20.42	GP_4	2.64
Ant_5	8.23	GP_5	1.16
Ant_6	0.34	GP_6	16.12
		GP_7	17.5

the wideband antenna matching. The antenna shape is obtained from one spline with 7 points. Some sections of the antenna and the ground plane geometry are cut away. The coordinates of the points belonging to the antenna and ground plane splines are summarized in Table 7.2

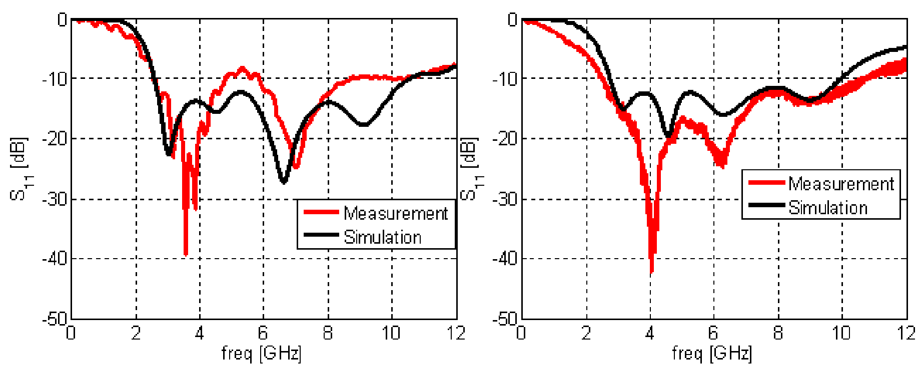

Figure 7.2. Free space and on-body simulated and measured S_{11} (dB) for the monopole antenna.

The simulated and measured S_{11} for the antenna in free-space and for the on-body case is shown in Fig. 7.2.

For simplicity the simulation model considers the body as a muscle brick with the antenna a distance of 6 mm away. In free space the antenna has a $S_{11} < -10$ dB between 3 and 10 GHz, while the body proximity increases this bandwidth slightly. The monopole antenna efficiency is 25% and 48.5% at 4 GHz and at 8 GHz respectively when in close proximity to the body.

7.2.2. The Vivaldi Antenna

The Vivaldi antenna is prototyped on a substrate 37.1 x 37.1 x 0.2 mm with a curve which is described in Equation 7.1.

$$z = 0.191e^{0.173y} \tag{7.1}$$

with

$$0 < y < 21[mm] \tag{7.2}$$

It provides a directional radiation pattern towards the upper body which minimizes interference to off-body networks. The antenna is based on the geometry described in Section 6 and it is shown in Fig. 7.3

The ground plane of this Vivaldi is bigger than the antenna described in Section 6. The dimensional parameters are summarized in Table 7.3. The free-space and the on-body simulated and measured S_{11} for the antenna

Table 7.3. Dimensions of the Vivaldi antenna.

Parameter	Dimension [mm]	Parameter	Dimension [mm]
W_f	3.1	V_s	0.6
S_f	0.2	V_1	10.9
GP_1	12.3	V_2	11.6
GP_2	21.1	V_3	24.5
L_1	25.3	L_2	11.8

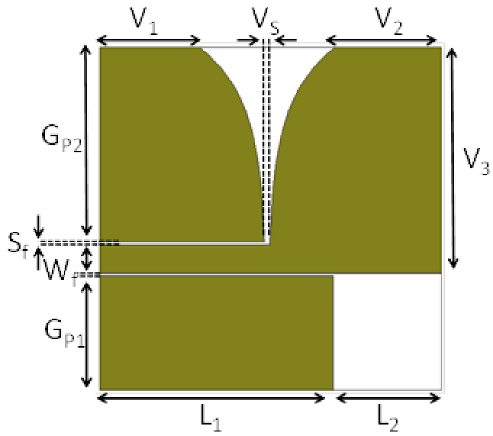

Figure 7.3. Vivaldi antenna geometry.

are shown in Fig. 7.4. The on-body simulations correspond to the antenna positioned on the lateral side of the left shoe, 10 mm from the foot.

The antenna has a $S_{11} < 10$ dB in the lower and higher European UWB bands (3.1 GHz-4.8 GHz and 6.0 GHz-8.5 GHz). The on-body Vivaldi antenna is 50% and 56% efficient at 4 GHz and 8 GHz respectively with realized gain values of 5.1 dBi at 4 GHz and 6.4 dBi at 8 GHz.

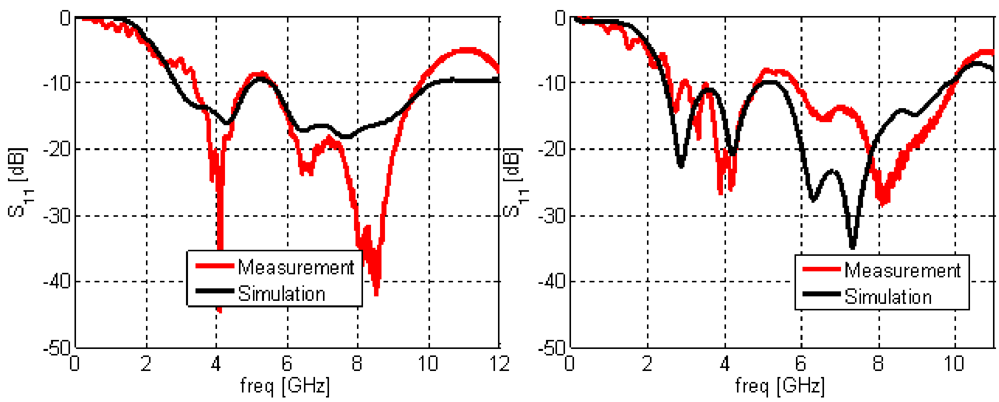

Figure 7.4. Free-space and on-body S_{11} (dB) for the Vivaldi antenna.

7.3. On-body Channel Measurements

7.3.1. Measurement Setup

Three link configuration cases are described :

- Case 1: Waist-centric hub monopole and node monopole antennas (M/M);
- Case 2: Footwear-centric hub Vivaldi and node Vivaldi antennas (V/V);
- Case 3: Waist-centric hub monopole and node Vivaldi antennas (M/V).

While the hub is located on the left footwear or on waist, the other nodes are located on the left and right upper arms, the sternum and the 4th vertebra, as shown in Fig. 7.5.

261 link measurements were recorded per person for the hub-node combinations under the following circumstances:

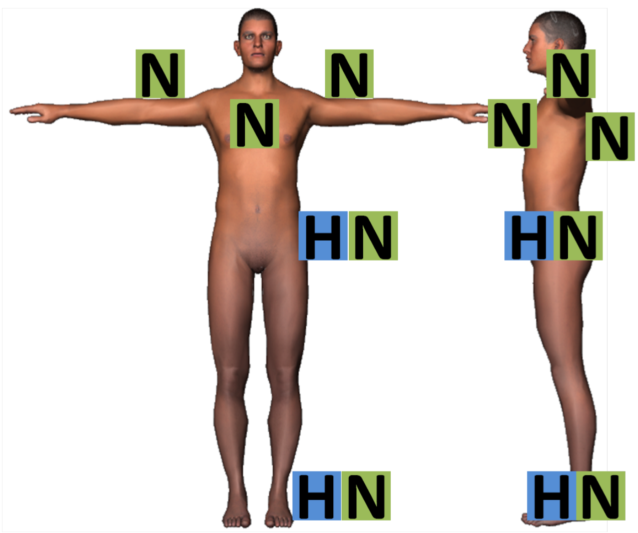

Figure 7.5. Positions of the hubs and nodes for the waist- and footwear-centric systems.

Case 1 represents the classical on-body solution for on-body communication, where the hub and the nodes are characterized by omnidirectional antennas. Case 2 represents the solution proposed here, with directional antennas both in the hub and in the different nodes. Case 3 is a combination of Case 1 and 2, with directional antennas on the nodes and an omnidirectional antenna on the waist as a hub. The model with a Vivaldi antenna on a waist-centric system (V/M or V/V) is excluded because the antenna can't cover all the different directions. The measurements were performed on two subjects (height 1.75 m and weight of 70 kg and 80 kg) in an 8 m x 8 m laboratory area with metallic furniture and reinforced concrete floor and ceiling. S_{21} values were recorded for the low and high band frequencies of 3.9936 GHz and 7.9872 GHz with a bandwidth of 499.2 MHz. These bands were selected as they are the mandatory regional bands for IEEE 802.15.6 UWB impulse radio (IR).

- *standing static channel*: The first 4 second period is for a subject in a standing position in a static channel;
- *walking static channel*: The next 12 second period is for a subject walking in a static channel, and;
- *standing dynamic channel*: The last 10 second period is for a subject standing in a dynamic channel with people moving randomly near the subject in the laboratory.

7.3.2. Measurement Results

Inspection of the data indicates that the right upper arm exhibits the least path gain from the left foot and left waist due to shadowing of the direct path. Low-band path gains for the three hub-node configurations for right upper arm with the left foot and left waist of the 70 kg subject are shown in Fig. 7.6.

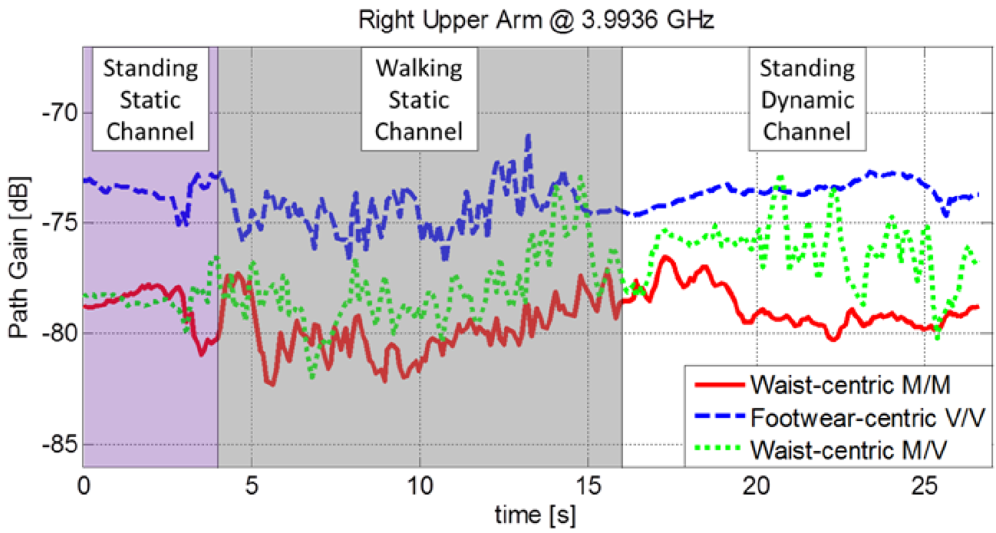

Figure 7.6. Comparison of the measured S_{21} (dB) for the three systems.

The S_{21} results are stable for the first 4 seconds (Standing Static Channel), then it oscillates for the Walking Static Channel and it is again stable for the Standing Dynamic Channel. Despite the increased distances between the left footwear and the right upper arm compared to the left waist to right upper arm, it is evident that the footwear-centric arrangement outperforms the waist-centric approach. Using directional antennas in the waist-centric system improves the performances. The cumulative distribution functions (CDFs) of the measured path gain for each hub-node configuration are shown in the following figures. The increased horizontal spread of values denotes shadowing, antenna pattern misalignment and fading variations, etc., that are due to body movement. The high band performs better than the low band for the left and right upper arm, as shown in Fig. 7.7 and Fig. 7.8. This is due to the predominance of free-space waves compared to surface wave propagation for these links.

In other cases, the low band is better since there is less path loss at lower frequencies as shown in Fig. 7.9, Fig. 7.10 and Fig. 7.11. In most of the analysed cases, the footwear-centric configuration performs better than the

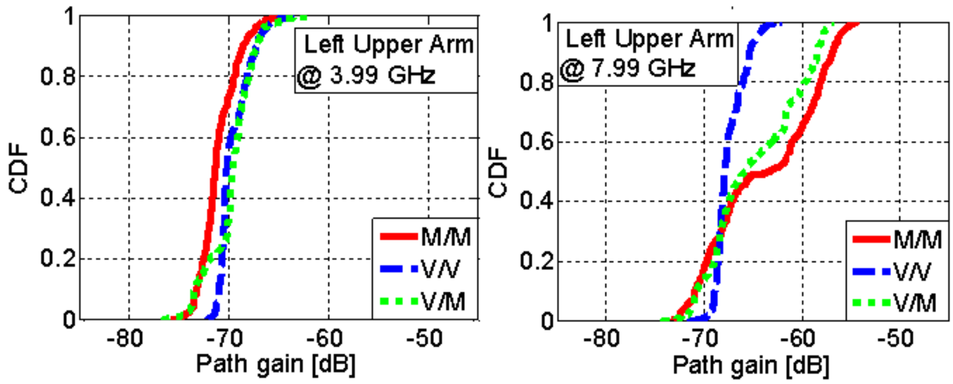

Figure 7.7. Low frequency and high frequency path gain for the left upper arm.

waist-centric configuration. An exception is the sternum area, where the distance between the hub and sensor node in the waist-centric system is significantly shorter, as observed in Fig. 7.9.

The CDFs results are summarized in Table 7.4 which shows the maximum data rates achieved for an IEEE 802.15.6 compliant IR-UWB system. The measured data-rates are based on the received signal strength calculated using the path gain and the maximum transmitter power. For example, the minimum and maximum data rates of 0.3948 Mbps and 12.636 Mbps correspond to the received signal strength of -91 dBm and -76 dBm, respectively. Where the minimum 0.3948 Mbps data rate was not guaran-

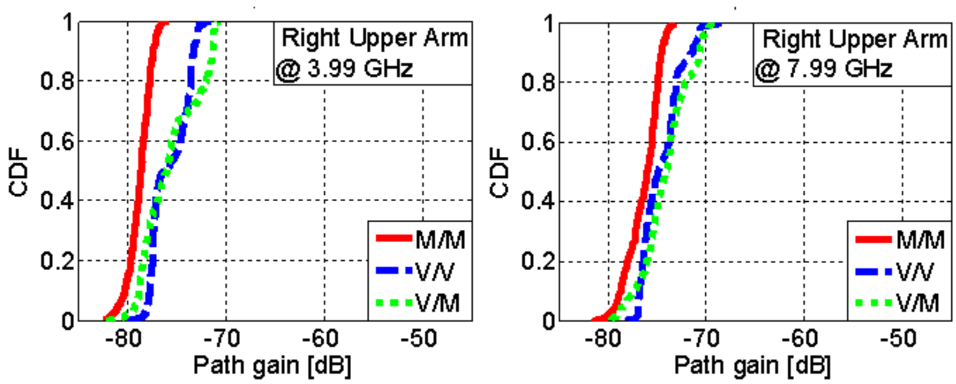

Figure 7.8. Low frequency and high frequency path gain for the right upper arm.

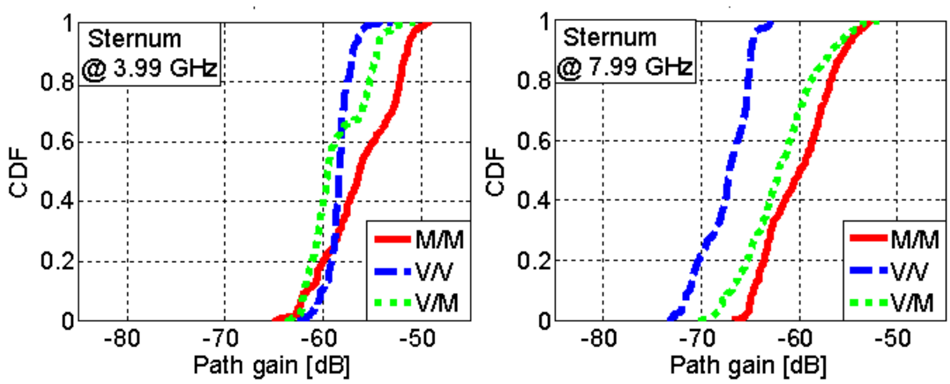

Figure 7.9. Low frequency and high frequency path gain for the sternum area.

teed due to path gains being less than -76.7 dB, the outcomes are reported as the percentage of successful 0.3948 Mbps data rate measurements. Inspection of the data rates in Table 7.4 indicates that the footwear-centric system performance matches or is better than a waist-centric system, except for the sternum area. In fact, the footwear-centric system is significantly better for nodes on the vertebra since the footwear hub location mitigates the shadowing impact. The right upper arm area is the furthest location from the left foot hub and it is not possible to guarantee a minimum data rate for all the measurements. However, the footwear-centric hub provides better link availability for the lowest data rate.

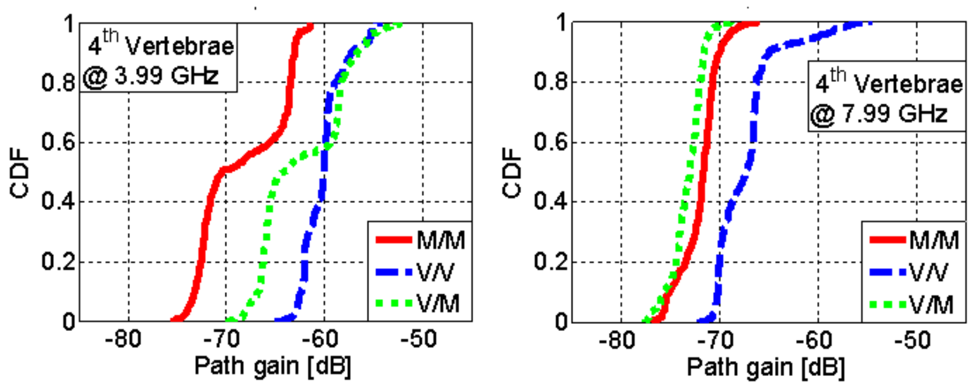

Figure 7.10. Low frequency and high frequency path gain for the 4th vertebra.

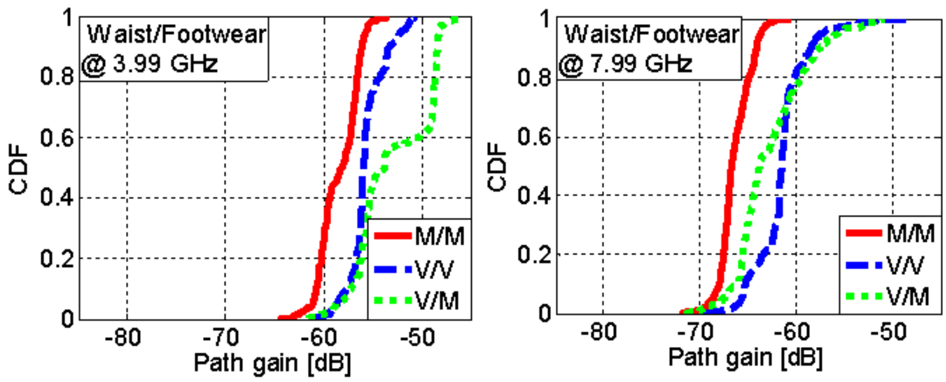

Figure 7.11. Low frequency and high frequency path gain for the waist/footwear location.

Table 7.4. Achieved maximum data rates for 522 path gain measurements across two subjects for the M/M, M/V and V/V WBAN configurations.

Frequency	3.99 GHz			7.99 GHz		
Hub and Antenna Positions	Waist-centric [Mbps]		Footwear-centric [Mbps]	Waist-centric [Mbps]		Footwear-centric [Mbps]
	M/M	M/V	V/V	M/M	M/V	V/V
Footwear/Waist	6.3	12.6	12.6	0.8	0.8	1.6
Left Upper Arm	0.4	0.4	0.8	0.8	0.4	0.8
Right Upper Arm	0.2%	57%	87%	61%	57%	86%
Sternum	3.2	6.3	6.3	3.2	1.6	0.8
4th vertebra	0.4	1.6	3.2	99%	96%	0.8

7.4. Conclusions

In this chapter a waist-centric system with omnidirectional and directional antennas was compared with a foot-centric system using directional antennas. The series of measurements demonstrates that for different on-body locations the footwear-centric system matches or outperforms the waist-centric system. The results are described in terms of maximum data rate considering the IEEE 802.4.16 standard on Wireless Body Area Networks. The footwear-centric system has a data rate greater than 0.8 Mbps for the low frequency range and 0.4 Mbps for the high frequency range with the exception of the right upper arm.

8. Conclusions And Future Work

8.1. Conclusions

The main goal of this thesis is to evaluate procedures for footwear antenna design and to evaluate different antenna solutions. Directional antennas on footwear can be used to improve the communication link with other on-body nodes. The reduced beamwidth mitigates multipath effects. The larger volume on footwear can accommodate different antenna solutions. The antenna design must take the body and the ground proximity into consideration, with more focus on different body postures which changes the antenna alignment. The antenna should be integrated without impairing the footwear profile or changing the spatiotemporal gait characteristics. It was demonstrated that when the thickness of the heel counter and lateral quarter is considered, a polarization parallel to the body can be used for LOS communication links between footwear and other nodes for frequencies greater than 6 GHz. Different channel measurements between the footwear and the wrist were performed in different frequency bands and the path loss distribution was found to be Rician, i.e. the dominant component is the direct path. The evaluated K factor increased and became more stable for higher frequencies. The communications link between footwear and the wrist was found to be robust to fading effects owing to the antenna directivity characteristics, which naturally reject components coming from other directions. The communication link complies with the 802.15.6 standard for each measured case for a subject standing and walking. To integrate completely the antenna in the footwear, an insole antenna was designed. In this case a 433 MHz antenna was designed to broaden the investigation towards lower frequencies. The antenna was integrated in the insole, it is lightweight, low-cost and user oblivious. A novel antenna geometry was realised to resonate at 433 MHz with a 0.2 mm separation from the foot and 20 mm distance from different ground types, as well as to radiate from the antenna sides, towards the upper body. It was finally demonstrated that the communication link using the footwear insole antenna as a hub is resilient to ground proximity, node location and body movement. For the first time UWB antenna design methodologies were proposed for footwear integration. Three footwear positions were identified and investigated: the toe cap, the lateral quarter and the heel counter. Vivaldi antennas were used for the lateral quarter and the heel counter and a monopole antenna was used for the toe cap. The on-body antenna behaviour was evaluated and it was found that the antenna reflection coefficient and radiation pattern are impaired by body proximity, requiring the antenna optimization to include the surrounding environment. The change in antenna alignment due to body movement was evaluated using simulated E-field distributions for three different body postures. The antenna performance for a walking subject depends on the antenna type, node locations and body frame in the gait cycle. Vivaldi antennas on the lateral quarter are suitable for communication with the upper arm node locations. Monopole antennas on the toe cap offer good coverage of the ventral side of the coronal plane with greater E-field intensity compared to the Vivaldi antennas for the first two gait cycle frames. The heel counter Vivaldi antenna is limited by body shadowing for the sternum area. The lateral quarter Vivaldi antenna represents the best trade-off between the toe cap monopole and heel counter Vivaldi for a walking subject. Time domain performances for the UWB antennas were analyzed with different on-body probes. It was demonstrated that a FF greater than 0.8 was obtained for all the cases (except for the right upper arm for the lateral quarter Vivaldi antenna) and for the first time that the FF is degraded by destructive/constructive interference from different on-body surface wave components. Finally a waist-centric BAN with omnidirectional antennas is compared to a foot-centric BAN network using directional antennas. As observed, directional antennas are characterized by a higher gain and from the footwear location there is only one direction of interest. For the waist-centric system, the antenna cannot provide omnidirectional high gain and the communication link is impaired for some node locations. This concept was verified with on-body measurements for a walking subject. The footwear-centric system was proven to outperform the waist-centric system for the majority of cases.

8.2. Future Work

The analysis and investigation of footwear antennas raises different issues in the antenna and propagation models. The design methodologies of locating an antenna on footwear are now established. More work is required on footwear integrated antennas for off-body communications and, in particular, to provide omnidirectional coverage with minimum body shadowing. Furthermore, the Vivaldi antennas investigated have a polarization tangential to the body. Further investigation should evaluate if the E-field variation for different body postures and for NLOS nodes can be reduced with on-body perpendicular polarization. New antenna concepts are required to realise low-profile directional antennas with a polarization perpendicular to the body. It was demonstrated in this thesis that the footwear-centric BAN is a new concept that can potentially revolutionize future wearable technology. Using a directional antenna as a hub located on one edge of the body improves the communication link and decreased multipath effects. Future work would include a comparison of footwear-centric systems with waist-centric systems, for narrowband and wideband channels and for outdoor non-reflective environments. On-body diversity can enable more robust communication links. The footwear location has several advantages because the antenna radiation patterns can be decoupled due to the body shadowing, using, for example a heel counter and a toe cap antenna illuminating the rear and front coronal plane, respectively.

BIBLIOGRAPHY

[1] Z. Icrupka, "The Effect of the Human Body on Radiation Properties of Small-Sized Communication Systems," *Trans. Antennas Propag.*, vol. 16, no. 2, 1968.

[2] H. E. King and J. L. Wong, "Effects of a Human Body on a Dipole Antenna at 450 and 900 MHz," *Trans. Antennas Propag.*, no. 3, pp. 376–379, 1977.

[3] R. J. Spiegel, "The Thermal Response of a Human in the Near-Zone of a Resonant Thin-Wire Antenna," *IEEE Trans. Microw. Theory Techn.*, vol. 30, no. 2, pp. 177–185, Feb. 1982.

[4] C. Pichot, L. Jofre, G. Peronnet, and J.-C. Bolomey, "Active microwave imaging of inhomogeneous bodies," *IEEE Trans. Antennas Propag.*, vol. 33, no. 4, pp. 416–425, Apr. 1985.

[5] T. Kashiwa, N. Yoshida, and I. Fukai, "Analysis of radiation characteristics of planar inverted-F type antenna on conductive body of hand-held transceiver by spatial network method," *Electronics Letters*, vol. 25, no. 16, pp. 1044–1045, 1989.

[6] J. Toftgird, S. N. Hornsleth, and J. B. Andersen, "Effects on Portable Antennas of the Presence of a Person," *IEEE Trans. Antennas Propag.*, vol. 41, no. 6, 1993.

[7] A. Bahr and I. Wolff, "Numerical investigation of antenna concepts for hand-held portable telephones including effects from the human

body," in *Proc. IEEE Antennas and Propagation Society International Symposium*, 1994, pp. 363–366.

[8] H. Ruoss and F. M. Landstorfer, "Slot antenna for hand held mobile telephones showing significantly reduced interaction with the human body," *Electronics Letters*, vol. 32, no. 6, pp. 513–514, 1996.

[9] C. Baber, J. Knight, D. Haniff, and L. Cooper, "Ergonomic of Wearable Computers," *Mobile networks and Applications*, vol. 4, pp. 15–21, 1999.

[10] "IEEE Standard for Local and metropolitan area networks Part 15.6: Wireless Body Area Networks - 2012."

[11] B. Najafi, K. Aminian, A. Paraschiv-Ionescu, F. Loew, C. J. Büla, and P. Robert, "Ambulatory system for human motion analysis using a kinematic sensor: monitoring of daily physical activity in the elderly." *IEEE Trans. Biomed. Eng.*, vol. 50, no. 6, pp. 711–23, Jun. 2003.

[12] R. Paradiso, G. Loriga, and N. Taccini, "A wearable health care system based on knitted integrated sensors," *IEEE Trans. on Inf. Technol. in Biomed.*, vol. 9, no. 3, pp. 337–44, Sep. 2005.

[13] R. R. Fletcher, K. Dobson, M. S. Goodwin, H. Eydgahi, O. Wilder-Smith, D. Fernholz, Y. Kuboyama, E. B. Hedman, M.-Z. Poh, and R. W. Picard, "iCalm: wearable sensor and network architecture for wirelessly communicating and logging autonomic activity." *IEEE Trans. on Inf. Technol. in Biomed.*, vol. 14, no. 2, pp. 215–23, Mar. 2010.

[14] H. H. Asada, P. Shaltis, A. Reisner, S. Rhee, and R. C. Hutchinson, "Mobile monitoring with wearable photoplethysmographic biosensors." *Engin. in Medic. and Biol. Magaz.*, vol. 22, no. 3, pp. 28–40, 2003.

[15] A. Pantelopoulos and N. Bourbakis, "A Survey on Wearable Sensor-Based Systems for Health Monitoring and Prognosis," *Trans. on Syst., Man, and Cybern.*, vol. 40, no. 1, pp. 1–12, Jan. 2010.

[16] P. S. Hall and Y. Hao, *Antennas and propagation for body-centric wireless communications*. Artech House inc., 2006.

[17] D. B. Smith, D. Miniutti, T. A. Lamahewa, and L. W. Hanlen, "Propagation Models for Body-Area Networks," *IEEE Antennas Propag. Mag.*, vol. 55, no. 5, 2013.

[18] P. Hall, Y. Hao, Y. Nechayev, A. Alomainy, C. Constantinou, C. Parini, M. Kamarudin, T. Salim, D. Hee, R. Dubrovka, A. Owadally, W. Song, A. Serra, P. Nepa, M. Gallo, and M. Bozzetti, "Antennas and propagation for on-body communication systems," *IEEE Trans. Antennas Propag.*, vol. 49, no. 3, pp. 41–58, Jun. 2007.

[19] G. A. Conway and W. G. Scanlon, "Antennas for Over-Body-Surface Communication at 2.45 GHz," *Trans. Antennas Propag.*, vol. 57, no. 4, pp. 844–855, 2009.

[20] G. Conway, W. Scanlon, and S. Cotton, "The performance of on-body wearable antennas in a repeatable multipath environment," *Proc. IEEE Antennas and Propagation Society International Symposium*, pp. 1–4, Jul. 2008.

[21] W. G. Scanlon and A. R. Chandran, "Stacked-Patch Antenna with Switchable Propagating Mode for UHF Body-Centric Communications off-body mode on-body mode," *IEEE International Workshop on Antenna Technology*, pp. 9–12, 2009.

[22] T. B. Welch, R. L. Musselman, B. A. Emessiene, P. D. Gift, D. K. Choudhury, D. N. Cassadine, and S. M. Yano, "The effect of the human body on UWB signal propagation in an indoor environment," *IEEE Trans. Antennas Propag.*, vol. 20, no. 9, pp. 1778–1782, 2002.

[23] A. Fort, J. Ryckaert, C. Desset, P. D. Doncker, P. Wambacq, and L. V. Biesen, "Ultra-Wideband Channel Model for Communication

Around the Human Body," *Journal On Selec. Areas in Comm.*, vol. 24, no. 4, pp. 927–933, 2006.

[24] Q. Wang and J. Wang, "Performance of on-body chest-to-waist UWB communication link," *IEEE Microw. Compon. Lett.*, vol. 19, no. 2, pp. 119–121, Feb. 2009.

[25] A. Alomainy, Y. Hao, C. Parini, and P. Hall, "Comparison Between Two Different Antennas for UWB On-Body Propagation Measurements," *IEEE Antennas Wireless Propag. Lett.*, vol. 4, no. 1, pp. 31–34, Dec. 2005.

[26] A. Alomainy, Y. Hao, X. Hu, C. G. Parini, and P. S. Hall, "UWB on-body radio propagation and system modelling for wireless body-centric networks," *Proc. IEEE Comm.*, vol. 153, no. 1, pp. 107–114, 2006.

[27] Y. Zhao, Y. Hao, A. Alomainy, and C. Parini, "UWB On-Body Radio Channel Modeling Using Ray Theory and Subband FDTD Method," *IEEE Trans. Microw. Theory Techn.*, vol. 54, no. 4, pp. 1827–1835, 2006.

[28] A. Alomainy, A. Sani, A. Rahman, J. Santas, and Y. Hao, "Transient characteristics of wearable antennas and radio propagation channels for ultrawideband body-centric wireless communications," *Trans. Antennas Propag.*, vol. 57, no. 4, pp. 875–884, 2009.

[29] A. Sani, A. Alomainy, G. Palikaras, Y. Nechayev, C. Parini, and P. Hall, "Experimental Characterization of UWB On-Body Radio Channel in Indoor Environment Considering Different Antennas," *IEEE Trans. Antennas Propag.*, vol. 58, no. 1, pp. 238–241, Jan. 2010.

[30] M. Klemm, I. Z. Kov, G. F. Pedersen, and G. Tröster, "Novel Small-Size Directional Antenna for UWB WBAN / WPAN Applications," *Trans. Antennas Propag.*, vol. 53, no. 12, pp. 3884–3896, 2005.

[31] J. Verbiest and G. E. Vandenbosch, "A Novel Small-Size Printed Tapered Monopole Antenna for UWB WBAN," *IEEE Antennas Wireless Propag. Lett.*, vol. 5, no. 1, pp. 377–379, Dec. 2006.

[32] J. R. Verbiest and G. A. E. Vandenbosch, "Small-size planar triangular monopole antenna for UWB WBAN applications," *Electronics Letters*, vol. 42, no. 10, pp. 9–10, 2006.

[33] Y. P. Zhang and Q. Li, "Performance of UWB Impulse Radio With Planar Monopoles Over On-Human-Body Propagation Channel for Wireless Body Area Networks," *IEEE Trans. Antennas Propag.*, vol. 55, no. 10, pp. 2907–2914, Oct. 2007.

[34] G. Almpanis, C. Fumeaux, J. Fröhlich, and R. Vahldieck, "A Truncated Conical Dielectric Resonator Antenna for Body-Area Network Applications," *IEEE Antennas Wireless Propag. Lett.*, vol. 8, pp. 279–282, 2009.

[35] N. Chahat, M. Zhadobov, R. Sauleau, and K. Ito, "A compact UWB antenna for on-body applications," *Trans. Antennas Propag.*, vol. 59, no. 4, pp. 1123–1131, 2011.

[36] L. Ma, R. M. Edwards, and W. Whittow, "A Notched Hand Wearable Ultra Wideband W Printed Monopole Antenna For Sporting Activities," in *Loughborough Antennas and Propagation Conference*, 2008, pp. 397–400.

[37] H. B. Lim, D. Baumann, and E.-P. Li, "A human body model for efficient numerical characterization of UWB signal propagation in wireless body area networks." *IEEE Trans. Biomed. Eng.*, vol. 58, no. 3, pp. 689–97, Mar. 2011.

[38] W. Thompson, R. Cepeda, G. Hilton, and M. A. Beach, "An improved antenna mounting for ultra-wideband on-body communications and

channel characterization," *IEEE Trans. Microw. Theory Techn.*, vol. 59, no. 4, pp. 1102–1108, 2011.

[39] C.-h. Kang, S.-j. Wu, and J.-h. Tarng, "A Novel Folded UWB Antenna for Wireless Body," *IEEE Trans. Antennas Propag.*, vol. 60, no. 2, pp. 1139–1142, 2012.

[40] T. Tuovinen, K. Yekeh Yazdandoost, M. Berg, and J. Iinatti, "Ultra wideband loop antenna on contact with human body tissues," *IET Microw., Antennas and Propag.*, vol. 7, no. 7, pp. 588–596, May 2013.

[41] Q. H. Abbasi and A. Sani, "On-Body Radio Channel Characterization and System-Level Modeling for Multiband OFDM," *IEEE Trans. Microw. Theory Techn.*, vol. 58, no. 12, pp. 3485–3492, 2010.

[42] Q. H. Abbasi, A. Alomainy, and Y. Hao, "Characterization of MB-OFDM-Based Ultrawideband Systems for Body-Centric Wireless Communications," *IEEE Antennas Wireless Propag. Lett.*, vol. 10, pp. 1401–1404, 2011.

[43] T. Thungren, E. Kollberg, and K. Yngvesson, "Vivaldi Antennas for Single Beam Integrated Receivers," in *12th European Microwave Conference*. IEEE, Oct. 1982, pp. 361–366.

[44] K. Yngvesson, D. H. Schaubert, T. L. Korzeniowski, E. Kollberg, T. Thungren, and M. Johansson, "Endfire Tapered Slot Antennas on Dielectric," *Trans. Antennas Propag.*, no. 12, pp. 1392–1400, 1985.

[45] P. Gibson, "The Vivaldi Aerial," in *9th European Microwave Conference*. IEEE, Oct. 1979, pp. 101–105.

[46] Y. Aziz, H. E. Hennawy, S. Mahrous, and K. Schunemann, "Design of vivaldi antenna for microwave integrated circuits applications," in *14th European microw. Conf.*, no. 1, 1984, pp. 637–642.

[47] E. Gazit, "Improved design of the Vivaldi antenna," *IEE Proc. Microw., Antennas and Propag.*, vol. 135, no. 2, pp. 89–92, 1988.

[48] J. D. S. Langley, P. Hall, and P. Newham, "Novel ultrawide bandwidth Vivaldi antenna with low crosspolarization," *Electronics Letters*, vol. 29, no. 23, pp. 2004–2005, 1993.

[49] J. Langley, P. Hall, and P. Newham, "Balanced antipodal Vivaldi antenna for wide bandwidth phased arrays," *IEE Proc. Microw., Anten. and Propag.*, vol. 143, no. 2, p. 97, 1996.

[50] I. Linardou, C. Migliaccio, J.M. Laheurte, and A. Papiernik, "Twin Vivaldi antenna fed by coplanar waveguide," *Electronics Letters*, vol. 33, no. 22, pp. 1835–1837, 1997.

[51] I. Linardou, C. Migliaccio, and J. M. Laheurte, "Equivalent circuit of twin Vivaldi antenna fed," *Electronics Letters*, vol. 35, no. 25, pp. 2160–2161, 1999.

[52] A. Butrym and S. Pivnenko, "CPW To CPS Transition," in *Ultrawideband and Ultrashort Impulse Signals*, vol. 2, 2004, pp. 107–108.

[53] E. D. Lera, E. Garcia, E. Rajo, and D. Segovia, "A coplanar Vivaldi antenna with wide band balun proposal for the low frequency band of the SKA: approach to the FPA solution," in *IEEE Melecon*, 2006, pp. 557–560.

[54] A. Vasylchenko, L. Wang, Z. Ma, W. De Raedt, and G. A. E. Vandenbosch, "A very compact CPW-to-CPS balun for UWB antenna feeding," in *25th Convention of Electrical and Electronics Engineers in Israel*, 2008, pp. 446–449.

[55] C. Prest, S. Wang, and J. Zavala, "Antennas for compact portable wireless devices," *US Patent 7,623,077*, 2009.

[56] M. Jamel, P. Bertagna, and R. J. Davis, "Footwear with GPS," *US Patent 6,788,200*, vol. 1, no. 12, 2004.

[57] D. Torrieri, M. B. Bendak, and G. Ritchie, "Indoor geolocation by inertial navigation," *2011 - MILCOM 2011 Military Communications Conference*, pp. 1760–1765, Nov. 2011.

[58] R. Zhang, F. Hoeflinger, O. Gorgis, and L. M. Reindl, "Indoor localization using inertial sensors and ultrasonic rangefinder," *2011 International Conference on Wireless Communications and Signal Processing (WCSP)*, no. 1, pp. 1–5, Nov. 2011.

[59] J. Paradiso, K.-y. Hsiao, and E. Hu, "Interactive Music for Instrumented Dancing Shoes," in *International Computer Music Conference*, no. October, 1999, pp. 13–16.

[60] C. Mariotti, V. Lakafosis, M. M. Tentzeris, and L. Roselli, "An IPv6-enabled Wireless Shoe-Mounted Platform for Health-monitoring," *IEEE Topical Conference on Wireless Sensors and Sensor Networks*, pp. 46–48, 2013.

[61] M. Farooqui and A. Shamim, "Dual band inkjet printed bow-tie slot antenna on leather," *Proc. IEE Conference on Antennas & Propagation*, pp. 3287–3290, 2013.

[62] Z. Abbas, R. D. Pollard, and R. W. Kelsall, "A Rectangular Dielectric Waveguide Technique for Determination of Permittivity of Materials at," *Microwave and Optical Technology Letters*, vol. 46, no. 12, pp. 2011–2015, 2011.

[63] R. Mosig, N. G. Alexopolous, A. Stratton, L. Chow, P. A. Bernard, and J. M. Gautray, "Measurement of Dielectric Constant Using a Microstrip Ring Resonator ," *Trans. on Microw. Theo. and Techniq.*, vol. 39, no. 3, pp. 592–595, 1991.

[64] T. Marsland and S. Evans, "Dielectric measurements with an open-ended coaxial probe," *IEEE proceedings*, vol. 134, no. 4, p. 341, 1987.

[65] D. K. Ghodgaonkar, V. V. Varadan, and V. K. Varadan, "A Free-Space Method for Measurement of Dielectric Constants and Loss Tangents at Microwave Frequencies," *IEEE Trans. Instrum. Meas.*, vol. 37, no. 3, pp. 789–793, 1989.

[66] M. D. Pozar, *Microwave and RF Design of Wireless Systems*. New York: John Wiley and Sons, 2001.

[67] Balanis, C. A., *Antenna Theory*. New Jersey: John Wiley and Sons, 2005.

[68] "IEEE Std 802.15.4a-2007, IEEE Standard for Information Technology-Telecommunications and Information Exchange Between Systems-LANs and MANs-Specific Requirements-Part 15.4: Wireless MAC and PHY Specifications for LR-WPANs."

[69] A. Dumoulin, M. John, M. J. Ammann, and P. McEvoy, "Optimized Monopole and Dipole Antennas for UWB Asset Tag Location Systems," *IEEE Trans. Antennas Propag.*, vol. 60, no. 6, pp. 2896–2904, 2012.

[70] G. Quintero, J. Zürcher, and A. K. Skrivervik, "System Fidelity Factor : A New Method for Comparing UWB Antennas," *Trans. Antennas Propag.*, vol. 59, no. 7, pp. 2502–2512, 2011.

[71] D. Gaetano, A. Dumoulin, M. J. Ammann, and P. McEvoy, "Conformal UWB Impulse Antenna for Pipe Telemetry," in *Loughborough Antennas and Propagation Conference*, no. November, 2011, pp. 3–6.

[72] C. H. Durney, H. Massoudi, and M. F. Iskander, *Radiofrequency Radiation Dosimetry Handbook*. Brooks Air Force Base-USAFSAM-TR-85-73, 1986.

[73] C. Gabriel, "Compilation of the dielectric properties of body tissues at RF and microwave frequencies," Brooks Air Force Base, Texas, Tech. Rep., 1996.

[74] "An internet Resource for the Calculation of the Dielectric Properties of Body Tissues." [Online]. Available: http://niremf.ifac.cnr.it

[75] "Make Human." [Online]. Available: http://www.makehuman.org/

[76] "Blender." [Online]. Available: www.blender.org

[77] M. Clemens and W. T., "Discrete Electromagnetism with the Finite Integration Technique," *Progress In Electromagn. Research*, vol. 32, pp. 65–87, 2001.

[78] "ICNIRP guidelines for limiting exposure to time-varying electric, magnetic and electromagnetic fields (up to 300 GHz)."

[79] "IEEE C95. 1-1992: IEEE Standard for Safety Levels with Respect to Human Exposure to Radio Frequency Electromagnetic Fields, 3 kHz to 300 GHz."

[80] A. Lea, P. Hui, J. Ollikainen, and R. Vaughan, "Propagation Between On-Body Antennas," *IEEE Trans. Antennas Propag.*, vol. 57, no. 11, pp. 3619–3627, Nov. 2009.

[81] M. Grimm and D. Manteuffel, "Norton Surface Waves in the Scope of Body Area Networks," *IEEE Trans. Antennas Propag.*, vol. 62, no. 5, pp. 2616–2623, May 2014.

[82] "IEEE Standard Definitions of Terms for Radio Wave Propagation, IEEE Std. 211-1997."

[83] L. Akhoondzadeh-Asl, Y. Nechayev, P. S. Hall, and C. C. Constantinou, "Parasitic Array Antenna With Enhanced Surface Wave Launch-

ing for On-Body Communications," *IEEE Trans. Antennas Propag.*, vol. 61, no. 3, pp. 1976–1985, 2013.

[84] M. Rehman, Y. Gao, X. Chen, C. Parini, Z. Ying, T. Bolin, and J. W. Zweers, "On-body bluetooth link budget: Effects of surrounding objects and role of surface waves," in *Loughborough Antennas and Propagation Conference*, 2008, pp. 97–100.

[85] L. Akhoondzadeh-asl, P. S. Hall, and Y. Nechayev, "Depolarization in On-Body Communication Channels at 2.45 GHz," *Trans. Antennas Propag.*, vol. 61, no. 2, pp. 882–889, Feb. 2013.

[86] H. B. Lim, D. Baumann, J. Cai, R. Koh, E. P. Li, and Y. Lu, "Antennae Polarization for Effective Transmission of UWB Signal around Human Body," in *International Conference on Ultra-Wideband*. IEEE, Sep. 2007, pp. 220–224.

[87] A. Khaleghi and I. Balasingham, "Non-line-of-sight on-body ultra wideband (1-6 GHz) channel characterisation using different antenna polarisations," *IET Proc. Microw, Anten & Propag*, vol. 3, no. 7, p. 1019, 2009.

[88] X. Artiga, J. Perruisseau-carrier, P. Pardo-carrera, I. Llamas-garro, and Z. Brito-brito, "Halved Vivaldi Antenna With Reconfigurable Band Rejection," *IEEE Antennas Wireless Propag. Lett.*, vol. 10, pp. 56–58, 2011.

[89] D. H. Gadani, R. V. A., S. P. Bhatnagar, P. A. N., and V. A.D., "Effect of Salinity on the Dielectric Properties of Water," *Indian Journal of Applied and Pure Physics*, vol. 50, pp. 405–410, 2012.

[90] L. Klein and C. Swift, "An improved model for the dielectric constant of sea water at microwave frequencies," *IEEE Trans. Antennas Propag.*, vol. 25, no. 1, pp. 104–111, Jan. 1977.

[91] S. Arcone, A. Gow, and S. McGrew, "Microwave Dielectric, Structural, and Salinity Properties of Simulated Sea Ice," *IEEE Trans. on Geoscience and Remote Sensing*, vol. GE-24, no. 6, pp. 832–839, Nov. 1986.

[92] J. Wang, O. Fujiwara, and S. Watanabe, "Approximation of Aging Effect on Dielectric Tissue Properties for SAR Assessment of Mobile Telephones," *IEEE Trans. on Electrom. Compatib.*, vol. 48, no. 2, pp. 408–413, May 2006.

[93] W. G. Scanlon and N. E. Evans, "Body-surface Mounted Antenna Modelling for Biotelemetry Using FDTD with Homogeneous, Two- and Three- Layer Phantoms," *10th Internationaf Conference on Antennas and Propagation*, vol. 436, no. 0, Apr. 1997.

[94] V. Hebelka, J. Lacik, K. Pitra, and Z. Raida, "Slot antennas for on-body communication," *Applied Electromagnetics and Communications (ICECom)*, pp. 1–6, Oct. 2013.

[95] N. Haga, K. Saito, M. Takahashi, and K. Ito, "Characteristics of Cavity Slot Antenna for Body-Area Networks," *IEEE Trans. Antennas Propag.*, vol. 57, no. 4, pp. 837–843, Apr. 2009.

[96] "Tekscan Systems." [Online]. Available: http://www.tekscan.com/medical/system-fscan1.html

[97] S. J. M. Bamberg, A. Y. Benbasat, D. M. Scarborough, D. E. Krebs, and J. a. Paradiso, "Gait analysis using a shoe-integrated wireless sensor system." *IEEE Trans. on Inf. Technol. in Biomed.*, vol. 12, no. 4, pp. 413–23, Jul. 2008.

[98] S. J. Morris, J. A. Paradiso, and A. H. Development, "Shoe-Integrated Sensor System For Wireless Gait Analysis And Real-Time Feedback,"

in *Proceedings of the Second Joint EMBS BMES Conference*, 2002, pp. 2468–2469.

[99] "802.15.1-2002-IEEE Standard for Telecommunications and Information Exchange Between Systems-LAN/MAN-Specific Requirements-Part 15: Wireless Medium Access Control (MAC) and Physical Layer (PHY) Specifications for Wireless Personal Area Networks (WPANs)."

[100] "802.11a-1999-IEEE Standard for Information Technology-Telecommunications and Information Exchange Between Systems-Local and Metropolitan Area Networks-Specific Requirements-Part 11: Wireless LAN Medium Access Control (MAC) and Physical Layer (PHY) Spec."

[101] Zigbee Alliance, "Zigbee Specification," Tech. Rep., 2008.

[102] "CST Microwave Studio." [Online]. Available: www.cst.com

[103] S. Kim, C. Brendle, H.-Y. Lee, M. Walter, S. Gloeggler, S. Krueger, and S. Leonhardt, "Evaluation of a 433 MHz band body sensor network for biomedical applications." *Sensors*, vol. 13, no. 1, pp. 898–917, Jan. 2013.

[104] A. Sabban, "New Wideband Printed Antennas for Medical Applications," *IEEE Trans. Antennas Propag.*, vol. 61, no. 1, pp. 84–91, 2013.

[105] X. Huo, U.-M. Jow, and M. Ghovanloo, "Radiation characterization of an intra-oral wireless device at multiple ISM bands: 433 MHZ, 915 MHZ, and 2.42 GHz." *IEEE Proc. : Annual International Conference of the IEEE Engineering in Medicine and Biology Society*, vol. 2010, pp. 1425–8, Jan. 2010.

[106] M. Weiss, J. Smith, and J. Bach, "RF coupling in a 433-MHz biotelemetry system for an artificial hip," *IEEE Antennas Wireless Propag. Lett.*, vol. 8, pp. 916–919, 2009.

[107] D. Gaetano, P. McEvoy, M. J. Ammann, C. Brannigan, L. Keating, and F. Horgan, "On-body Fidelity Factor for Footwear Antennas Over Different Ground Materials," in *Proc. IEE Conference on Antennas & Propagation*, 2014.

[108] M. Kim and J.-I. Takada, "Characterization of Wireless On-Body Channel Under Specific Action Scenarios at Sub-GHz Bands," *IEEE Trans. Antennas Propag.*, vol. 60, no. 11, pp. 5364âĂŞ–5372, 2012.

[109] R. Dalke, C. Holloway, P. McKenna, J. M., and A. Ali, "Effects of reinforced concrete structures on RF communications," *IEEE Trans. Electromagn. Compat.*, vol. 42, no. 4, pp. 486–496, 2000.

[110] T. S. P. See and Z. N. Chen, "Experimental Characterization of UWB Antennas for On-Body Communications," *IEEE Trans. Antennas Propag.*, vol. 57, no. 4, pp. 866–874, Apr. 2009.

[111] K. Ito, "Human body phantoms for evaluation of wearable and implantable antennas," in *2nd Eur. Conf. Antennas and Propagation*, 2007.

[112] M. John and M. J. Ammann, "Antenna Optimization With a Computationally Efficient Multiobjective Evolutionary Algorithm ," *IEEE Trans. Antennas Propag.*, vol. 57, no. 1, pp. 260–263, 2009.

[113] J. Liang, C. C. Chiau, X. Chen, and C. G. Parini, "Study of a Printed Circular Disc Monopole Antenna for UWB Systems," *IEEE Trans. Antennas Propag.*, vol. 53, no. 11, pp. 3500–3504, 2005.

[114] K. Fujii, K. Ito, and S. Tajima, " A study on the receiving signal level in relation with the location of electrodes for wearable devices using

human body as a transmission channel ," *Proc. IEEE Antennas and Propagation Society International Symposium*, pp. 1071–1074, 2003.

[115] Chambers, H. G. , and D. H. Sutherland, "A practical guide to gait analysis," *J. Amer. Acad. Orthop. Surg.*, vol. 10, pp. 222–231, 2002.

[116] K. S. Kwak, S. Ullah, and N. Ullah, "An overview of IEEE 802.15.6 standard," *2010 3rd International Symposium on Applied Sciences in Biomedical and Communication Technologies (ISABEL 2010)*, pp. 1–6, Nov. 2010.

Appendix A.

List of Publications

Journal Publications

[JP 1] D. Gaetano, V. Sipal, P. McEvoy, M. J. Ammann, C. Brannigan, L. Keating, and F. Horgan "Footwear-centric body area network with directional UWB antenna," *Electronics Letters*, vol. 49, no. 14, pp. 860–861, July 2013.

[JP 2] D. Gaetano, P. McEvoy, M. J. Ammann, J. E. Browne, L. Keating, and F. Horgan, "Footwear Antennas for Body Area Telemetry," *IEEE Transactions on Antennas and Propagation*, vol. 61, no. 10, pp. 4908–4916, Oct. 2013.

[JP 3] D. Gaetano, P. McEvoy, M. J. Ammann, C. Brannigan, L. Keating, and F. Horgan, "Footwear and Wrist Communication Links using 2.4 GHz and UWB Antennas," *Electronics*, vol. 3, no. 2, pp. 339–350, June 2014.

[JP 4] D. Gaetano, M. J. Ammann, P. McEvoy, M. John, L. Keating, and F. Horgan, "Proximity Study of a UWB Directional Conformal Antenna on Water Pipe," *Microwave and Optical Technology Letters*, vol. 54, no. 8, pp. 1982–1986, Aug. 2012.

[JP 5] G. Ruvio, D. Gaetano, M. J. Ammann, and P. McEvoy, "Antipodal Vivaldi Antenna for Water Pipe Sensor and Telemetry," *International Journal of Geophysics*, vol. 2012, Article ID 916176, May 2012.

International Conference Publications

[CP 1] D. Gaetano, A. Dumoulin, P. McEvoy, and M. J. Ammann, "Conformal UWB Impulse Antenna for Pipe Telemetry," in *Proc. LAPC - Loughborough Antennas & Propagation Conference*, Loughborough, UK, Nov. 14–15, 2011.

[CP 2] D. Gaetano, M. J. Ammann, P. McEvoy, M. John, L. Keating, and F. Horgan, "A Conformal UWB Directional Antenna," in *Proc. EuCAP - European Conference on Antennas and Propagation*, Rome, Italy, Mar. 11–15, 2011.

[CP 3] M. J. Ammann, P. McEvoy, D. Gaetano, L. Keating, and F. Horgan, "(Invited) An Antenna for Footwear," in *Proc. MobiHealth 3rd International Conference on Wireless Mobile Communication and Healthcare*, Paris, France, Mar. 21–22, 2012.

[CP 4] D. Gaetano, P. McEvoy, M. J. Ammann, C. Brannigan, L. Keating, and F. Horgan, "On-body Fidelity Factor for Footwear Antennas Over Different Ground Materials," in *Proc. EuCAP - European Conference on Antennas and Propagation*, The Hague, The Netherlands, Mar. 06–11, 2014.

[CP 5] V. Sipal, D. Gaetano, P. McEvoy, M. J. Ammann, C. Brannigan, L. Keating, and F. Horgan, "Fading and Rician K-factor in the Ultra Wideband Footwear-Centric Body Area Network," in *Proc. EuCAP - European Conference on Antennas and Propagation*, The Hague, The Netherlands, Mar. 06–11, 2014.

[CP 6] D. Gaetano, P. McEvoy, M. J. Ammann, C. Brannigan, L. Keating, and F. Horgan, "Anatomical Loading on a UWB Antenna for Shoe Toe Box" in *Proc. APS - IEEE International Symposium on Antennas and Propagation*, Orlando, USA, July 8–13, 2013.

[CP 7] G. Ruvio, R. Solimene, A. Cuccaro, J. E. Browne, D. Gaetano, and M. J. Ammann, "Experimental Microwave Breast Cancer Detection with Oil-in-

Gelatin Phantom" in *Proc. ICEAA - IEEE International Conference Electromagnetics in Advanced Applications*, Torino, Italy, Sept. 9–13, 2013.